Academy of Montpellier

MONTPELLIER 2 UNIVERSITY
— SCIENCES AND TECHNIQUES OF LANGUEDOC —

THESIS

in partial fulfillment of the requirements for the degree of
DOCTOR OF ELECTRONICS AT MONTPELLIER 2 UNIVERSITY
DOCTORAL COURSE: Electronics, Nanotechnologies, Components and Systems
DOCTORAL SCHOOL: Electrical Engineering

Theoretical and experimental investigation of a new GaN based solid state terahertz MASER

Publicly introduced by:

Thibault LAURENT

under the direction of Luca VARANI and Jérémie TORRES

defended on December 3, 2010 in front of the following examination panel:

Christophe GAQUIERE	Professor, Lille University	Referee
Javier MATEOS	Associate Professor, Salamanca University	Referee
Yvon CORDIER	Senior Researcher, Research Center on Hetero-Epitaxy and its Applications, Valbonne	Examiner
Wojciech KNAP	Research Leader, Montpellier 2 University	Examiner
Jerzy ŁUSAKOWSKI	Professor, Warsaw University	Examiner
Patrick MOUNAIX	Research Scientist, Bordeaux University	Examiner
Jérémie TORRES	Associate Professor, Montpellier 2 University	Supervisor
Luca VARANI	Professor, Montpellier 2 University	Supervisor

Institut d'Électronique du Sud — UMR UM2-CNRS 5214

Contents

Symbols table vii

Acronyms table xi

General introduction 1

I State of the art and theory 5

1 The terahertz: waves of tomorrow 7
- 1.1 The terahertz frequency domain . . . 8
- 1.2 Applications of THz radiations . . . 8
  - 1.2.1 Medical applications . . . 8
  - 1.2.2 Industrial applications . . . 9
  - 1.2.3 Other applications . . . 11
- 1.3 State of the art . . . 11
  - 1.3.1 Direct generation of THz radiations . . . 11
  - 1.3.2 Indirect generation of THz radiations . . . 15
  - 1.3.3 Detectors . . . 15
- 1.4 Summary . . . 17

2 The optical phonon transit time resonance in gallium nitride 19
- 2.1 Electronic transport and the Boltzmann equation . . . 20
  - 2.1.1 The Boltzmann equation . . . 20
  - 2.1.2 The Fermi's golden rule . . . 23
- 2.2 Carrier scatterings in semiconductors . . . 26
  - 2.2.1 Relaxation times . . . 26
  - 2.2.2 Scattering with ionized impurities . . . 29
  - 2.2.3 Scattering with acoustic phonons . . . 32
  - 2.2.4 Scattering with polar optical phonons . . . 32
  - 2.2.5 Other interactions . . . 33
- 2.3 The optical phonon transit time resonance . . . 34
  - 2.3.1 Origin of optical phonon transit time resonance . . . 34
  - 2.3.2 Description of optical phonon transit time resonance . . . 35
  - 2.3.3 Conditions for optical phonon transit time resonance . . . 36
  - 2.3.4 Amplification by optical phonon transit time resonance . . . 37
- 2.4 Scattering rates and amplification bands in gallium nitride . . . 40

2.4.1 Bulk material . . . 40
2.4.2 2-D material . . . 43
2.4.3 Comparison of GaN with other materials . . . 45
2.5 Device design and experimental conditions . . . 46
2.5.1 Electric field versus device length . . . 46
2.5.2 Operating temperature . . . 48
2.6 Summary . . . 48

II Experimental realization 49

3 GaN quantum-wells: towards concrete devices 51
3.1 Pre-process conception . . . 52
3.1.1 Different layers . . . 52
3.1.2 Band diagram . . . 53
3.1.3 Fabrication of masks . . . 54
3.2 Fabrication process . . . 56
3.2.1 Substrates . . . 56
3.2.2 Process . . . 56
3.3 Post-process characterizations . . . 58
3.3.1 SEM - AFM imaging . . . 58
3.3.2 Electrical characterization . . . 60
3.4 Summary . . . 61

4 Experimental setup 63
4.1 Aim of the measurements . . . 64
4.1.1 Goal to achieve . . . 64
4.1.2 Experimental conditions . . . 64
4.1.3 Frequency range of operation . . . 65
4.2 Setup design . . . 65
4.2.1 Instruments . . . 65
4.2.2 Description . . . 74
4.2.3 Optical alignment . . . 76
4.3 Characterizations of the bench . . . 79
4.3.1 Frequency properties . . . 79
4.3.2 Power properties . . . 80
4.3.3 Gain measurement . . . 80
4.4 Measurement procedure . . . 82
4.4.1 Experiment control . . . 83
4.4.2 Calibration . . . 85
4.5 Current-voltage measurements . . . 87
4.5.1 Continuous measurements . . . 87
4.5.2 Pulsed measurements . . . 88
4.6 Summary . . . 89

III Results **91**

5 Electrical characterization of the samples **93**
5.1 Description of the different structures . . . 94
5.2 Temperature dependence . . . 94
5.2.1 Transmission lines model . . . 94
5.2.2 High electron mobility transistors . . . 95
5.2.3 Interdigitated fingers . . . 96
5.2.4 Discussion . . . 96
5.3 Geometry dependence . . . 97
5.3.1 Transmission lines model . . . 97
5.3.2 High electron mobility transistors . . . 97
5.3.3 Interdigitated fingers . . . 98
5.3.4 Optimization of the devices proposal . . . 100
5.4 Pulse duration dependence . . . 100
5.5 OPTTR investigation . . . 101
5.6 Summary . . . 104

6 Experimental investigation of terahertz transmission **105**
6.1 Room temperature passive measurements with the photomixing bench . . . 106
6.1.1 About the experiment and data processing . . . 106
6.1.2 GaN over sapphire sample . . . 107
6.1.3 Investigation of other samples . . . 108
6.2 Room and low-temperature measurements with the electronic source . . . 110
6.2.1 About the data processing . . . 110
6.2.2 Polarization dependence . . . 111
6.2.3 Temperature dependence . . . 113
6.2.4 Geometry dependence . . . 113
6.2.5 Electric field dependence . . . 114
6.3 Summary . . . 116

General summary **121**

IV Appendices **125**

A Electrical characterizations of grown samples **127**
A.1 Capacitance-voltage measurements . . . 127
A.2 Van der Pauw and Hall effect measurements . . . 128
A.2.1 Van der Pauw . . . 128
A.2.2 Hall effect . . . 130
A.3 Buffer layers resistivity . . . 131
A.4 Contact and sheet resistances measurements . . . 131

B Description of the *Tera-Spectro* program **133**
B.1 Introduction . . . 133
B.2 Regulation of the lasers . . . 133

List of figures **135**

List of tables **137**

Bibliography **141**

Publications of the author **149**

Symbols table

Greek letters are repported at the end of the table

Symbol	Magnitude	Value	Unit
$\mathbf{a}$	Acceleration vector		m/s^2
$\bar{A}(\mathbf{r},t)$	Averaging of the quantity $A(\mathbf{r},\mathbf{v},t)$ with the help of the distribution function		
A_β	Deformation amplitude in the case of the deformation-potential interaction		m
c	Velocity of light in vacuum	2.998×10^8	m/s
$c_k(t)$	Projection coefficients of the wave function of a perturbed problem on the orthonormal set made of wave functions of the unperturbed problem		
c_l	Elastic constant		Pa
d	Hole of the sample holder diameter		m
D_A	Deformation acoustic potential		J
E	Electron energy		J
$E_{C0}(\mathbf{r})$	Applied or built-in potential energy		J
E_f	Fermi level of the energy band		J
E_g	Band-gap energy		J
$E_i, i \in \mathbb{N}^*$	i^{th} energy level of a quantum-well		
$f(\mathbf{r},\mathbf{v},t)$	Distribution function		
$G_{d_e}(\nu)$	Gain calculated by the formula of equation (4.10)		
$G_{raw}(\nu)$, $G(\nu)$	Gain calculated by the raw formula: $G_{raw}(\nu) = \frac{P_b(\nu)}{P_c(\nu)}$		
h	Planck constant	6.626×10^{-34}	$m^2.kg/s$
$\hbar$	Reduced Planck constant that is $h/(2\pi)$	1.056×10^{-34}	$m^2.kg/s$
H_0	Hamiltonian operator for the unperturbed problem that is: $E_{C0} + U_C$		J
$H_{k'_0 k_0}$, $H_{\mathbf{p}'\mathbf{p}}$	Matrix element of the scattering potential between states k'_0 and k_0, or $\mathbf{p}$ and $\mathbf{p}'$		J
i	Complex number that is $i^2 = -1$		
$I(k,k')$	Overlap factor		
I_d	Current crossing a device under study		A
$\mathbf{k}$	Wave vector		cm^{-1}

Symbol	Magnitude	Value	Unit
k_B	Boltzman constant	1.381×10^{-23}	$m^2.kg.s^{-2}.K^{-1}$
K	Relative area of the sample under study with respect to the area of the sample holder hole		
L, L_{dev}	Semiconductor length		m
L_A	Length of the long (active) zones in a IDF structure		m
L_{ds}	Drain-source length in a HEMT		m
L_D	Debye length		m
L_g	Gate length in a HEMT		m
L_P	Length of the short (passive) zones in a IDF structure		m
L_T	Sum of active and passive lengths of a IDF structure: $L_T = L_A + L_P$		m
L_{TLM}	Length between contacts in a TLM structure		m
m^*	Effective electron mass		kg
m_0	Electron mass	9.109×10^{-31}	kg
$n(\mathbf{r}, t)$	Particle density		m^{-3}
$N(\mathbf{r}, \mathbf{v}, t)$	Number of particles in the crystal		
N_D	Impurities concentration		m^{-3}
N_β	Bose-Einstein factor that is: $N_\beta = \frac{1}{e^{\frac{\hbar\omega_0}{k_B T}} - 1}$		
$\mathbf{p}$	Electron momentum vector		kg.m/s
p	Electron momentum		kg.m/s
p_t	Component of the piezoelectric tensor		
$P(k = k_0)$	Probability of finding a particle with the wave vector k_0		
$P(\nu)$, $P_{b_0}(\nu)$	Transmission spectrum of the unbiased sample		V
$P_b(\nu)$	Transmission spectrum of the biased sample		V
$P_c(\nu)$	Calibration spectrum of the bench without sample		V
$P_d(\nu)$	Transmission spectrum of the biased device		V
$P_{d_0}(\nu)$	Transmission spectrum of the unbiased device		V
q	Electronic charge	-1.602×10^{-19}	C
$\mathbf{r}$	Space position vector of the considered particle		m
r	Radius parameter in spherical coordinates		m
R	A resistance		Ω
R_A, R_P, R_T	Equivalent resistances of the active, passive and total zones of an IDF		Ω
R_S	Sheet resistance of a 2D channel		$\Omega/\square$
$\Re[x]$	Real part of a complex variable x		$[x]$
$S(k_0, k_0')$	Scattering rate from k_0 to k_0'		s^{-1}
t	Time		s

Symbol	Magnitude	Value	Unit
T	Absolute temperature		K
T_L	Lattice temperature		K
$\mathbf{u}$	Unity vector directed along the device		
$U_C(\mathbf{r})$	Crystal electrostatic potential due to atoms		J
$U_S(\mathbf{r}, t)$	Scattering potential		J
U_0	A voltage		V
$\mathbf{v}$	Velocity vector of the considered particle		m/s
v	Velocity		m/s
V	Electrostatic potential		V
v_s	Sound velocity		m/s
V_{ds}	Voltage applied on a device		V
W, W_{dev}, W_{QW}	Width of a quantum-well		m
x	Asymmetry factor of the IDF structures that is: $x = \frac{L_A}{L_T}$		
z	One dimension problem space position		m
α	Angle between momentums $\mathbf{p}$ and $\mathbf{p}'$		rad
$\alpha_0(\nu, n)$	Gain of the devices		
$\alpha(\nu)$	Transmission coefficient defined by: $\alpha(\nu) = \frac{P_b(\nu)}{P_{b_0}(\nu)}$		
$\hbar\boldsymbol{\beta}$	Momentum change vector resulting from a scattering event		kg.m/s
β	Wavevector		m^{-1}
$\delta(x)$	Dirac function of x that is: $\delta(x) = \begin{cases} 1, x = 0 \\ 0, x \neq 0 \end{cases}$		
∇^2	Laplacian operator		
ε_r, ε_{r_0}	Low frequency dielectric constant		
ε_{r_∞}	High frequency dielectric constant		
ε_0	Vacuum permittivity	8.854×10^{-12}	F/m
θ	Angle of the momentum with the $\mathbf{z}$ direction, i.e. the inclination angle in spherical coordinates		rad
λ	A wavelength		m^{-1}
μ	Mobility		cm^2/V.s
ν	Frequency		Hz
ν_-, ν_+	Relaxation rates in the passive and active regions, respectively		Hz
ν_Σ	Transit frequency for an electron started from the passive area center to reach its boundary		Hz
π	Archimede's Constant	3.141	
ρ	Mass density		$\mathrm{kg/m}^3$
$\boldsymbol{\Sigma}$, $\boldsymbol{\Sigma}_0$, $\boldsymbol{\Sigma}_0'$	Electric field vector		V/m
$\tau(\mathbf{p}_0)$	Scattering time		s
$\tau_E(\mathbf{p}_0)$	Energy relaxation time		s

Symbol	Magnitude	Value	Unit
$\tau_m(\mathbf{p}_0)$	Momentum relaxation time		s
τ_-, τ_+	Relaxation times in the passive and active regions, respectively		s
τ_Σ	Transit time necessary for an electron started from the passive area center to reach its boundary		s
γ_R	Absorption coefficient		m^{-1}
ϕ	Azimuth angle in spherical coordinates		rad
$\Psi(\mathbf{r}, t)$	Wave function		
$\psi(\mathbf{r})$	Space dependence part of the wave function $\Psi(\mathbf{r}, t)$		
ω	Angular frequency		rad/s
Ω	Semiconductor volume		m^3
ω_0	Polar optical phonon angular frequency		rad/s

Acronyms table

Acronym	Meaning
AFM	Atomic Force Microscopy
AITHER	Amplificating Integrable TeraHertz Emitter of Radiation
ANR	French National Research Agency
ASCII	American Standard Code for Information Interchange (plain text file)
BEP	Beam Equivalent Pressure
CAR	Continual Azimuthal Rotation
CMOS	Complementary Metal-Oxide-Semiconductor
CR	Cyclotron Resonance
CRHEA	Research Center on Hetero-Epitaxy and its Applications of Valbonne, France
DFB	Distributed FeedBack
DNA	DeoxyriboNucleic Acid
DNDM	Dynamic Negative Differential Mobility
FIRAS	Far Infrared Absolute Spectrometer
FWHM	Full Width at Half Maximum
HBT	Heterojunction Bipolar Transistor
HDPE	High-Density PolyEthylene
HEMT	High Electron Mobility Transistor
HF	High-Frequency
HVPE	Hydride Vapor Phase Epitaxy
IDF	InterDigitated Fingers
IES	Institute of Electronics of the South of Montpellier, France
IMPATT	IMPact ionization Avalanche Transit-Time
JFET	Junction Field Effect Transistor
LO	Local Oscillator
LTG	Low Temperature Grown
MBE	Molecular Beam Epitaxy
MESFET	MEtal Semiconductor Field Effect Transistor
MOVPE	MetallOrganic Vapor Phase Epitaxy
NEMAG	Negative Effective Mass Amplifier and Generator
OPTTR	Optical Phonon Transit Time Resonance
OSA	Optical Spectrum Analyzer
PE	PolyEthylene
PID	Proportional, Integral, and Derivative corrector
PTFE	PolyTetraFluoroEthylene

Acronym	Meaning
PM	Polarization Maintaining
QCL	Quantum Cascade Laser
RF	Radio-Frequency
RFID	Radio-Frequency IDentification
RHEED	Reflection High-Energy Electron Diffraction
SEM	Scanning Electron Microscopy
SOA	Semiconductor Optical Amplifier
SPI	Semiconductor Physics Institute of Vilnius, Lithuania
TLM	Transmission Line Method (or Model)

General introduction

The terahertz (THz) frequency range (1 THz $= 10^{12}$ Hz) lies from 300 GHz to 30 THz, which corresponds to wavelengths between 1 mm and 10 µm. Previously known as the *Far Infrared Range*, it represents an exceptionally underused domain of the electromagnetic spectrum. Nevertheless, THz radiations have a great number of potential applications in several domains: high-resolution spectroscopy in physics (THz time domain spectroscopy, study of electron dynamics, interaction with phonons, impurities, etc.), in chemistry (gas detection, pollution and environment control, study of chemical reactions, etc...), in astronomy (study of galaxies, detection of gas, atoms and ionized molecules, ...), in telecommunications (wireless and broadband networks, short range networks, radars), in industrial imaging (inspection of materials, devices and systems), in medicine (detection of caries, oncology, diagnostic of burns), in biology (water detection, food industry), in security domain (detection of weapons and dangerous materials). Therefore the realization of devices able to operate at these frequencies represents one of the greatest challenges of both modern electronics and optoelectronics since this domain is well above the typical frequencies of microwave electronics and, at the same time, well below the typical frequencies of optical and infrared generators. At present, there is a huge international effort to develop low-cost, reliable, compact and tunable sources, able to operate continuously at ambient (or near- ambient) temperature and compatible with the standard technological dies to achieve easy integration in complex systems and circuits. This is confirmed by the exceptional increase in the number of articles published in international journals and in proceedings of international conferences devoted to theoretical and experimental investigations of the THz frequency domain and related devices.

As concerns the so-called THz optical sources, two strategies are exploited: the indirect and the direct generations. In the former case, the principle consists in using light sources which are available within the visible or the infrared domain and to obtain lower frequencies, for instance, through optical beatings between two laser sources, or by flashing a non-linear optical crystal or a photoconductor by a femtosecond laser pulse. In the latter case, the principle is to obtain directly the THz emission by optical devices such as the free-electron laser, the p-Germanium laser and, more recently, the quantum cascade laser. However, the main drawbacks associated with these optical THz sources are the relative complexity of the devices, the need to operate at low-temperatures, the high cost and, in some cases, the need of strong magnetic fields.

Both indirect and direct generations can be also employed to realize THz sources using the electronic way. In the former case, the usual technique consists in exploiting different intrinsic non- linearities of electronic devices starting from available oscillators in the GHz range to reach, through frequency multiplication, the THz range. In the latter case, the strategy consists in studying novel materials, physical mechanisms, devices and systems leading to electrical oscillations at higher and higher frequencies. The most used devices are n-i-n diodes, Schottky diodes, heterostructure barrier varactors, IMPATT diodes, resonant tunnel diodes, MESFETs and HEMTs. The main drawbacks of THz generation by the electronic

way are associated with high current levels which often lead to an unacceptable heating of the device, the effect of the contact resistance which tends to suppress the high frequency oscillations, and the obtained efficiencies which are quite low in comparison with a high level of intrinsic noise. The chapter 1 of this manuscript presents the state of the art in term of applications and devices.

My thesis has been developed in the framework of an ANR project (AITHER: Amplificating Integrable TeraHertz Emitter of Radiation). This project is based on the contributions of four complementary research groups: the Institute of Electronics of the South [1] (IES) in Montpellier, the Research Center on Hetero-Epitaxy and its Applications [2] (CRHEA) in Valbonne, Lumilog [3] in Vallauris, and the Semiconductor Physics Institute [4] (SPI) in Vilnius, Lithuania (this last one not included directly in the ANR project). The basic idea was initially proposed by the IES and the SPI some years ago using bulk nitrides as active region. The role of the IES and the SPI is to perform the theoretical modeling, the optimization of the active region and of the resonant cavity using microscopic simulation approaches. Moreover the experimental facilities to measure detection and emission of THz radiation from the fabricated devices has been designed and fabricated in the framework of this thesis within the IES laboratory.

The CRHEA is the main academic laboratory in France devoted to the epitaxial growth of wide band gap semiconductors such as the group III-Nitrides. Its role in the project is the fabrication of the heterostructure device. To achieve working operation it is necessary to control material growth parameters, to reduce the number of dislocations, to study GaN growth on various substrates in order to optimize the quality of the layers in terms of defects, mechanical strain, the buffer insulating character and carrier confinement.

Finally, Lumilog is one of the world leading GaN supplier offering the highest quality bulk GaN and GaN templates on sapphire. It should be emphasized that one of the necessary conditions for reaching the THz amplification is a quasi-ballistic acceleration of electrons in the low- energy region, therefore to decrease the number of electron collisions very-high quality materials are required. To this purpose Lumilog is specialized in templates perfectly lattice matched to GaN-based devices which are mostly targeted for substrate applications for AlGaN/GaN devices. These high quality substrates will be necessary to fabricate efficient and reliable devices.

In this context the following manuscript proposes an original strategy which combines the electronic and the optic approaches: a maser-like device where, similarly to a THz laser, generation is obtained inside a semiconductor when the medium is active and can amplify propagating electromagnetic waves. However, the maser amplification, similarly to a microwave device, is caused by a dynamic negative differential conductivity appearing in a narrow region of the high-frequency spectrum.

In detail we propose to study, develop, fabricate and characterize a novel device able to amplify and generate electromagnetic radiation at THz frequencies.

The active (i.e. amplificating) part of the structure is a 2D electron gas inside a triangular quantum well to which a constant electric field is applied in the lateral direction. The physical mechanism at the basis of the amplification is a quasi-ballistic acceleration of electrons followed by a fast emission of polar optical phonons, the so-called optical phonon transit time resonance (OPTTR). The conditions necessary to achieve the resonance are the absence of interactions at low energies and a very sharp energy threshold for the emission of optical phonons: these two conditions can be satisfied exploiting the special transport properties of nitrides which are much more adapted than standard III-V materials. The cyclic movement of electrons in the phase space enables the amplification of electromagnetic waves

1. http://www.ies.univ-montp2.fr/
2. http://www.crhea.cnrs.fr/
3. Lumilog is a French company providing high quality substrates for device fabrication: http://www.lumilog.com/
4. http://www.pfi.lt/

in a restricted frequency range given by the inverse of the electron transit time in the low-energy region (below the optical phonon energy). The emission of radiation is perpendicular to the well through the device surface and we have already shown that for electric fields of reasonable strength (some kV/cm), this frequency lies in the THz range. The description of this physical mechanism is explained in chapter 2.

Prior to the work developed in this thesis, the project were devoted to the modeling, design and fabrication of a structure which must satisfy all the requirements to reach the optimum conditions for amplification. First of all, semi-insulating substrates of the highest available quality are necessary to reduce the defect density. To this purpose, different templates (GaN-on-Sapphire, and GaN free standing) have to be tested. Successively, appropriate AlGaN/GaN heterostructures grown by molecular beam epitaxy are fabricated to obtain a quantum well which satisfies the conditions established by the theoretical modeling concerning the carrier concentration, mobility, width and position of the well, etc. To obtain THz amplification a device of large area is necessary (typically 1 mm^2) for which an original topology of interdigitated contacts is proposed. In the framework of this thesis, the sapphire substrate have been used: chapter 3 describes how the devices are fabricated on this basis.

The main objective of this thesis involves the design, the fabrication and the full testing of the fabricated devices including structural and electrical characterizations. To ensure that the structure is able to amplify electromagnetic waves, special attention will be paid to the intrinsic gain of the 2D gas: this essential quantity will be evaluated through transmission measurements, with or without applied voltage, performed using a tunable photomixed or electronic sources and a silicon bolometer for detection. For that purpose, several dedicated setups are designed and made: chapter 4 describes them. At this step an important feedback for the fabrication process is to draw optimization rules for the next generation of sample as well as for the final design. The results obtained with the dedicated benches are presented in chapters 5 and 6, and presents the main ideas to optimize the next generation of devices.

If amplification is demonstrated with these devices, the generation of THz radiation will be achieved by placing the active device inside a resonant cavity which will be designed and realized: basically it could be a confocal optical resonator with spherical mirrors whose exact design will depend on the optical characteristics of the interdigitated electrodes.

When all of this will be done, the complete device (active region + resonant cavity = AITHER) will be fully characterized in terms of power emission, quantum efficiency, polarization and line-width using a dedicated Fourier Transform Infrared Reflectometry facility coupled to a bolometer detector.

To conclude, the main theoretical advantages of AITHER with respect to already existing devices should be the following:

1. A wide range of working temperatures which includes also the liquid nitrogen temperature;
2. High values of the maximum amplification coefficient;
3. Wide tuning of the generation frequency, which covers most of the THz range and is obtained by sweeping the applied voltage only;
4. Absence of a magnetic field, which simplifies considerably the device design;
5. Narrow amplification band, which is useful for realizing the single-mode generation;
6. Simple design favourable to integration in circuits.

The AITHER project is funded by the French National Research Agency[5] *(ANR) under the contract AITHER n° ANR-07-BLAN-0321.*

5. http://www.agence-nationale-recherche.fr/

Part I

State of the art and theory

Chapter 1

The terahertz: waves of tomorrow

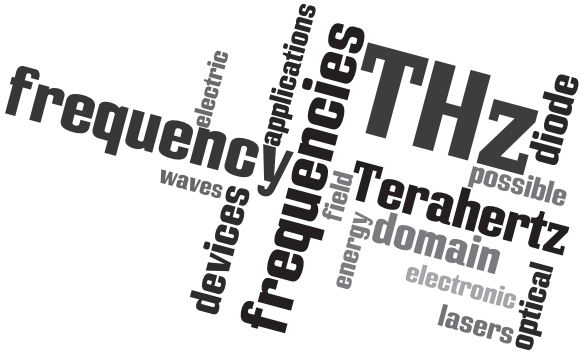

1.1 The terahertz frequency domain

Etymologically speaking, the word "terahertz" comes from the Greek prefix "tera" (*teras, teratos*), which means monster. Prefixing a number, it multiplies by a billion, that is 10^{12}. Consequently, the terahertz (THz) frequencies are one thousand times higher than the classical *gigahertz* frequencies fulfilled by the microwave electronic devices.

In the electromagnetic spectrum, the THz region lies between the microwaves and the mid-infrared optics domain, as shown in figure 1.1: the ranges of wavelengths (and frequencies) corresponds to 10 µm up to 1 mm (300 GHz up to 30 THz). This region is also called far-infrared or sub-millimeter because the wavelengths are greater than the mid-infrared region and smaller than those of the microwaves.

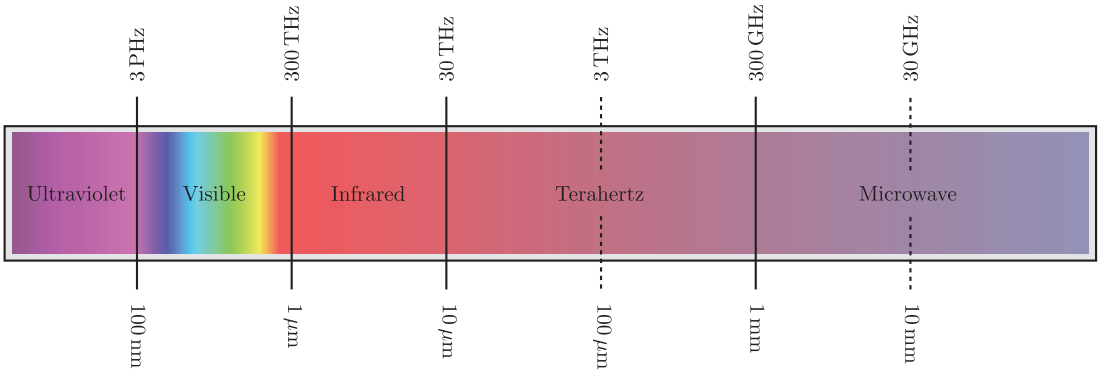

Figure 1.1: Terahertz domain in the electromagnetic spectrum. Upper and lower scales correspond to frequencies and wavelengths respectively.

This domain has been a research enigma for a long time as electronic and optic approaches were not able to reach it.

1.2 Applications of THz radiations

When the first THz generation experiments were carried out, one of the main goals was to find original applications for this new spectral domain. Many investigations had shown some interesting characteristics usable for further applications such as medicine, security, and spectroscopy. The conclusion of this research is a wide range of applications uncovered by other electromagnetic spectral domains (microwaves, infrared, etc.) or where other domains could be dangerous (such as the X-rays). The following sub-sections describe briefly the potential applications of the THz frequency domain.

1.2.1 Medical applications

In the medical domain, it is well known that the use of X-rays is unhealthy due to ionization and penetration properties. Some burn marks or even cancer can result from prolonged exposure of these radiations. Consequently, the use of THz radiations, whose energetic value is much lower (≈ 4 meV) than that of X-rays (> 120 eV), is a good alternative [Siegel 02, Siegel 04]. High-resolution images of the human body, thanks to the transmission and absorption properties of the THz waves, are now possible in a presumed healthy way for the patient. Figure 1.2 is an example of a THz radiography of a tooth which shows that the THz beam can cross the external layer of the tooth to reveal an inside cavity.

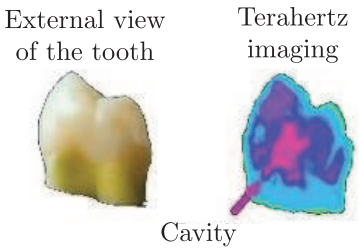

Figure 1.2: Terahertz radiography of a decayed tooth [TeraView 10].

Other medical applications have been revealed that are essentially oriented on imaging (organes, cancers, skin abnormalities) or molecule analysis such as DNA. Nevertheless, potential hazards and health effects of THz exposure should be monitored carefully, particularly since some research results suggest induction of genomic instability [Dabouis 09].

1.2.2 Industrial applications

The industrial applications of THz waves are concentrated around the properties of transparency of some materials such as epoxy which is used for the packaging of many integrated components. It is a promising method for a non-destructive control of microelectronic components. An example is shown in figure 1.3 which represents the internal image of a packed component.

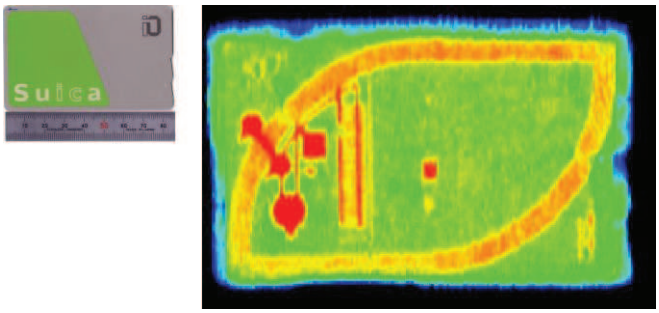

Figure 1.3: Non-destructive control of an electronic RFID tag through the packaging (Reproduced with the permission of the RIKEN Sendai Laboratory).

Another industrial application of THz waves is for gas sensing since some gases can have their specific spectroscopic signatures in this frequency range. Some research has also been made for food safety inspection with the THz waves [Shen 09].

One of the most popular application of the THz frequencies is for safety [Kemp 03]. There is an exponential increase of interest since last airplane hijacking events that really developed the research in that way. New machines are put in operation in airports (one of these can be seen in figure 1.4) using higher frequencies as an improvement of accuracy and resolution. These machines allow to watch through the clothes and detect weapons or drugs, like X-rays can do, but with the advantage of being able to distinguish materials from each other. An example of an image realized by this technique can be seen in figure 1.5.



Figure 1.4: Whole-body imaging system developped by L-3 communications®.

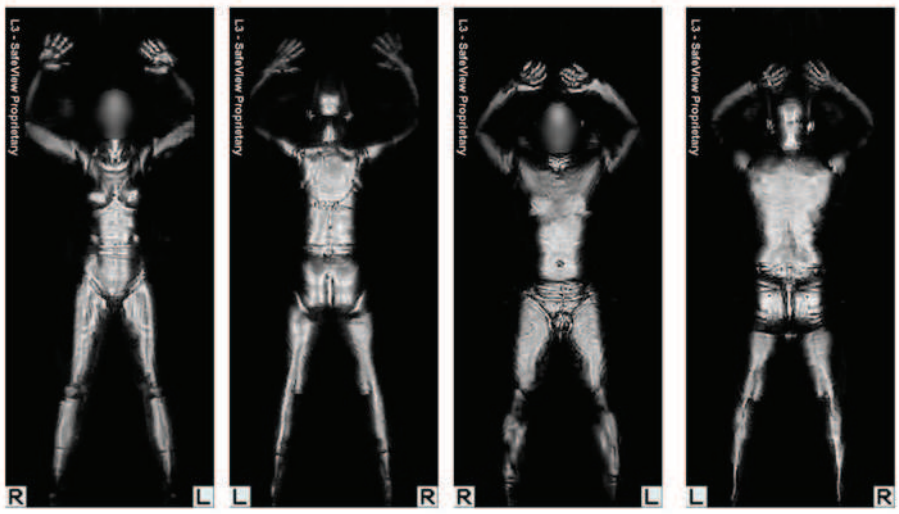

Figure 1.5: Example of whole-body imaging (United States Transportation Security Administration picture): every cloth becomes clear, and nothing can be kept secret.

1.2.3 Other applications

Another field of application of the THz waves is in telecommunications regarding to Shannon's law [Shannon 49] which predicts a possible increase of the data flow with the frequency. A very-high flow rate short-distance wireless link is then possible in this domain of frequencies, substituting the present WiFi®. Lastly, cosmic observations in this frequency domain brings new informations which are useful to understand our universe. An illustration of such observations is shown in figure 1.6.

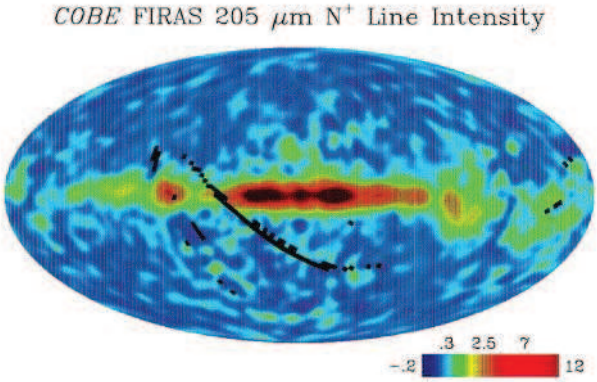

Figure 1.6: Projection of the full sky in Galactic coordinates at a frequency of 1.4611 THz obtained with the far infrared absolute spectrometer (FIRAS), the scale corresponds to the emission intensity in $nW.m^2.sr^{-1}$ [Fixsen 99].

1.3 State of the art

Since the THz frequency domain lies between the microwaves (generated by electronic devices) and the mid-infrared (where optical sources exists), both domains can be investigated to create new devices (sources and detectors) able to work in this spectral region [Dragoman 04, Miles 00] using electronic or optical skills, whatsoever a direct or indirect way of generating the THz signal.

1.3.1 Direct generation of THz radiations

1.3.1.1 Electronic devices adapted for THz

Starting from existing electronic devices, researchers try to adapt the technologies for higher frequencies or to develop new devices able to generate THz electric fields from different physical phenomena. Here is a brief description of the main electronic devices used to generate THz frequencies.

Gunn diode

Gunn diode has an ability to act, under certain conditions, as a negative differential resistance. This phenomenon is due to the decrease of electronic mobility when the electrons change of conduction valley. At low electric field (region I of figure 1.7), the conduction of electrons occurs in the Γ valley, but at some point, when the electric field is increased, the energy of electrons is sufficient to reach the L valley where they have a higher effective mass, and consequently, a lower mobility. As a consequence the current-voltage curve of the diode presents a decrease and a negative differential resistance (region II on figure 1.7).

It is easy to use this feature for generating oscillations at very high frequencies. The limit in term of frequency is mainly due to the mobility of carriers in the diode. As an example, it is possible nowadays to obtain on indium-phosphide (InP) substrates frequencies higher than 100 GHz with up to 100 mW of power emission. It is also possible to use upper harmonics to go higher in frequency but with an inescapable big loss of generated power [Savelli 96, Khalid 07]. The drawback of this component is the lack of frequency tune because the frequency is set by the length of the diode.

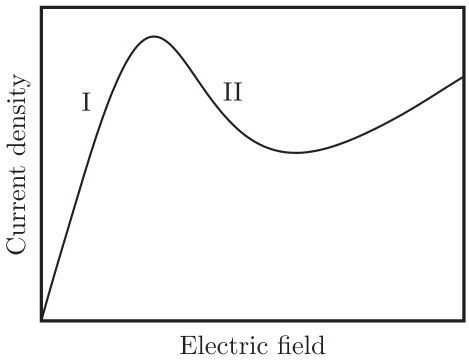

Figure 1.7: Current-electric field characteristics of a gunn diode [Savelli 96].

Tunnel effect diode

This type of diode presents a negative differential resistance under particular biases. This property is due to quantic effects during carriers displacements into the diode. This phenomenon is understandable by looking at the inside scheme of the tunnel effect diode: as shown in the figure 1.8, this particular diode is built with two potential gates used to create a quantum well in the opposite direction of the electrons displacement.

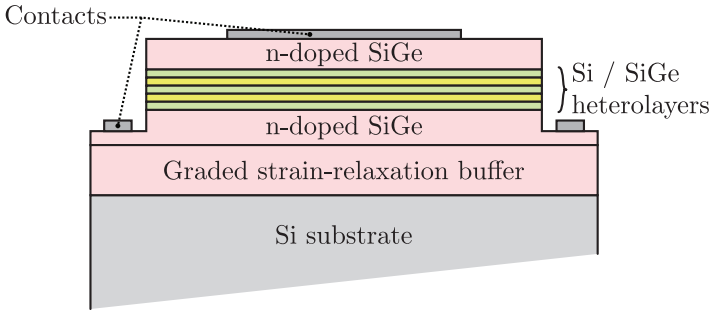

Figure 1.8: Typical layers scheme of a SiGe resonnant tunnel effect diode.

As we increase the bias of the diode, the electrons begin to cross the quantum well gates to finally reach the optimal bias corresponding to the alignment of the Fermi injection level with the first energy level inside the quantum well. If the bias voltage is increased, the number of electrons decrease in the channel, and so does the current. As a consequence, a negative differential mobility occurs in this domain of bias as shown in figure 1.9.

Fast transistors

Recent investigations reveal that it is possible to realize some ultra-fast transitors able to generate or

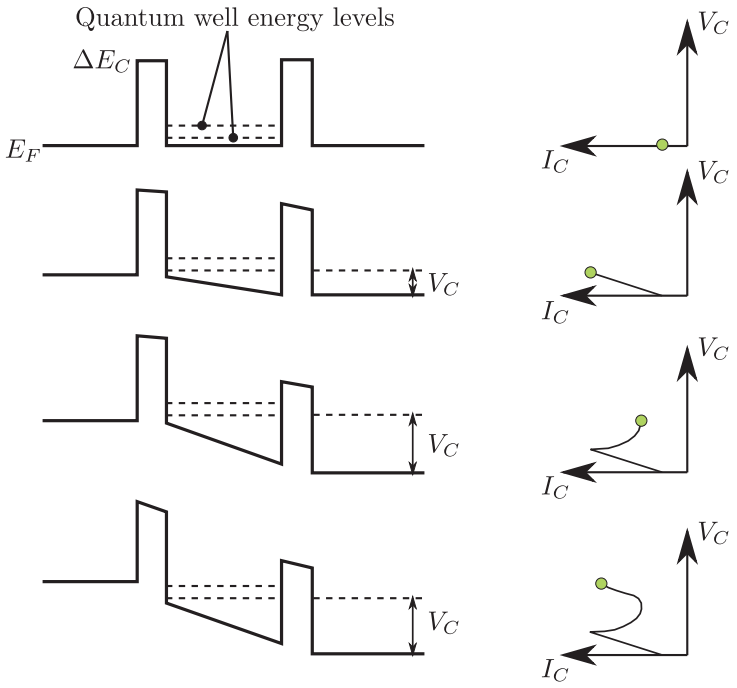

Figure 1.9: Step by step building of the current-voltage characteristics of a resonant tunnel effect diode [Savelli 96]. Vc is the bias voltage applied on the diode, E_F is the Fermi injection level and ΔE_c is the quantum well gate energy.

detect frequencies in the THz frequency domain. Two type of structures are preferred: high electron mobility transistors (HEMT) and heterojunction bipolar transistors (HBT).

HEMTs are field-effect transistors in which the donor atoms are placed outside the channel to limit interaction between carriers and ionized impurities. This trick combined with high-mobility materials such as GaAs or InP create a very fast carriers transit in the channel. A typical scheme of such a transistor is shown in figure 1.10. One can see that the donor atoms are placed in the δ-doping layer separated from the channel by a spacer layer built to limit far-interaction of ionized impurities with carriers of the channel.

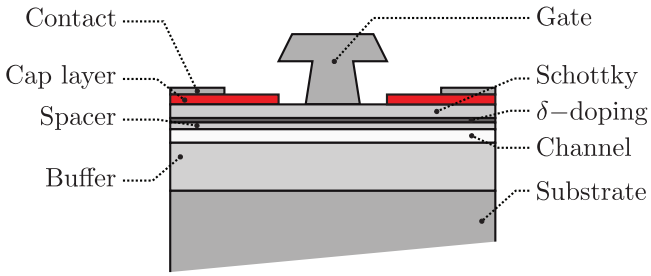

Figure 1.10: Typical layer scheme of a HEMT.

Regarding the HBT, it is an evolution of the traditional bipolar transistors, with the objective of obtaining higher frequencies. The principle of these devices is to add a heterojunction to limit the injection of holes in the emitter region. Thus, it is possible to increase the base doping and by consequence to reduce the base resistance. The HBT has the vertical structure shown in figure 1.11, and recent cut-off frequency limits for this kind of transistors is around 710 GHz for InP/InGaAs technology [Hafez 05] and 510 GHz for Si/SiGe technology (CMOS compatible) [Krithivasan 06].

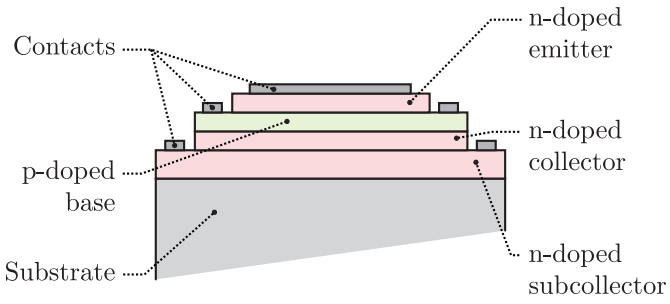

Figure 1.11: Typical layer scheme of a HBT.

1.3.1.2 Optical devices adapted for THz

Apart from electronic approach, another way to generate THz frequencies is to start from existing optical technologies and adapt them to increase their wavelength. In that section, there is a brief description of some optical devices used to generate radiations in this spectral range.

Quantum cascade lasers

One of the most popular optical device adapted for the generation of THz frequencies is a quantum cascade laser [Kohler 02, Tredicucci 04]. It is a heterostructure made of a succession of building blocks: each one is composed of an injection and an active region as illustrated in figure 1.12. In the active region, the electron stimulates the generation of a photon by making a transition from upper to lower energy level while in the injection region they are injected from the lower level of the last block to the excited one of the next block active region.

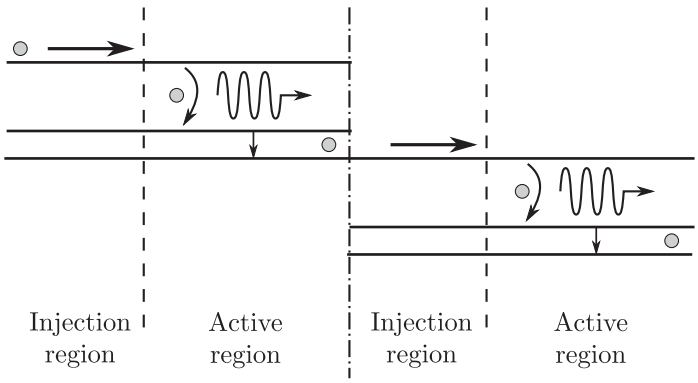

Figure 1.12: Schematic picture of the energy levels in two adjacent blocks of a quantum cascade laser. The straight arrows shows the flow of electrons through the heterostructure while the oscillating arrows illustrate the photon emission in the active region.

The main advantage of this method is to produce powers in the mW range. However, some drawbacks exist: the frequency is set by the heterostructure, and by consequence, is not tunable, and the operation at room-temperature is still not possible. Till now, the minimum frequency obtained with quantum cascade lasers is 1.39 THz [Scalari 06] up to a heat sink temperature of 40 K.

P-germanium lasers

Germanium-based lasers use the transitions between different energy levels in the valence band. The advantage of this source is its wide range of tunability (from 1 up to 4 THz) but the drawbacks are the

very strong electric and magnetic fields applied on it. Due to heating effects, it is not able to generate waves continuously (up to 1 ms) [Hubers 05], and it has to be cooled down to liquid helium temperatures to operate.

1.3.2 Indirect generation of THz radiations

An alternative method to generate THz frequencies is to use an existing source in a different frequency domain, such as infrared or radio-frequencies (RF), and use non-linearities of some devices to convert the initial frequency to the THz domain.

Frequency conversion

One of the ways to obtain THz frequencies is to start from a RF input source (stabilized frequency synthesizer), and use some non-linear device which can multiply the frequency. This can be achieved by using components such as the varactor and varistor-modes of GaAs Schottky diodes. The latter technology is able to generate frequencies up to 2.7 THz [Martin 01,Ward 08]. There are many advantages of choosing this technology to generate THz waves such as the accuracy in term of frequency directly related to the accuracy of the RF source, the available power over -25 dBm (≈ 3 µW) at 1.5 THz and the reliability.

Photomixing

One of the most popular technique to obtain THz frequencies is the photomixing source: as a proof of popularity, many manufacturers sell it for research as well as for industry. To create such a source, the technique is to focus the optical signal generated by two continuous-wave lasers of near wavelengths with identical polarization on a photomixing antenna (a biased dipole antenna), as shown in figure 1.13. The generated frequency is equal to a beating frequency, which is simply equal to the difference of both lasers frequencies: $\nu_{generated} = \nu_2 - \nu_1$, ($\nu_i = \frac{c}{\lambda_i}$), where c is the velocity of light in vacuum, and ν_1, ν_2, λ_1 and λ_2 are, respectively, the frequencies, and wavelengths of the two lasers. By consequence, it is easy to tune the generated frequency by simply tuning one or both wavelengths of the lasers: for example, this can be simply achieved by tuning the temperature of a distributed feedback (DFB) laser. The available power of this kind of device is about 1 µW, and the advantages of this technique are the ability to operate continuously at room-temperature, to be monochromatic, and tunable within a large frequency domain [Ito 05].

This device is described in detail in the section 4.2.1.2 since this is one of the devices we have been using.

1.3.3 Detectors

In addition to the bolometer which is very sensitive in a large domain of frequencies but has to be cooled, some other devices able to detect THz signal exists. Some of them are detailed in the following sub-sections.

1.3.3.1 Heterodyne detection

It is possible to detect the THz frequencies by using a heterodyne detection, which can transpose the high frequency (HF) spectrum to lower one by multiplying the signal with a close-frequency local

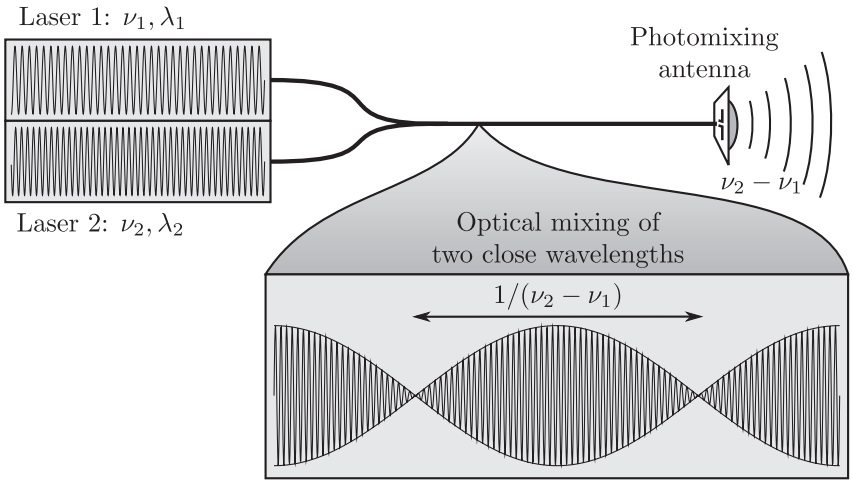

Figure 1.13: Illustration of the mixing of two laser signals of close wavelengths; the frequency of the envelope is equal to the difference of frequencies of the two lasers, and by consequence this is the frequency generated by the photomixing antenna.

oscillator (LO). Thus, the transposed signal will be easily detectable in a classical RF band. For example, these detections have been used with a QCL as a LO to detect frequencies up to 3 THz [Richter 08, Lee 08].

This kind of detection needs cooling at liquid helium temperatures to operate, but recent publication [Marinchio 10] shows a possible room temperature heterodyne way to detect THz frequencies based on the simultaneous optical and electronic excitation of plasma waves in HEMTs. In this case, the optical beating is acting as a LO and the non-linear device is used to mix the two waves.

1.3.3.2 Electro-optical sampling detection

Two different physical effects are possible for this kind of detection [Coutaz 08].

The Pockels effect

This detection is based on the principle of birefringence in an electro-optical crystal due to the THz electric field. Thus, it is possible to geometrically align the crystal in order to rotate the polarization of an incident optical beam with the value of the THz electric field. The measurement of this polarization rotation is by consequence an image of the incident electric field.

The Franz-Keldysh effect

Semiconductors have a very sharp threshold absorption as a function of an incident optical beam energy. This means that if we lineary decrease the wavelength of an input optical beam, there is a wavelength value from which the device becomes opaque for the incident beam; this is due to absorption in the material. The energy threshold value is equal to the forbidden energy band gap. In *classical* (direct band-gap) III/V material such as GaAs or InP, the threshold shape depends on the applied electric field. As a consequence, the refractive index of the material depends on the electric field as one can see in figure 1.14. This phenomenon, called the Franz-Keldysh effect can be used, as the Pockels' effect to sample a fast variating incident electric beam down to sub-picoseconds time domain.

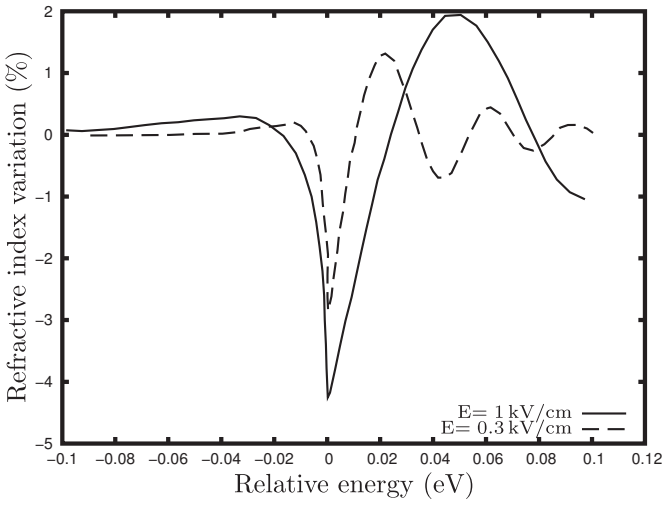

Figure 1.14: Refractive index variations induced by different electric field values in InP as a function of relative photon energy ($\hbar\omega - E_g$, where $\hbar$ is the reduced Planck constant, ω is the photon angular frequency, and E_g is the band gap energy of InP) [Bennett 87].

1.4 Summary

Many studies show that potential applications of THz frequencies are huge, but the lack of devices working in the THz frequency domain is still limitating. Our interest is to use a physical phenomenon (the optical phonon transit-time resonance) to create inovating components which will fill in a part of the so-called *THz gap*. One of these physical phenomenon will be described in the next chapter since it will be exploited in the novel devices we develop in our laboratory. These new devices have been fabricated within a french national project, and experimental results are detailed in the part III.

Chapter 2

The optical phonon transit time resonance in gallium nitride: from theory to experiment



The physical mechanism involved in the terahertz amplification of our study is based on particular electron transport properties of III/V semiconductor materials such, and, in particular, nitrides. The first part of this chapter will be dedicated to the theoretical analysis of electron transport in such materials. After the description of the main features of such a transport, we will explain how these properties can lead to the amplification of electromagnetic waves using the so-called optical phonon transit time resonance. Finally, we will extract the parameters needed for the fabrication process as well as for the experimental verification of the amplification mechanism.

2.1 Electronic transport and the Boltzmann equation

Conventional device analysis begins by assuming that carriers behave as classical particles which obeys Newton's laws. A more fundamental treatment describes the electron by its wave function, $\Psi(\mathbf{r},t)$, which is obtained by solving the Schrödinger equation,

$$i\hbar\frac{\partial\Psi}{\partial t} = -\frac{\hbar^2}{2m_0}\nabla^2\Psi + [E_{C0}(\mathbf{r}) + U_C(\mathbf{r}) + U_S(\mathbf{r},t)]\Psi(\mathbf{r},t)\ , \tag{2.1}$$

where $\hbar$ is the reduced Planck constant, and m_0 the electron mass. Three different potentials appear in the wave equation; the first, $E_{C0}(\mathbf{r})$, describes potentials that are built-in or applied to the device (external electric and magnetic fields, and energy bands). The second potential is the crystal potential, $U_C(\mathbf{r})$, which describes the electrostatic potential due to atoms and the average of other carriers. Finally, $U_S(\mathbf{r},t)$ is a scattering term due to random variations in potential caused, for instance, by ionized impurities or by lattice vibrations (phonons).

In principle, we should analytically solve this equation to determine the behavior of every electron, and, at a macroscopic scale, the studied device. Unfortunately, even if a few situations allow an analytical solution, in most of the cases, a numerical solution of the Schrödinger equation will be the only way to solve a given problem.

2.1.1 The Boltzmann equation

For any physical system, the distribution function $f(\mathbf{r},\mathbf{v},t)$ describes the probability of presence of a particle at the space position $\mathbf{r}$ with a velocity $\mathbf{v}$ at time t [Palermo 04, Lundstrom 00]. As a consequence, the number of particles present in the phase space element $d^3\mathbf{r}d^3\mathbf{v}$ at time t verifies:

$$dN(\mathbf{r},\mathbf{v},t) = f(\mathbf{r},\mathbf{v},t)d^3\mathbf{r}d^3\mathbf{v}\ . \tag{2.2}$$

The particle density n present at $\mathbf{r}$ at time t is given by:

$$n(\mathbf{r},t) = \int_v f(\mathbf{r},\mathbf{v},t)d^3\mathbf{v}\ , \tag{2.3}$$

where the integration is extended to all velocities. This equation can be written as:

$$\int_v \frac{f(\mathbf{r},\mathbf{v},t)}{n(\mathbf{r},t)}d^3\mathbf{v} = 1\ , \tag{2.4}$$

allowing us to introduce the ratio

$$\frac{f(\mathbf{r},\mathbf{v},t)}{n(\mathbf{r},t)}\ , \tag{2.5}$$

as a normalized density of probability. Thus, every particles physical property defined by the quantity $A(\mathbf{r}, \mathbf{v}, t)$ can be averaged thanks to the normalized density of probability with the following equation:

$$\bar{A}(\mathbf{r}, t) = \frac{\int_v A(\mathbf{r}, \mathbf{v}, t) f(\mathbf{r}, \mathbf{v}, t) d^3\mathbf{v}}{\int_v f(\mathbf{r}, \mathbf{v}, t) d^3\mathbf{v}} \, . \tag{2.6}$$

Hence, the distribution function gives full information of the macroscopic behavior of the considered system through the averaged physical properties.

In other terms, the distribution function is the keystone for the microscopic description of every electronic device behavior. However its knowledge represents a quite complex task to be solved numerically in the case of realistic devices. Many numerical methods exist to describe electronic transport (drift-diffusion, hydrodynamic, Monte Carlo, direct solution of the Boltzmann equation) with the objective to find the approximate solution of the equation which describes the evolution of the distribution function: the Boltzmann equation.

Let us consider a gas composed of carriers subject to an electric field $\mathbf{\Sigma}$. These carriers traverse in a crystalline structure and by consequence undergo interactions with it. Thus, the distribution function reflects the effects of the electric field $\mathbf{\Sigma}$ plus the scattering interactions of the structure.

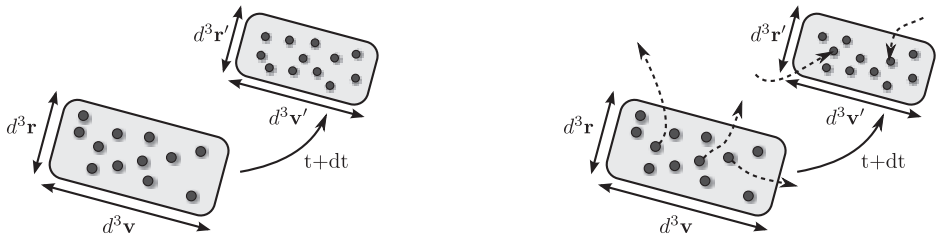

(a) Collision-less evolution

(b) Evolution with collisions

Figure 2.1: Evolution in the phase space of a system between times t and $t + dt$.

For a better understanding of the situation, one can have a look at the picture 2.1(a) illustrating the phase space. If no collision occurs between time t and $t + dt$, then all the carriers included in a volume $d^3\mathbf{r}d^3\mathbf{v}$ will be transfered to the volume $d^3\mathbf{r}'d^3\mathbf{v}'$, and the vectors $\mathbf{r}$, $\mathbf{r}'$, $\mathbf{v}$ and $\mathbf{v}'$ will be linked by the relations:

$$\mathbf{r}' = \mathbf{r} + d\mathbf{r} = \mathbf{r} + \frac{\partial \mathbf{r}}{\partial t} dt \, , \tag{2.7}$$

and

$$\mathbf{v}' = \mathbf{v} + d\mathbf{v} = \mathbf{v} + \frac{\partial \mathbf{v}}{\partial t} dt \, . \tag{2.8}$$

The conservation of carriers number can be written as (neglecting generation-recombination processes) :

$$f\left(\mathbf{r} + \frac{\partial \mathbf{r}}{\partial t} dt, \mathbf{v} + \frac{\partial \mathbf{v}}{\partial t} dt, t + dt\right) d^3\mathbf{r}' d^3\mathbf{v}' - f(\mathbf{r}, \mathbf{v}, t) d^3\mathbf{r} d^3\mathbf{v} = 0 \, . \tag{2.9}$$

At first order, this equation develops into:

$$\frac{\partial f(\mathbf{r}, \mathbf{v}, t)}{\partial t} + \frac{\partial \mathbf{r}}{\partial t} \frac{f(\mathbf{r}, \mathbf{v}, t)}{\partial \mathbf{r}} + \frac{\partial \mathbf{v}}{\partial t} \frac{f(\mathbf{r}, \mathbf{v}, t)}{\partial \mathbf{v}} = 0 \, . \tag{2.10}$$

Although

$$\frac{\partial \mathbf{r}}{\partial t} = \mathbf{v} \,, \tag{2.11}$$

and

$$\frac{\partial \mathbf{v}}{\partial t} = \mathbf{a} = \frac{q\boldsymbol{\Sigma}}{m^*} \,, \tag{2.12}$$

where $\mathbf{a}$ is the acceleration, q is the charge and m^* is the effective mass of the carriers. These magnitudes can be inserted in equation (2.10), and one obtains the *collision-less Boltzmann equation*:

$$\boxed{\frac{\partial f(\mathbf{r},\mathbf{v},t)}{\partial t} + \frac{\partial f(\mathbf{r},\mathbf{v},t)}{\partial \mathbf{r}} + \frac{q\boldsymbol{\Sigma}}{m^*}\frac{\partial f(\mathbf{r},\mathbf{v},t)}{\partial \mathbf{v}} = 0}_{coll.less} \,. \tag{2.13}$$

If collisions are taken into account, as illustrated in figure 2.1(b), some particles that are initially in the volume $d^3\mathbf{r}d^3\mathbf{v}$ at time t may undergo a collision and be evicted of the final volume $d^3\mathbf{r}'d^3\mathbf{v}'$ at time $t+dt$. Analogously, particles starting from points of the phase space different from $d^3\mathbf{r}d^3\mathbf{v}$ may be scattered into the final volume $d^3\mathbf{r}'d^3\mathbf{v}'$ during the time interval dt due to some interaction. As a consequence, the number of particles between t and $t+dt$ can differ, and the Boltzmann equation (2.13) can be rewritten as:

$$\boxed{\frac{\partial f(\mathbf{r},\mathbf{v},t)}{\partial t} + \frac{\partial f(\mathbf{r},\mathbf{v},t)}{\partial \mathbf{r}} + \frac{q\boldsymbol{\Sigma}}{m^*}\frac{\partial f(\mathbf{r},\mathbf{v},t)}{\partial \mathbf{v}} = \left.\frac{\partial f(\mathbf{r},\mathbf{v},t)}{\partial t}\right|_{coll}} \,, \tag{2.14}$$

where $\left.\frac{\partial f(\mathbf{r},\mathbf{v},t)}{\partial t}\right|_{coll}$ is the variation of the distribution function due to scattering processes. This expression describes the out-flow of carriers from $d^3\mathbf{r}d^3\mathbf{v}$ as well as the in-flow of carriers in $d^3\mathbf{r}'d^3\mathbf{v}'$ which don't come from $d^3\mathbf{r}d^3\mathbf{v}$. If $S(\mathbf{v},\mathbf{v}')$ is the transition probability from the initial quantum state $|\mathbf{r},\mathbf{v}\rangle$ to the final quantum state $|\mathbf{r},\mathbf{v}'\rangle$, the collision term becomes:

$$\left.\frac{\partial f(\mathbf{r},\mathbf{v},t)}{\partial t}\right|_{coll} = \frac{\Omega}{8\pi^3}\int_{\mathbf{v}'}\left\{S(\mathbf{v}',\mathbf{v})f(\mathbf{r},\mathbf{v}',t)[1-f(\mathbf{r},\mathbf{v},t)] - S(\mathbf{v},\mathbf{v}')f(\mathbf{r},\mathbf{v},t)[1-f(\mathbf{r},\mathbf{v}',t)]\right\}d^3\mathbf{v}' \,, \tag{2.15}$$

where Ω is the semiconductor crystal volume. If $S(\mathbf{v},\mathbf{v}')$ is the transition probability from $|\mathbf{r},\mathbf{v}\rangle$ to $|\mathbf{r},\mathbf{v}'\rangle$, $f(\mathbf{r},\mathbf{v}',t)[1-f(\mathbf{r},\mathbf{v},t)]$ is the probability that simultaneously, initial state $|\mathbf{r},\mathbf{v}\rangle$ is occupied *and* final state $|\mathbf{r},\mathbf{v}'\rangle$ is free.

Thus, the Boltzmann equation is given by:

$$\frac{\partial f(\mathbf{r},\mathbf{v},t)}{\partial t} + \frac{\partial f(\mathbf{r},\mathbf{v},t)}{\partial \mathbf{r}} + \frac{q\boldsymbol{\Sigma}}{m^*}\frac{\partial f(\mathbf{r},\mathbf{v},t)}{\partial \mathbf{v}} = \frac{\Omega}{8\pi^3}\int_{\mathbf{v}'}\left\{S(\mathbf{v}',\mathbf{v})f(\mathbf{r},\mathbf{v}',t)[1-f(\mathbf{r},\mathbf{v},t)] - S(\mathbf{v},\mathbf{v}')f(\mathbf{r},\mathbf{v},t)[1-f(\mathbf{r}\,,\mathbf{v}',t)]\right\}d^3\mathbf{v}' \,. \tag{2.16}$$

In the case of low carrier concentration the two terms in square brackets can be usually neglected. It is obvious that a direct solution of equation (2.16) is extremely difficult excluding a very few particular cases. Some assumptions can be used to simplify the resolution, such as the relaxation time approximation, but this is not the object of this thesis and it will not be described here. The details can be found elsewhere [Hamaguchi 01].

Electronic transport is thus mainly governed by the interactions carriers may undergo during their movement inside a device. The next sections describe how to quantitatively evaluate these effects.

2.1.2 The Fermi's golden rule

As we consider a one dimension problem, the Schrödinger equation (2.1) can be written as:

$$[H_0 + U_S(z,t)]\Psi(z,t) = i\hbar\frac{\partial\Psi(z,t)}{\partial t}\,, \tag{2.17}$$

where z is the spatial coordinate (for simplicity we will consider a one dimensional treatment), and H_0 is the Hamiltonian operator for the unperturbed system (i.e.: without scattering potential). We assume that the unperturbed problem:

$$H_0\psi_k = E(k)\psi_k \tag{2.18}$$

$$\Psi_k^0(z,t) = \psi_k(z)e^{-iE(k)t/\hbar}\,, \tag{2.19}$$

has been solved. These solutions form a complete orthonormal set, so we can express the solution to the perturbed problem as a linear combination of them:

$$\begin{aligned}\Psi(z,t) &= \sum_k c_k(t)\Psi_k^0(z,t)\\ &= \sum_k c_k(t)\psi_k(z)e^{-iE(k)t/\hbar}\end{aligned} \tag{2.20}$$

Now consider the situation sketched in figure 2.2 – an electron wave packet centered at $k = k_0$ enters, interacts with $U_S(z,t)$, and emerges at k_0'. At $t = 0$ we have:

$$c_{k_0}(t=0) = 1\,, \tag{2.21}$$

$$c_k(t=0) = 0, \qquad \forall k \neq k_0\,. \tag{2.22}$$

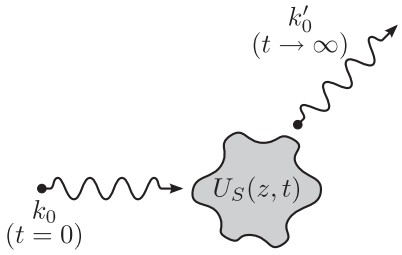

Figure 2.2: Scattering of a wave packet centered at $k = k_0$ to one centered at $k = k_0'$.

After the scattering event, the probability of finding the electron with wave vector, k_0', is:

$$P(k = k_0') = \lim_{t\to\infty}\left|c_{k_0'}(t)\right|^2\,, \tag{2.23}$$

so the scattering rate from k_0 to k_0' is:

$$S(k_0, k_0') = \lim_{t\to\infty}\frac{\left|c_{k_0'}(t)\right|^2}{t}\,. \tag{2.24}$$

(To allow $t \to \infty$ in these expressions, without another collision occurring, collisions must be infrequent.)

To find the value of every c_k, we insert equation (2.20) in (2.17) to obtain:

$$U_S(z,t)\sum_k c_k(t)\psi_k e^{-iE(k)t/\hbar} = i\hbar\sum_k \frac{\partial c_k}{\partial t}\psi_k e^{-iE(k)t/\hbar} \,. \tag{2.25}$$

Next we multiply both side by the conjugate quantity, integrate over position, and make use of the orthogonality of eigenfunctions, to find:

$$i\hbar\frac{\partial c_{k'_0}}{\partial t} = \sum_k H_{k'_0 k} c_k(t) e^{-i[E(k'_0)-E(k)]t/\hbar} \,, \tag{2.26}$$

where

$$\boxed{H_{k'_0 k_0}(t) \equiv \int_{-L/2}^{+L/2} \psi_{k'_0}(z) U_S(z,t) \psi_{k_0}(z) dz} \,, \tag{2.27}$$

is the matrix element of the scattering potential between states k'_0 and k. We have normalized the wave-functions over a length L, which becomes a volume, Ω, in three dimensions.

Since we assume that the scattering is weak, $c_{k_0} \simeq 1$ for all time, and the other c_k $(\forall k)$ are always small. With this approximation (the so-called Born approximation) the sum in equation (2.26) can be approximated by one term as:

$$i\hbar\frac{\partial c_{k'_0}}{\partial t} = H_{k'_0 k_0}(1) e^{-i[E(k'_0)-E(k_0)]t/\hbar} \,, \tag{2.28}$$

which can be integrated to find:

$$c_{k'_0}(t) = \frac{1}{i\hbar}\int_0^t H_{k'_0 k_0} e^{-i[E(k'_0)-E(k_0)]t/\hbar} dt + c_{k'_0}(0) \,. \tag{2.29}$$

Because the final state k'_0 was empty at $t = 0$, $c_{k'_0}(0) = 0$.
Let us specify the time-dependent matrix element as:

$$H_{k'_0 k_0}(t) = H^{a,e}_{k'_0 k_0} e^{\mp i\omega t} \,. \tag{2.30}$$

(The significance of the a and e superscripts which apply the minus and plus signs respectively will be explained shortly.) As a consequence, the c_k coefficients can be calculated from equation (2.29):

$$c_{k'_0}(t) = \frac{1}{i\hbar} H^{a,e}_{k'_0 k_0} \frac{e^{-i[E(k'_0)-E(k_0)]t/\hbar} - 1}{i[E(k'_0) - E(k_0) \mp \hbar\omega]/\hbar} \,. \tag{2.31}$$

When we define:

$$\Lambda = [E(k'_0) - E(k_0) \mp \hbar\omega]/\hbar \,, \tag{2.32}$$

then the equation (2.31) can be written as:

$$c_{k'_0}(t) = \frac{1}{i\hbar} H^{a,e}_{k'_0 k_0} e^{i\Lambda t/2} \frac{\sin(\Lambda t/2)}{\Lambda t/2} t \,. \tag{2.33}$$

Now, according to equation (2.24), we find the transition rate as:

$$S(k_0, k'_0) = \lim_{t\to\infty} \frac{\left|H^{a,e}_{k'_0 k_0}\right|^2}{t\hbar^2} \left[\frac{\sin(\Lambda t/2)}{\Lambda t/2}\right]^2 t^2 \,. \tag{2.34}$$

For large t, the function in brackets is sharply peaked near the origin and looks like a δ-function (also known as the Dirac function). The strength of the δ-function is determined from the area under the curve. Recall that

$$\int_{-\infty}^{+\infty} \frac{\sin^2(x)}{x^2} dx = \pi \,, \tag{2.35}$$

so $\sin^2(x)/x^2$ can be replaced by $\pi\delta(x)$. Using $x = \Lambda t/2$, we find the replacement:

$$\lim_{t\to\infty} \left[\frac{\sin(\Lambda t/2)}{\Lambda t/2}\right]^2 = \frac{2\pi}{t}\delta(\Lambda) \,, \tag{2.36}$$

which can be inserted in the equation (2.34) to find:

$$\begin{aligned} S(k_0, k_0') = &\frac{2\pi}{\hbar} \left|H^a_{k_0' k_0}\right|^2 \delta\left(E(k_0') - E(k_0) - \hbar\omega\right) \\ &+ \frac{2\pi}{\hbar} \left|H^e_{k_0' k_0}\right|^2 \delta\left(E(k_0') - E(k_0) + \hbar\omega\right) \end{aligned} \,. \tag{2.37}$$

The δ-function in equation (2.37) simply expresses conservation of energy and applies when scattering is weak, so that time can approach infinity in equation (2.34). For frequent scattering, there is an uncertainty in the final energy, given by $\Delta E \Delta t \geq \hbar$, which is known as *collisional broadening*. The first term in equation (2.37) contributes when $E(k_0') = E(k_0) + \hbar\omega$; an energy $\hbar\omega$ has been absorbed. The second contributes when $E(k_0') = E(k_0) - \hbar\omega$; an energy $\hbar\omega$ has been emitted.

Equation (2.37) is the basic result of scattering theory that we will apply to the carriers in the semiconductors. The result is known as *Fermi's Golden Rule*. To apply the Golden Rule, the scattering potential must be identified so that the matrix element can be evaluated. For electrons in semiconductor, the wave functions for the unperturbed problem are Bloch waves. When the matrix element described in equation (2.27) is evaluated for Bloch waves, one finds [Nag 80]:

$$H_{k'k} = I(k, k') U_S(k - k') \,, \tag{2.38}$$

where

$$I(k, k') \equiv \left| \int_{cell} u^*_{k'}(z) u_k(z) dz \right|^2 \,, \tag{2.39}$$

is the overlap factor between the periodic part $u_k(z)$ of the Bloch wave functions of initial and final states. This factor only depends on the geometry of the semiconductor crystal and not on the scattering itself. For a parabolic band, $I(k, k') \simeq 1$ [Nag 80].

$$U_S(k - k') = \int_{-L/2}^{+L/2} \frac{e^{-ik'z}}{\sqrt{L}} U_S(z) \frac{e^{+ik'z}}{\sqrt{L}} dz \,. \tag{2.40}$$

Finally, in the case of a parabolic band semiconductor, the matrix element can be calculated by the formula

$$H_{k'k} \simeq \frac{1}{L} \int_{-L/2}^{+L/2} e^{-ik'z} U_S(z) e^{+ik'z} dz \,, \tag{2.41}$$

which can be generalized for a 3D case

$$\boxed{H_{\mathbf{p}'\mathbf{p}} = \frac{1}{\Omega} \int_\Omega e^{-i\mathbf{p}'\cdot\mathbf{r}/\hbar} U_S(\mathbf{r}) e^{+i\mathbf{p}'\cdot\mathbf{r}/\hbar} d^3r} \,, \tag{2.42}$$

From now, the challenging task to evaluate the global behavior of a semiconductor, is to be able to calculate the scattering potential of every possible interaction that a carrier may undergo during its transition in the considered device.

2.2 Carrier scatterings in semiconductors

The electronic transitions of interest in charge transport in semiconductors can be classified as intravalley transitions, when the initial and final states of the electron lie in the same valley, or intervalley transitions, when the initial and final states lie in different valleys. For the case of holes, transitions are correspondingly called intraband and interband. In the case of our problem, we will not consider hole transport, because in both bulk and quantum-well, electrons will prevail.

The most important scattering sources which determine these transitions are:

– phonons;
– defects;
– impact-ionization;
– carrier-carrier.

The interaction of phonons with charge carriers can be due to the deformation of the otherwise perfect crystal produced by the phonons, or to the electrostatic forces produced by the polarization waves which accompany the phonon. The first kind of mechanism, typical of covalent semiconductors, is called deformation-potential interaction for both acoustic and optical phonons. The electrostatic interaction, typical of polar materials, is called piezoelectric interaction for the case of acoustic phonons, and polar interaction for optical phonons. Often the attribute of piezoelectric or polar is given directly to the phonon involved. Thus we speak of piezoelectric phonons or polar optical phonons as we speak of intervalley phonons to indicate phonons which induce intervalley electron transitions.

Defects can arise in a crystal owing to dislocations of different types and geometries, to impurities (neutral or ionized) due to extra atoms, and to the random distribution of component atoms among available lattice sites in alloys.

Impact ionization occurs when the carrier energy is approximately above the energy gap of the semiconductor under investigation. Related to this kind of scattering is the possibility of charge carriers multiplication, a phenomenon which leads to the electronic breakdown of the material.

Finally, carrier-carrier interaction is a very difficult type of scattering to include in the model because it makes the Boltzmann equation nonlinear. As a general trend, the effect of this type of collision is, however, very limited under hot-electron conditions because of its electrostatic nature which results in a smaller efficiency at increasing carrier velocity. Figure 2.3 summarizes the various scattering mechanisms existing in cubic semiconductors.

2.2.1 Relaxation times

As we saw with the help of the Fermi's golden rule in section 2.1.2, if we know the matrix element $H_{\mathbf{p}'\mathbf{p}}$, we are able to calculate the transition rate, $S(\mathbf{p}, \mathbf{p}')$, which is the probability per unit time that a carrier with crystal momentum $\mathbf{p}$ scatters to a state with crystal momentum $\mathbf{p}'$, with the formula

$$S(\mathbf{p}, \mathbf{p}') = \frac{2\pi}{\hbar} \left| H_{\mathbf{p}'\mathbf{p}} \right|^2 \delta(E(\mathbf{p}') - E(\mathbf{p}) - \Delta E) \,, \tag{2.43}$$

where ΔE is the change in energy (if any) caused by the scattering event.

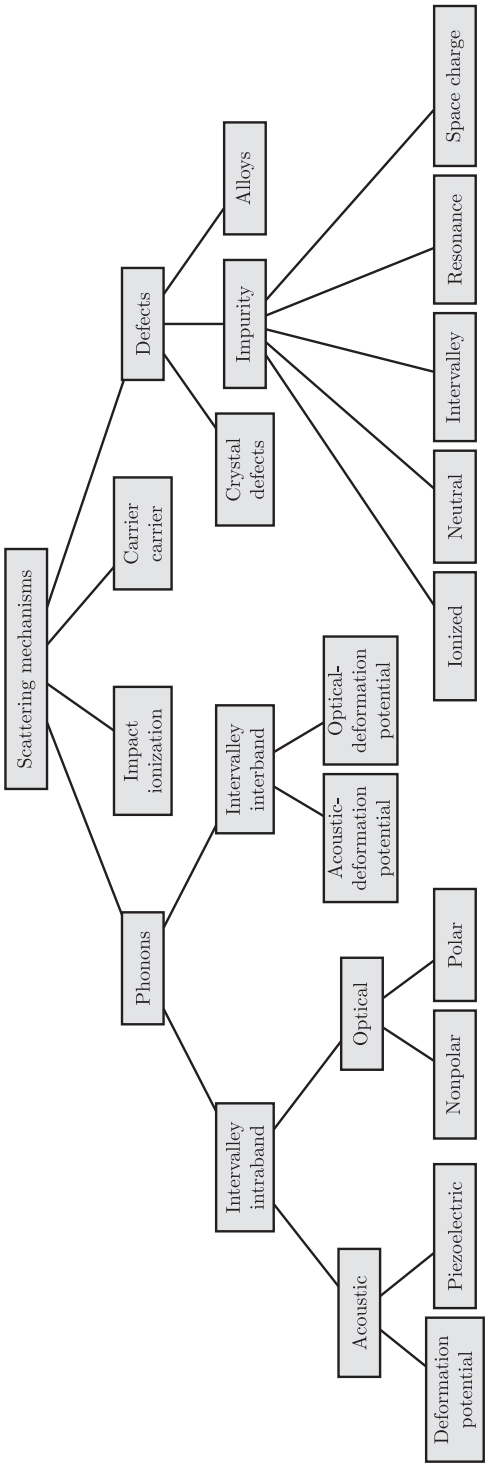

Figure 2.3: Scattering mechanisms in cubic semiconductors [Reggiani 85].

On an other hand, the scattering rate

$$\frac{1}{\tau(\mathbf{p}_0)} = \sum_{\mathbf{p}',\uparrow} S(\mathbf{p}_0, \mathbf{p}')[1 - f(\mathbf{p}')] \,, \tag{2.44}$$

is the rate at which carriers with a specific momentum $\mathbf{p}_0$ scatter to any other state. Alternatively, $\tau(\mathbf{p}_0)$ is the average time between collisions (also known as the lifetime of the state $\mathbf{p}_0$). The vertical arrow bellow the sum is to indicate that the sum over final states includes only those whose spin is parallel to that of the incident carrier (the scattering mechanisms we consider do not flip the carrier spin). The factor of $[1 - f(\mathbf{p}')]$ gives the probability of finding an empty final state. For a non-degenerate semiconductor, there is a high probability that the state at $\mathbf{p}'$ is empty, so equation (2.44) becomes

$$\frac{1}{\tau(\mathbf{p}_0)} = \sum_{\mathbf{p}',\uparrow} S(\mathbf{p}_0, \mathbf{p}') \,. \tag{2.45}$$

This sum is much easier to calculate because it does not depend on knowing how the states are occupied.

Some important scattering mechanisms are not isotropic. Instead, they tend to deflect carriers by small angles. In other words, even after $\tau(\mathbf{p}_0)$, the carriers can retain a memory of their incident momentum. To evaluate the rate at which the **z**-directed momentum is relaxed, we need to weight each collision by the fractional change in the **z**-directed momentum. The result is

$$\frac{1}{\tau_m(\mathbf{p}_0)} = \sum_{\mathbf{p}',\uparrow} S(\mathbf{p}_0, \mathbf{p}') \left(1 - \frac{p'_z}{p_{z0}}\right) = \sum_{\mathbf{p}',\uparrow} S(\mathbf{p}_0, \mathbf{p}') \left(1 - \frac{p'}{p_0}\cos\alpha\right) \,, \tag{2.46}$$

where α is the polar angle between the incident and scattered momenta as illustrated in figure 2.4(a). $\tau_m(\mathbf{p}_0)$ is known as the *momentum relaxation time*, and corresponds to the time required to randomize the momentum with a given scattering mechanism. We may also be interested in the time required to

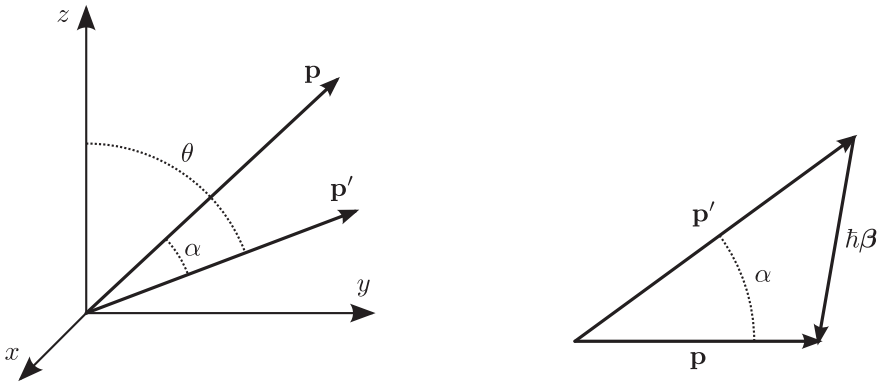

(a) Scattering event (b) Induced momentum change

Figure 2.4: Illustration of a scattering event showing the incident and scattered momenta and the polar angle, α. Definition of $\hbar\boldsymbol{\beta}$, the momentum change resulting from scattering.

dissipate carrier energy, in particular for the polar optical phonon, this time will be important to know how fast polar optical phonons are emitted by electrons. To find the energy relaxation rate, we weight

each collision by the fractional change in energy and find

$$\frac{1}{\tau_E(\mathbf{p}_0)} = \sum_{\mathbf{p}',\uparrow} S(\mathbf{p}_0, \mathbf{p}') \left(1 - \frac{E(\mathbf{p}')}{E(\mathbf{p}_0)}\right) , \tag{2.47}$$

where $\tau_E(\mathbf{p}_0)$ is the *energy relaxation time*.

In the next section, we will follow step by step the calculation of the scattering rates for ionized impurities scattering, and will directly give the results for deformation acoustic and polar optical phonon scatterings.

2.2.2 Scattering with ionized impurities

Carriers are scattered when they encounter the electric field of an ionized impurity. We might assume that the scattering potential is Coulombic,

$$U_S(\mathbf{r}) = \frac{q^2}{4\pi\varepsilon_r\varepsilon_0 r}, \tag{2.48}$$

but the ionized impurity attracts mobile carriers which *screen* the potential. The electrostatic potential due to both the ionized impurity and mobile carriers is found by solving Poisson's equation in spherical coordinates,

$$\frac{1}{r^2}\frac{d}{dr}\left(r^2\frac{dV}{dr}\right) = \frac{q}{\varepsilon_r\varepsilon_0}(n - N_D) , \tag{2.49}$$

where an n-type semiconductor has been assumed. Space charge neutrality dictates that $n = n_0 = N_D$ (with a corresponding electrostatic potential of $V = V_0$) on a macroscopic scale, but on a microscopic scale, perturbations in the potential and carrier density exist. By writing the potential and carrier density as $V = V_0 + \delta V$ and $n = n_0 + \delta n$ and substituting in equation (2.49), we find

$$\frac{1}{r^2}\frac{d}{dr}\left(r^2\frac{d\delta V}{dr}\right) = \frac{q\delta n}{\varepsilon_r\varepsilon_0}. \tag{2.50}$$

To find δn, recall that

$$n = N_C e^{[E_F - E_C(\mathbf{r})]/k_B T} , \tag{2.51}$$

for a non-degenerate semiconductor and that

$$E_C(\mathbf{r}) = \text{constant} - qV(\mathbf{r}), \tag{2.52}$$

so small perturbations in carrier density can be related to perturbations in the potential by

$$\delta n = \frac{\delta n}{\delta V}\delta V = \frac{qn_0}{k_B T}\delta V. \tag{2.53}$$

After inserting this result in Poisson's equation, we find

$$\frac{1}{r^2}\frac{d}{dr}\left(r^2\frac{d\delta V}{dr}\right) = \frac{q^2 n_0}{\varepsilon_r\varepsilon_0 k_B T}\delta V = \delta V / L_D^2, \tag{2.54}$$

where

$$L_D = \sqrt{\frac{\varepsilon_r\varepsilon_0 k_B T}{q^2 n_0}} , \tag{2.55}$$

is known as the *Debye length*.

The solution to equation (2.54),

$$\delta V = \frac{A}{r} e^{-r/L_D}, \tag{2.56}$$

shows that perturbations in potential decay exponentially with distance from the perturbation. If the perturbation is due to an ionized impurity, we should recover the coulombic potential as $r \to 0$, so

$$A = \frac{q^2}{4\pi\varepsilon_r\varepsilon_0}. \tag{2.57}$$

For an n-type semiconductor, therefore, the appropriate perturbing potential is the *screened Coulomb potential*,

$$\boxed{U_S(\mathbf{r}) = \frac{q^2}{4\pi\varepsilon_r\varepsilon_0 r} e^{-r/L_D}}. \tag{2.58}$$

On the other hand, when the mobile carrier density is low, as it is in the depletion region of a $p-n$ junction, the unscreened Coulomb potential (equation (2.48)) is used.

We now can evaluate the matrix element $H_{\mathbf{p}'\mathbf{p}}$ with the help of equation (2.42) as

$$H_{\mathbf{p}'\mathbf{p}} = \frac{1}{\Omega}\left(\frac{q^2}{4\pi\varepsilon_r\varepsilon_0}\right)\int_\Omega e^{-i\mathbf{p}'\cdot\mathbf{r}/\hbar}\left(\frac{e^{-r/L_D}}{r}\right)e^{+i\mathbf{p}'\cdot\mathbf{r}/\hbar}d^3r \tag{2.59}$$

or

$$H_{\mathbf{p}'\mathbf{p}} = \frac{1}{\Omega}\left(\frac{q^2}{4\pi\varepsilon_r\varepsilon_0}\right)\int_0^{2\pi} d\phi \int_0^{\pi}\int_0^{\infty} e^{-r/L_D}e^{i(\mathbf{p}-\mathbf{p}')\cdot\mathbf{r}/\hbar} r dr \sin(\theta) d\theta\ . \tag{2.60}$$

If we introduce the momentum change resulting from the scattering with an ionized impurity $\hbar\boldsymbol{\beta}$, as illustrated in figure 2.4(b), we have

$$\hbar\boldsymbol{\beta} = \mathbf{p}' - \mathbf{p} \tag{2.61}$$

and

$$\hbar\beta = 2p\sin\left(\frac{\alpha}{2}\right)\ , \tag{2.62}$$

which is due to the fact that ionized impurity scattering is elastic, and thus $p = p'$. As a consequence, equation (2.60) becomes

$$H_{\mathbf{p}'\mathbf{p}} = \frac{1}{\Omega}\left(\frac{q^2}{4\pi\varepsilon_r\varepsilon_0}\right)\int_0^{\infty}\int_0^{2\pi}\int_{-1}^{+1} r e^{-r/L_D}e^{-i\beta r\cos(\theta)} d(\cos\theta) d\phi dr\ . \tag{2.63}$$

The latter equation can be integrated to find

$$H_{\mathbf{p}'\mathbf{p}} = \frac{q^2}{\Omega\varepsilon_r\varepsilon_0}\frac{1}{\beta^2 + 1/L_D^2}\ . \tag{2.64}$$

According to equation (2.43), the transition rate due to scattering from a single ionized impurity is

$$S(\mathbf{p},\mathbf{p}') = \frac{2\pi}{\hbar}\left(\frac{q^2}{\Omega\varepsilon_r\varepsilon_0}\right)^2 \frac{\delta(E(\mathbf{p}') - E(\mathbf{p}))}{\left[\beta^2 + 1/L_D^2\right]^2}\ . \tag{2.65}$$

Finally, we multiply by $N_D\Omega$, the number of impurities in the normalization volume, and make use of

equation (2.62) to write

$$\boxed{S(\mathbf{p},\mathbf{p}') = \frac{2\pi N_D q^4}{\hbar\Omega\varepsilon_r^2\varepsilon_0^2}\frac{\delta(E(\mathbf{p}')-E(\mathbf{p}))}{\left[4\left(\frac{p}{\hbar}\right)^2\sin^2\left(\frac{\alpha}{2}\right)+\frac{1}{L_D^2}\right]^2}}\,. \tag{2.66}$$

This result is general, but can be simplified in the case of a high carrier density. In that case, the Debye length is small enough to consider that the denominator is dominated by the $1/L_D^2$ term. As a consequence the transition rate for a strongly screened case is

$$S(\mathbf{p},\mathbf{p}') = \frac{2\pi N_D q^4 L_D^4}{\hbar\Omega\varepsilon_r^2\varepsilon_0^2}\delta(E(\mathbf{p}')-E(\mathbf{p}))\,. \tag{2.67}$$

As we saw in section 2.2.1, we can evaluate the scattering rate with the formula of equation (2.45)

$$\begin{aligned}\frac{1}{\tau(p)} &= \frac{\Omega}{8\pi^3\hbar^3}\int_0^{2\pi}\int_{-1}^{+1}\int_0^{\infty} S(\mathbf{p},\mathbf{p}')p'^2dp'd(\cos\theta)d\phi \\ &= \frac{N_D q^4}{2\pi\varepsilon_r^2\varepsilon_0^2\hbar^4}\int_{-1}^{+1}\int_0^{\infty}\frac{\delta(E(\mathbf{p}')-E(\mathbf{p}))}{\left[4\left(\frac{p}{\hbar}\right)^2\sin^2\left(\frac{\alpha}{2}\right)+\frac{1}{L_D^2}\right]^2}p'^2dp'd(\cos\theta)\,.\end{aligned} \tag{2.68}$$

If we orient the **z**-axis so that it points along the initial momentum, then $\alpha = \theta$ and equation (2.68) becomes

$$\frac{1}{\tau(p)} = \frac{N_D q^4}{2\pi\varepsilon_r^2\varepsilon_0^2\hbar^4}\int_0^{\infty}\int_{-1}^{+1}\frac{\delta(E(\mathbf{p}')-E(\mathbf{p}))d(\cos\theta)}{\left[4\left(\frac{p}{\hbar}\right)^2\frac{1-\cos\theta}{2}+\frac{1}{L_D^2}\right]^2}p'^2dp'\,. \tag{2.69}$$

We thus can integrate over $\cos\theta$ to find

$$\frac{1}{\tau(p)} = \frac{N_D q^4 L_D^2}{4\pi\varepsilon_r^2\varepsilon_0^2\hbar^2}\int_0^{\infty}\frac{1}{p^2}\frac{\gamma^2}{1+\gamma^2}\delta(E(\mathbf{p}')-E(\mathbf{p}))p'^2dp'\,, \tag{2.70}$$

where $\gamma^2 = 4\left(\frac{p}{\hbar}\right)^2 L_D^2 = 8m^*E(p)\frac{L_D^2}{\hbar^2}$. Knowing that $p' = \sqrt{2m^*E'}$ and $dp' = \frac{\sqrt{2m^*}}{2\sqrt{E'}}dE'$, we can transform the integral

$$\frac{1}{\tau(p)} = \frac{N_D q^4 L_D^2}{4\pi\varepsilon_r^2\varepsilon_0^2\hbar^2}\int_0^{\infty}\frac{\gamma^2}{1+\gamma^2}\frac{\delta(E(\mathbf{p}')-E(\mathbf{p}))\sqrt{2m^*}}{2\sqrt{E'}}dE'\,, \tag{2.71}$$

and finally integrate over E' to find

$$\boxed{\frac{1}{\tau(p)} = \frac{N_D q^4 L_D^2\sqrt{2m^*}}{8\pi\varepsilon_r^2\varepsilon_0^2\hbar^2\sqrt{E(p)}}\frac{\gamma^2}{1+\gamma^2}}\,. \tag{2.72}$$

Starting from equations (2.46) and (2.67) and using a similar demonstration, we can calculate the momentum relaxation rate, to obtain

$$\boxed{\frac{1}{\tau_m(p)} = \frac{N_D q^4}{16\pi\varepsilon_r^2\varepsilon_0^2\sqrt{2m^*}E^{3/2}(p)}\left[\ln(1+\gamma^2)-\frac{\gamma^2}{1+\gamma^2}\right]}\,. \tag{2.73}$$

These results will be used in section 2.4 to evaluate the scattering rates in the particular case of bulk GaN material, for which ionized impurities scattering is one of the most important for electronic transport.

Particular case of confined carriers

If we consider a 2D-channel of carriers, the above demonstration is not needed anymore. Indeed, the donors are placed outside the conduction channel and thus, it is possible to consider that the ionized impurities are too far from the electrons to interact with them.

2.2.3 Scattering with acoustic phonons

In case of deformation-potential interaction [Lundstrom 00], the squared matrix element used for acoustic scattering is given by

$$\boxed{\left|H_{\mathbf{p}'\mathbf{p}}\right|^2 = \beta^2 D_A^2 \left|A_\beta\right|^2 \delta_{\mathbf{p}',\mathbf{p}\pm\hbar\boldsymbol{\beta}}}, \tag{2.74}$$

where β is the wavevector, D_A the deformation acoustic potential, A_β is the deformation amplitude, and the δ function express the conservation of energy. This expression allows us to calculate the transition rate

$$\boxed{S(\mathbf{p},\mathbf{p}') = \frac{\pi m^* D_A^2}{\hbar\rho v_S p\Omega}\left(N_\beta + \frac{1}{2} \mp \frac{1}{2}\right)\delta\left(\pm\cos\theta + \frac{\hbar\beta}{2p} \mp \frac{\omega}{v(p)\beta}\right)}, \tag{2.75}$$

where ρ is the mass density, v_S the sound velocity, $v(p)$ the carriers velocity and ω the phonon angular frequency. The δ function express the conservation of both momentum and energy. From equation (2.75), we can calculate the scattering rates of electrons with acoustic phonons using the same line as for ionized impurities scattering.

$$\boxed{\frac{1}{\tau(p)} = \frac{1}{\tau_m(p)} = \frac{D_A^2 k_B T_L (2m^*)^{3/2}}{2\pi\hbar^4 c_l}\sqrt{E(p)}}, \tag{2.76}$$

where c_l is the elastic constant of the material, and T_L the lattice temperature.

Particular case of confined carriers

In the case of a quantum-well, the calculation of acoustic phonon scattering is different. In this work we will not detail the process, however, the details can be found in [Lundstrom 00]. Anyway, in the case of an infinite square well, the scattering rate becomes

$$\boxed{\frac{1}{\tau^{2D}(p)} = \frac{1}{\tau_m^{2D}(p)} = \frac{5 D_A^2 k_B T_L m^*}{2W\hbar^3 c_l}}, \tag{2.77}$$

where W is the width of the quantum-well. One should note that this rate does not depend anymore of carrier energy.

2.2.4 Scattering with polar optical phonons

The squared matrix element used for polar scattering from optical phonons is given by

$$\boxed{\left|H_{\mathbf{p}'\mathbf{p}}\right|^2 = \frac{\rho q^2\omega_0^2}{\beta^2\varepsilon_{r_0}\varepsilon_0}\left(\frac{\varepsilon_{r_0}}{\varepsilon_{r_\infty}} - 1\right)\left|A_\beta\right|^2 \delta_{\mathbf{p}',\mathbf{p}\pm\hbar\boldsymbol{\beta}}}, \tag{2.78}$$

where ω_0 is the polar optical phonon angular frequency, and ε_{r_0} and ε_{r_∞} are respectively the low and high frequency dielectric constant of the material. It is thus possible to calculate the transition rate due to

polar optical phonons scattering

$$\boxed{S(\mathbf{p},\mathbf{p}') = \frac{\pi m^* q^2 \omega_0}{\hbar \varepsilon_{r_0} \varepsilon_0 \beta^3 p \Omega} \left(\frac{\varepsilon_{r_0}}{\varepsilon_{r_\infty}} - 1\right) \left(N_\beta + \frac{1}{2} \mp \frac{1}{2}\right) \delta\left(\pm\cos\theta + \frac{\hbar\beta}{2p} \mp \frac{\omega}{v(p)\beta}\right)}, \tag{2.79}$$

where N_β is the Bose-Einstein factor, illustrating the number of phonons, and given by

$$N_\beta = \frac{1}{e^{\frac{\hbar\omega_0}{k_B T}} - 1}. \tag{2.80}$$

Finally, we calculate the energy relaxation rate from equation (2.47)

$$\boxed{\frac{1}{\tau_E(p)} = \frac{q^2\omega_0^2\left(\frac{\varepsilon_{r_0}}{\varepsilon_{r_\infty}} - 1\right)}{2\pi\varepsilon_{r_0}\varepsilon_0} \frac{(N_\beta + 1)\sqrt{\sinh^{-1}\left(\frac{E(p)}{\hbar\omega_0} - 1\right)}}{E(p)\sqrt{2E(p)/m^*}}}, \tag{2.81}$$

and the momentum relaxation rate

$$\begin{aligned}\frac{1}{\tau_m(p)} = \frac{q^2\omega_0\left(\frac{\varepsilon_{r_0}}{\varepsilon_{r_\infty}} - 1\right)}{4\pi\varepsilon_{r_0}\varepsilon_0\hbar\sqrt{2E(p)/m^*}} \Bigg[& N_\beta\sqrt{1 + \frac{\hbar\omega_0}{E(p)}} + (N_\beta + 1)\sqrt{1 - \frac{\hbar\omega_0}{E(p)}} \\ & - \frac{\hbar\omega_0 N_\beta}{E(p)}\sqrt{\sinh^{-1}\left(\frac{E(p)}{\hbar\omega_0}\right)} + \frac{\hbar\omega_0(N_\beta+1)}{E(p)}\sqrt{\sinh^{-1}\left(\frac{E(p)}{\hbar\omega_0} - 1\right)}\Bigg].\end{aligned} \tag{2.82}$$

Particular case of confined carriers

In the case of a hetero-layer, the expression of the scattering rate of electrons with polar optical phonons becomes [Shiktorov 07]:

$$\frac{1}{\tau(p)} = \frac{q^2\sqrt{2\hbar\omega_0 m^*}}{4\pi\hbar^2\varepsilon_{r_0}\varepsilon_0}\left(\frac{\varepsilon_{r_0}}{\varepsilon_{r_\infty}} - 1\right)\int_0^\pi \frac{512 + 72(\frac{3}{2}Qp_0d) + 3(\frac{3}{2}Qp_0d)^2}{(8 + (\frac{3}{2}Qp_0d))^3} d\alpha\,, \tag{2.83}$$

where $Q = |\hbar\boldsymbol{\beta}| = \sqrt{\frac{E(p)}{\hbar\omega_0} + \frac{E(p')}{\hbar\omega_0} - 2\sqrt{\frac{E(p)}{\hbar\omega_0}\frac{E(p')}{\hbar\omega_0}}\cos\alpha}$ is the normalized phonon wave vector between the initial $\mathbf{p}$ and final $\mathbf{p}'$ states for a scattering event, and d is the effective width of the hetero-layer, defined as:

$$d = \frac{16}{3}\sqrt[3]{\frac{8\varepsilon_{r_0}\varepsilon_0\hbar^2}{33m^*q^2}} \tag{2.84}$$

This formula is not directly solved, but numerically evaluated, as described in [Shiktorov 07].

2.2.5 Other interactions

The other scattering mechanisms described in the figure 2.3 won't be detailed in this thesis since the main scatterings involved in the electronic displacement within GaN based devices had been discussed [Shur 96]. Other mechanisms are weak or nonexistent and thus can be neglected in our study. The additional details can be found in [Lundstrom 00].

2.3 The optical phonon transit time resonance

In this section, we will describe the physical phenomenon responsible for amplification in the THz frequency domain, called optical phonon transit time resonance (OPTTR) and the conditions to gather for it to occur.

2.3.1 Origin of optical phonon transit time resonance

If we consider the scattering rate sketched in figure 2.5, one can see that it can be divided into two parts: the low energy region, called the *passive region* where the scattering rate is low and the *active region* where the scattering rate is very high. These two regions are separated by a sharp threshold.

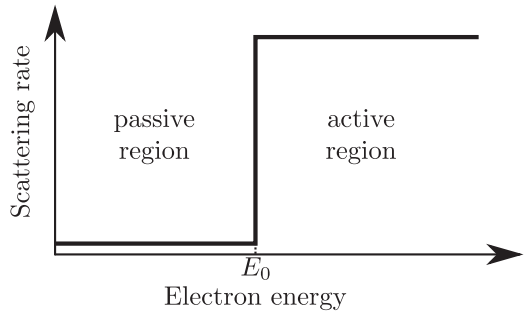

Figure 2.5: Perfect scattering rate as a function of electron energy needed for OPTTR.

As a consequence, an electron starting from the bottom of the band and accelerated by a constant external electric field will be able to cross the passive region without undergoing any collision and reach the active region where it will have a large probability to scatter and thus loose its energy. After this scattering the electron will be at the bottom of the conduction band where a new cycle will begin. This cyclic movement of acceleration followed by a loss of energy is responsible for various effects favorable for the sub-THz and THz radiation generation and amplification.

The first group of effects is related to the redistribution of carriers in the momentum space and to the formation of the steady-state distribution function which corresponds to overpopulation or inversion population of some areas in the momentum space or energy spectrum. The usual examples are:

1. an overpopulation of the negative mass cone in the heavy subband when Σ is parallel to [100] axis (the so called NEMAG proposed by Kromer in 1958 [Kromer 58]);
2. an opposite shift of cyclotron resonance (CR) spectra for positive and negative mass holes in Σ B [100] (the so called negative effective mass CR maser [Gavrilenko 91]);
3. an inversion population of direct optical transitions between the light – and heavy – hole-subbands in crossed Σ and B fields (the hot-hole intervalence band laser, see for example references [Gornik 91, Hubers 05] and references cited therein);
4. an overpopulation of Landau-levels in the light-hole subband (see, e.g., references [Gornik 91, Hubers 05]),
5. an overpopulation of impurity states (strained hot hole germanium resonant state THz laser [Hubers 05, Bondar 99, Odnoblyudov 00]) etc. Most of these lasers or masers are realized primarily on p-type germanium based on peculiarities of the valence band (warping of heavy-hole subband, presence of two subbands degenerated at the momentum space center, etc.) which are exploited by the static distribution function.

The second group of effects is based on dynamic properties of carriers caused by a cyclic character of single-carrier motion in the momentum space. In this case, the microwave power generation is caused by the dynamic negative differential mobility (DNDM) which appears in the frequency region corresponding to the period of the cyclic motion. An experimental verification of such a generation was obtained for the first time in InP samples by the group of Prof. L. E. Vorob'ev in St. Petersburg [Vorob'ev 01]. This previously described effect is the so-called OPTTR.

2.3.2 Description of optical phonon transit time resonance

Let us consider what we will call a *perfect material* with the scattering rates as a function of electron energy as described in figure 2.5. Let us stress that we put some contacts and apply a constant voltage across it, as sketched in figure 2.6, the electric field is then directly

$$\boldsymbol{\Sigma} = \frac{U_0}{L}\mathbf{u}\,, \tag{2.85}$$

where U_0 is the voltage, L the length of the device, and $\mathbf{u}$ the unit vector directed along the device. Available electrons will accelerate under the action of the electric field. This will lead to a quadratic gain

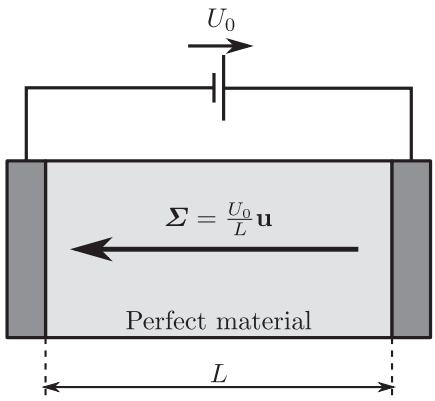

Figure 2.6: A constant electric field applied on a perfect material.

of energy according to the classical Newton's law

$$E(t) = \frac{q^2\Sigma^2 t^2}{2m^*}\,. \tag{2.86}$$

On one hand, this relation is true only in the case of ballistic transport of electrons in the material (i.e: if electrons do not scatter with anything), and thus will be usable as long as the electrons stay in the passive region of figure 2.5. On the other hand, supposing that electrons enter the active region, they will quickly scatter and loose their energy to go back to the bottom of the band, where they will start a new cycle of acceleration following equation (2.86). As a consequence all electrons energies describe a cyclic movement inside the material from a contact to the other as drawn in figure 2.7. This cyclic movement is the basis of the amplification process that can occur in the material.

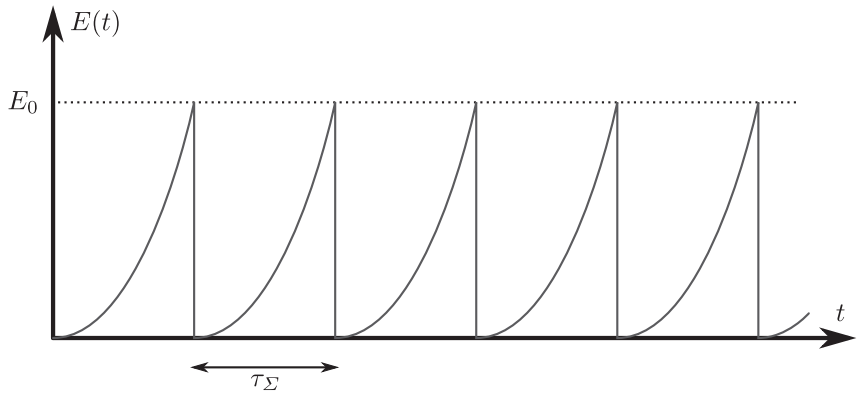

Figure 2.7: Illustration of the cyclic energy of electrons moving in a perfect material under a constant electric field, induced by a strong scattering rate at E_0.

2.3.3 Conditions for optical phonon transit time resonance

To allow the occurrence of OPTTR mechanism in a device, the main condition to achieve is a scattering rate profile as close as possible as the one shown in figure 2.5. Such a situation can usually appear in materials presenting high scattering rates with polar optical phonon emission, that only occurs from a non-zero value of energy. In the passive region, where the carrier energy $E(p)$ is less than that of the optical phonon $\hbar\omega_0$, optical phonon emission is absent and only weak elastic scatterings caused by deformation and piezoelectric acoustic phonons as well as impurity ions are possible. The intensity of the momentum relaxation in this region is conveniently characterized by an average momentum relaxation rate $\nu_- = \nu_{imp} + \nu_{da} + \nu_{piezo}$ [1] or by the corresponding average momentum relaxation time $\tau_- = 1/\nu_-$. For the ballistic motion under the action of dc electric field Σ to be realized in the passive region, the relaxation time must satisfy the condition:

$$\tau_\Sigma \ll \tau_- \tag{2.87}$$

where $\tau_\Sigma = p_0/q\Sigma$ is the transit time necessary for an electron started from the passive area center to reach its boundary at $p_0 = \sqrt{2m^*\hbar\omega_0}$. Here p_0 is the radius of the optical phonon sphere in the momentum space, $\hbar\omega_0$ the optical phonon energy, m^* the electron effective mass, and a simple spherical and parabolic band is assumed.

Entering into the active region $E(p) > \hbar\omega_0$ where the spontaneous emission of optical phonons is possible, a carrier emits an optical phonon and returns back into the passive region. If the penetration into the active region is sufficiently small,

$$\delta E \ll \hbar\omega_0 \tag{2.88}$$

a carrier quickly emits an optical phonon and comes back near the passive region center. If the condition given by equation (2.88) is fulfilled all the carriers move practically along $\mathbf{p}||\boldsymbol{\Sigma}$ axis from $p \approx 0$ up to $p \geq p_0$ periodically repeating this motion with the frequency $\nu_\Sigma = 1/\tau_\Sigma$, as sketched in figure 2.7. In terms of the characteristic times this condition is usually formulated as:

$$\tau_+ \ll \tau_\Sigma \tag{2.89}$$

1. The subscripts *imp*, *da*, and *piezo* respectively stands for impurities, deformation acoustic and piezoelectric scatterings.

where τ_+ is the characteristic time of the optical phonon emission in the active region. Let us stress, that due to different character of scattering process below and above $\hbar\omega_0$, τ_- describes the momentum relaxation in the passive region, while τ_+ is determined by the scattering rate from the active region back to the passive one. When the conditions (2.87) and (2.89) are satisfied, a carrier in the momentum space takes the well known cyclic motion characterized by τ_Σ. The smaller is the penetration into the active region the closer the carrier moves to the cyclic trajectory.

These conditions can be rewritten in terms of lower-and upper-limits for the amplitude of the effective electric field as:

$$\Sigma_- \ll \Sigma \ll \Sigma_+ \tag{2.90}$$

where $\Sigma_- = p_0/q\tau_-$ and $\Sigma_+ = p_0/q\tau_+$. Magnitudes of Σ_- and Σ_+ can be determined through the parameters of scattering mechanisms in the passive and active regions which characterize the semiconductor material and the type of electron dynamics (2D or 3D). As we will see in the next sections, wide-band-gap materials such as III-N compounds (nitrides) satisfy these requirements.

For a deeper understanding of frequency limitations of OPTTR, one can look at pictures sketched in figure 2.8. As the scattering rate increases in the passive zone, the electrons undergo more and more collisions before being able to reach the scattering threshold (figure 2.8(a)). Furthermore, as illustrated in figure 2.8(b), if the scattering rate in the active region is not sufficient, the electrons will be able to deeply penetrate in the active zone and undergo their collision far from the threshold. Both of these effects leads to the deterioration of the OPTTR mechanism in the material, and in the worst cases will completely destroy it.

2.3.4 Amplification by optical phonon transit time resonance

To link OPTTR with an amplification, we propose a small-signal study. The general objective of the small-signal analysis is to determine the amplification coefficient (static gain) for electromagnetic waves propagating inside an active media and to investigate its dependence on frequency ν, magnitudes of applied fields Σ_0, lattice temperature T_L, doping level N_D, etc. In the region where the differential mobility, $\mu(\nu)$ is negative, the gain $\alpha_0(\nu, n)$ is directly proportional to the real part of μ, $\Re[\mu]$, as:

$$\alpha_0(\nu, n) = -\Re[\mu(\nu)]n\frac{q}{c\varepsilon_0\sqrt{\varepsilon_r}}\,, \tag{2.91}$$

where c is the light velocity in vacuum. As a consequence of equation (2.91), the main problem of the small-signal analysis reduces to calculate the differential mobility spectrum under various conditions.

To calculate the differential mobility spectrum and the static gain in bulk wurtzite GaN subjected to a constant electric field Σ_0, we have used the single-particle Monte-Carlo procedure based on transient velocity averaging over before- and after-scattering ensembles as described in [Pozhela 92]. The advantage of this procedure is that, for a given Σ_0, N_D, and T_L, it allows one to obtain the whole amplification/absorption spectrum in a single Monte-Carlo simulation. The parameters of the band model are taken from [Albrecht 98]. Because the difference between the parallel and transverse effective mass in wurtzite GaN is small, a spherically symmetric conduction band approximation is used. Electron scatterings by polar optical phonons, deformation acoustic phonons and ionized impurities are accounted for. Due to relatively high heating of carriers up to energies of about $100 \sim 150$ meV the deformation acoustic scattering is considered in elastic approximation.

To show the advantages of GaN in comparison with other materials for the realization of an OPTTR maser, figure 2.9 presents the scattering rates for optical phonon emission as a function of the electron

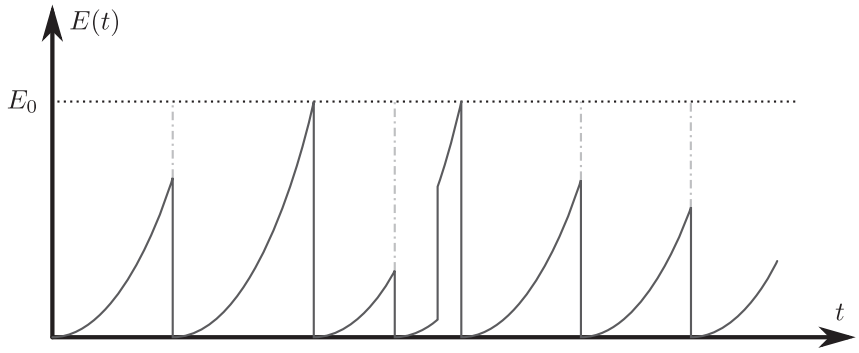

(a) Non-zero scattering rate in the passive zone

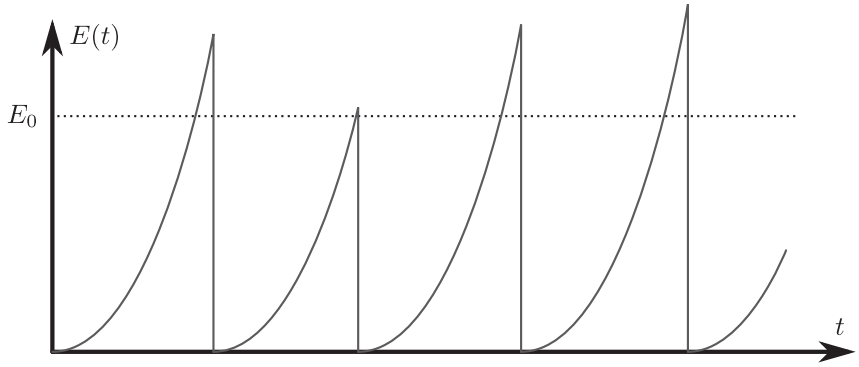

(b) Non-infinite scattering rate in the active zone

Figure 2.8: Illustration of the deterioration of the cyclic movement of electrons occurring in the material due to non-perfect properties of the material.

energy for wurtzite GaN, zincblende GaN, InN, GaAs, InP, CdTe, and 4H–SiC. From the arguments given in section 2.3.3, it is evident that the conditions for the streaming motion and the coherence of successive free flights of single carriers are definitively superior in GaN than in other materials when considering the combination of both the high value of the optical phonon energy and the steep increase of the optical phonon emission rate.

As an example of Monte-Carlo calculations, figure 2.10 shows the differential mobility spectra for two samples of wurtzite GaN with doping levels of $N_D = 10^{15}$ and 10^{16} cm^{-3} (curves 1 and 2, respectively) calculated at $T_L = 10$ K and $\Sigma_0 = 4.3$ kV/cm. This value of the electric field is sufficiently high for the runaway from the low-energy impurity scattering to take place for both doping levels. Accordingly, the spectra differ in the low-frequency region only, and practically coincide in the THz frequency range. The OPTTR manifests itself in the differential mobility spectrum as a sequence of minima corresponding to the first and higher harmonics of the resonant frequency $\nu_\Sigma = 1/\tau_\Sigma$. However, the broadening of the minima increases significantly with higher harmonics. Therefore, in the present case only the first two minima can be resolved while dynamic negative differential mobility (DNDM) is achieved in the first minimum only.

For a wurtzite GaN sample with $N_D = 10^{16}$ cm^{-3}, figure 2.11 reports as a function of the field the maximum negative value of $\Re[\mu]$ (curves 1 and 2 in the lower part of the figure for $T_L = 10$ and 80 K,

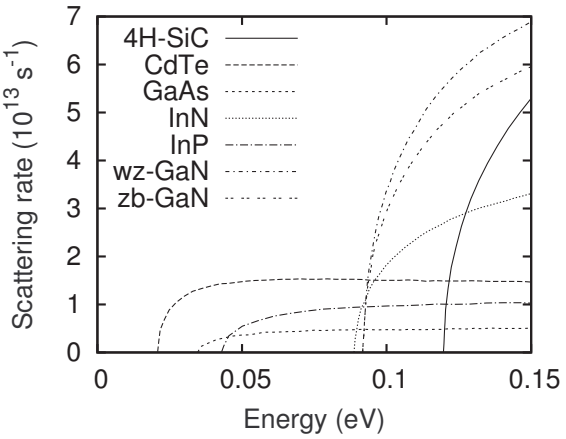

Figure 2.9: Scattering rates due to polar optical phonon emission in zincblende GaN, wurtzite GaN, InP, InN, GaAs, CdTe and 4H-SiC.

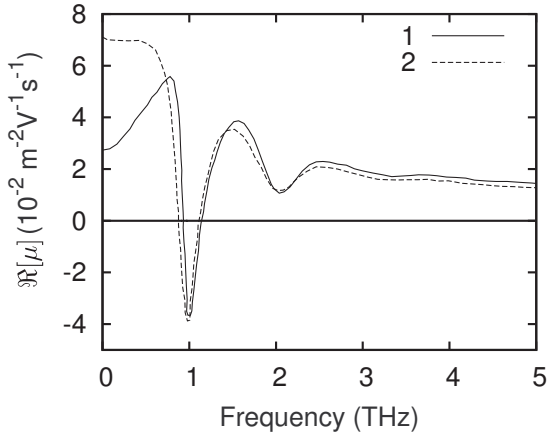

Figure 2.10: Real part of differential mobility spectrum calculated for wurtzite GaN at $T_L = 10$ K, $\Sigma_0 = 4.3$ kV/cm for the doping levels of $N_D = 10^{15}$ and 10^{16} cm^{-3} (curves 1 and 2 respectively).

respectively) and the lower and upper limits of the amplification range for the first case (curves 3 and 4 in the upper part of the figure). In the region of DNDM, the amplification band for $T_L = 80$ K practically coincides with that for $T_L = 10$ K. For the lower temperature of 10 K the negative values of $\Re[\mu(\nu)]$ appear at $\Sigma_0 \approx 1$ kV/cm and quickly reach the maximum values of the DNDM at $\Sigma_0 \approx 1.8$ kV/cm. The appearance and rapid change of the DNDM is related to electron runaway from the low-energy impurity scattering and subsequent formation of a narrow streaming-like distribution in momentum space. With a further increase of Σ_0, the maximum value of the DNDM decreases approximately as $1/\Sigma_0$ and finally disappears at $\Sigma_0 \approx 12$ kV/cm. Indeed, at $\Sigma_0 > 12$ kV/cm a significant penetration of carriers into the momentum space outside the optical phonon sphere (the so called active area) takes place, and the coherence of successive free flights of single carriers is destroyed.

As follows from figure 2.11, the generation frequency can be easily tuned by the static electric field magnitude. The total band of amplification caused by the OPTTR is rather wide, and at 10 K, covers practically the whole submillimeter region starting at $\nu = 0.2$ THz and ending at $\nu = 3$ THz. For a given value of Σ_0, the amplification band is very narrow (see curves 3 and 4), and the optimum amplification frequency, corresponding to the maximum value of the DNDM in the band, increases practically linearly with Σ_0 in full agreement with that predicted by the simple relation $\nu_\Sigma = q\Sigma_0/p_0$. With the increase of T_L, both the narrow character of the amplification band at a fixed Σ_0 and the linear increase of the optimum frequency of amplification remain the same. However, the total frequency range of possible amplification narrows down because the electric field range corresponding to streaming conditions also narrows down with the increase of scattering intensity in the passive region. Moreover, the maximum values of the DNDM decreases with the increase of T_L, the amplification in the THz frequency range persisting for liquid nitrogen temperatures. From one side, this persistence is very important for the technical implementation of the effect, since liquid nitrogen temperatures are preferable for practical use. From another side, the wide range of lattice temperatures where the DNDM is observed is of help to realize more stable generations at liquid helium temperatures, since any sample warms up under generation in strong applied fields.

The study of the dependence of the amplification coefficient (gain) on the doping level is of special interest since in accordance with equation (2.91), the gain at a given frequency is proportional to the product of DNDM with carrier concentration. It means that the higher the doping concentration the

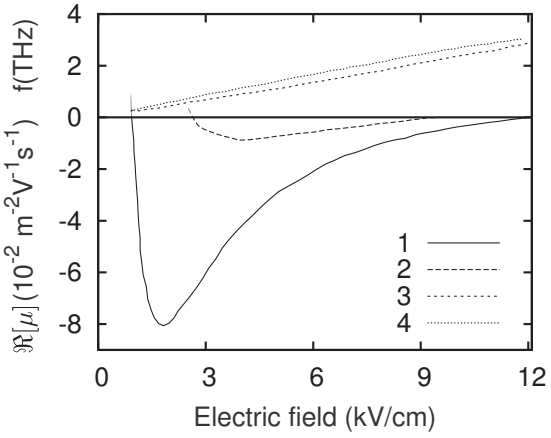

Figure 2.11: Maximum value of the DNDM (curve 1) and lower and upper frequency limits of the amplification band (curves 3 and 4, respectively) calculated for wurtzite GaN as a function of the electric field Σ_0 at $T_L = 10$ K with $N_D = 10^{16}$ cm^{-3}. Curve 2 refers to the maximum value of the DNDM at $T_L = 80$ K for $N_D = 10^{16}$ cm^{-3}.

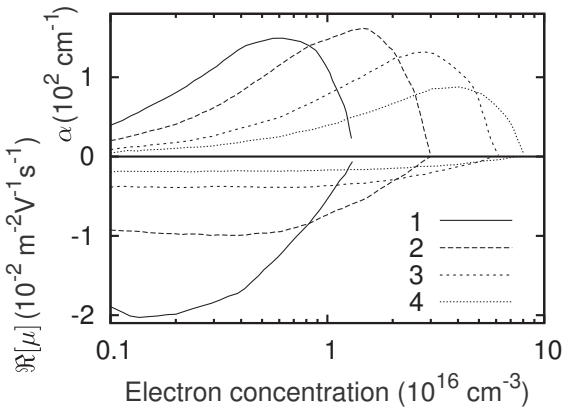

Figure 2.12: Real part of the differential mobility (lower curves) and dynamical gain (upper curves) as a function of electron concentration in wurtzite GaN at $\nu = 0.25$, 0.5, 1, and 1.5 THz for $T_L = 10$ K (curves 1 to 4).

higher the gain. However, the increase in doping concentration decreases the DNDM value due to the increase in impurity scattering, which leads eventually to the disappearance of DNDM. The competition of these two opposite processes implies that there exists a certain optimum range of doping level when the gain is maximum. This is illustrated in figure 2.12, which presents the gain and the DNDM maximum value (upper and lower parts of the figure) as a function of the carrier concentration at four fixed frequencies of $\nu = 0.25$, 0.5, 1, and 1.5 THz (curves 1 to 4) at $T_L = 10$ K. As follows from figure 2.12, the possible maximum gain is of the same order, $\alpha = 100 \sim 150$ cm^{-1} in a wide frequency range. However, the optimum doping level strongly depends on the desired frequency and differs for about one order of magnitude in going from the left to the right edge of the amplification band.

2.4 Scattering rates and amplification bands in gallium nitride

In the previous section, we described how the OPTTR mechanism can exist in a material to amplify an incident electromagnetic wave and what are the optimum conditions to obtain the largest amplification band. In that section, we will see why GaN (both bulk and quantum-wells) is a good candidate for amplification in the THz frequency domain, starting by drawing its scattering rates as a function of electron energy.

2.4.1 Bulk material

The physical properties of bulk GaN needed to calculate the momentum relaxation rates are summarized in table 2.1. We can now draw the scattering curves for each paramount scattering mechanism thanks to equations (2.73), (2.76) and (2.82). The result is shown in figure 2.13, for a carrier concentration of 10^{16} cm^{-1} at 10 K temperature. Comparing to figure 2.5, these scattering rates seem to be good, except for low energy electrons for which interactions with ionized impurities play a major role in their displacement. This may be a problem for OPTTR-induced amplification as we may move closer to the case of figure 2.8(a).

Table 2.1: Physical parameters of wurtzite GaN.

Symbol	Magnitude	Value	Unit
ε_{r_0}	Static dielectric constant [Bougrov 01]	8.9	
ε_{r_∞}	High frequency dielectric constant [Bougrov 01]	5.35	
$\hbar\omega_0$	Polar optical phonon energy [Bougrov 01]	91.2	meV
D_A	Acoustic deformation potential [Arabshahi 09]	8.3	eV
c_l	Elastic constant [Polian 96]	145	GPa

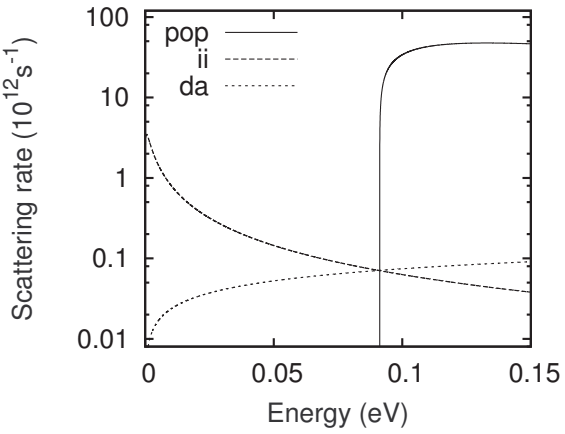

Figure 2.13: Main scattering rates in wurtzite GaN at 10 K temperature. (pop), (ii), and (da) respectively stand for polar optical phonon, ionized impurities, and deformation acoustic scatterings.

Let us see how these scattering rates can be altered with the variation of some parameters that can be controlled during the fabrication process as well as in the experimental conditions.

Evolution with temperature

If the temperature increases, the scattering rate of electrons with acoustic phonon becomes more and more important, as it could have been predicted from equation (2.76). The comparison of scattering rates for three different temperatures from 10 up to 300 K is pictured in figure 2.14.

Even if the polar optical phonon scattering is also temperature dependent (from the N_β factor of equation (2.82)), figure 2.15 shows that the behavior of this scattering rate is not really affected by temperature variation from 10 K to room temperature.

As a conclusion on the temperature effect, the lower the temperature, the closer we will be to the situation of figure 2.5 regarding the scattering rates of acoustic phonons.

Evolution with carrier concentration

As predicted from equation (2.73), if the concentration of carriers is increased (and also that of ionized impurities), the scattering rates of electrons with ionized impurities will also increase. This result is shown in figure 2.16, illustrating the evolution of the scattering rates with ionized impurities for concentrations from 10^{15} up to 10^{17}.

The carrier concentration is consequently an important factor to take into account for bulk materials. A compromise will have to be considered between gain of the device (which may increase with the carrier concentration) and band of amplification (which will be reduced by an increase of the total carrier

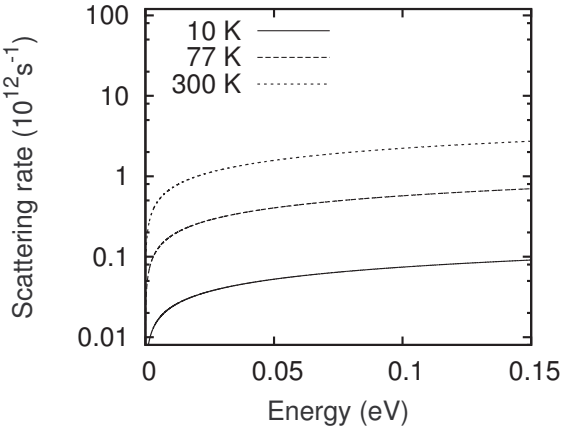

Figure 2.14: Evolution of deformation acoustic scatterings as a function of energy for three different temperatures (from 10 up to 300 K) in wurtzite GaN.

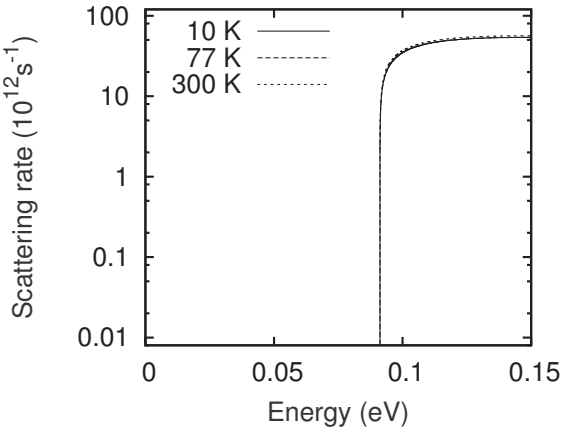

Figure 2.15: Evolution of polar optical phonon scatterings as a function of energy for three different temperatures (from 10 up to 300 K) in wurtzite GaN.

concentration).

Induced amplification band

The Monte-Carlo simulations performed in [Starikov 08, Starikov 01] show that the amplification band for bulk GaN at a temperature of 10 K with a carrier concentration of 10^{16} cm^{-3} is from 0.2 up to 3 THz, as represented in figure 2.17.

This frequency band is very interesting for the THz amplification because it covers almost the full THz-domain. A problem is still present since the fabrication of sufficiently good quality bulk GaN devices is a challenging task [Avrutin 10]. Hopefully, the fabrication process of GaN quantum-well is now much better controlled [Natali 09] and we thus can consider the case of confined carriers for THz amplification in the next sub-section.

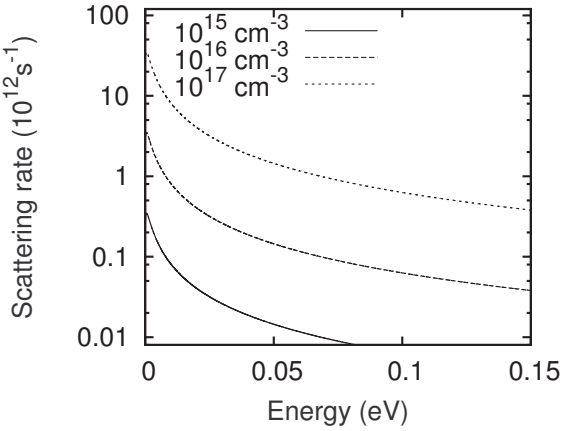

Figure 2.16: Evolution of ionized impurities scatterings as a function of energy for three different doping concentration (from 10^{15} up to 10^{17} cm^{-3}) in wurtzite GaN.

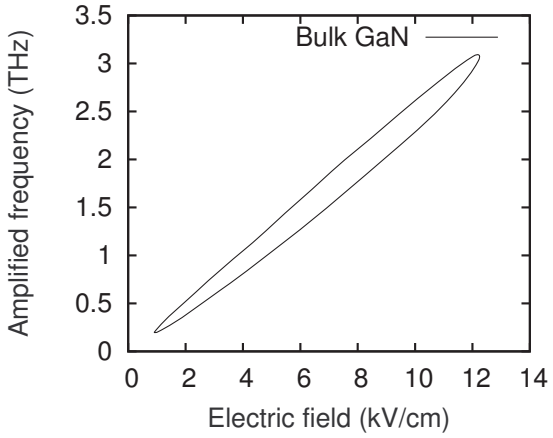

Figure 2.17: Amplification band as a function of applied electric field for bulk wurtzite GaN at a temperature of 10 K with a carrier concentration of 10^{16} cm^{-3} [Starikov 08].

2.4.2 2-D material

From equation (2.77), we can draw the momentum relaxation rate for acoustic phonons in a quantum-well structure, and also Monte-Carlo simulations of reference [Shiktorov 07] give us the momentum relaxation rate of polar optical phonons under the same conditions. Figure 2.18 illustrates these paramount scatterings in a 5 nm thick quantum-well of GaN at a temperature of 10 K.

Compared to the scattering rates in bulk GaN at the same temperature (figure 2.13), one can note that the threshold of the optical phonon scattering is sharper in the case of a quantum well (figure 2.18). This will lead to a higher upper frequency limit of the amplification band since the electrons have less chance to deeply penetrate into the active region for the same value of the electric field. As far as the passive zone is concerned, the absence of ionized impurity scattering [2] is a clear advantage for low energies. Only drawback is a slightly greater acoustic phonon scattering in the 2-D case. This will slightly increase the lower limit for frequency amplification.

2. Recall that doping impurities are placed outside the conductive channel, hence, the scattering of electrons with ionized impurities is negligible.

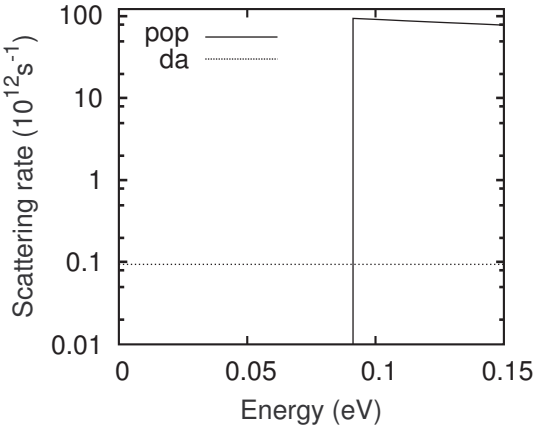

Figure 2.18: Main scattering rates in a 5 nm wurtzite GaN quantum well at a temperature of 10 K. (pop), and (da) respectively stands for polar optical phonon, and deformation acoustic scatterings.

Evolution with temperature

If the temperature increases, the scattering rate of electrons with acoustic phonon becomes more important, as predicted from equation (2.77). The comparison of scattering rates for three different temperatures from 10 up to 300 K is pictured in figure 2.19.

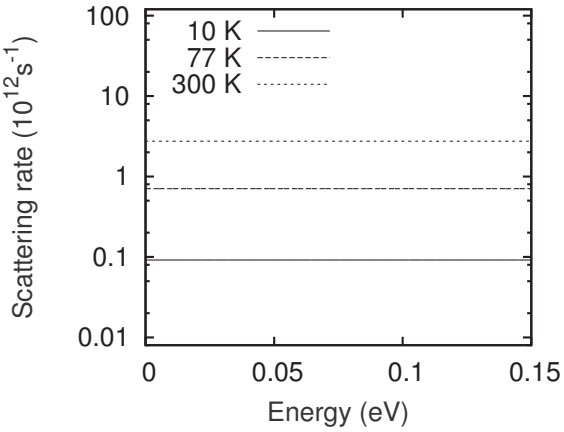

Figure 2.19: Evolution of scatterings with deformation acoustic phonons as a function of energy for three different temperatures (from 10 up to 300 K) in wurtzite GaN quantum-well.

In the case of quantum-well structure, the same conclusion as that of bulk materials can be drawn. The higher the temperature, the more important the scattering rates in the passive zone will be. This results in an increasing of the lower amplification frequency limit, and by consequence, in a shortening of the total amplification band.

Induced amplification band

The Monte-Carlo simulations performed in [Starikov 08,Starikov 01] show that the amplification band for a 5 nm thick quantum well of GaN at a temperature of 10 K is approximately from 0.2 up to 7.5 THz, as represented in figure 2.20.

The thin layer version of GaN is thus even more interesting than the bulk one, where the amplification occurs in a wider band.

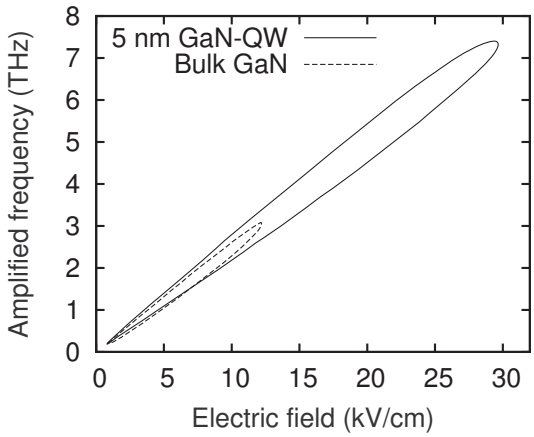

Figure 2.20: Amplification band as a function of applied electric field for bulk wurtzite GaN at a temperature of 10 K with a carrier concentration of 10^{16} cm^{-3} [Starikov 08], compared to the curve of figure 2.17 relative to bulk GaN at the same operating temperature.

2.4.3 Comparison of GaN with other materials

GaN is not the only material to present scattering rates close to those of figure 2.5, indium phosphide (InP) as well as other nitride based materials (aluminum and indium nitrides – AlN, InN) are also good candidates for amplification with OPTTR. They only differ by their amplification bands, related to their physical properties. The details of the Monte-Carlo simulations performed for these materials can be found in [Starikov 08] and the results are summarized in figure 2.21.

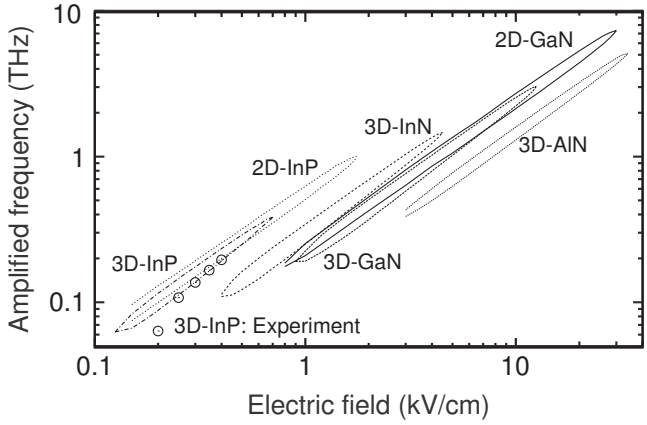

Figure 2.21: Comparison of the amplification bands due to OPTTR for different bulk materials and quantum-wells as a function of applied electric field [Starikov 08]. The reported points are the only available experimental results performed with bulk InP in [Vorob'ev 01].

In particular, this figure shows the only experimental points available at present of OPTTR induced amplification which were reported in [Vorob'ev 01]. This experiment have been done with bulk InP and shows a very good agreement with the Monte-Carlo simulations of [Starikov 08]. This result is particularly promising for a practical realization of amplification in the terahertz frequency domain by replacing the InP sample by a GaN sample.

2.5 Device design and experimental conditions

From what have been detailed in the beginning of this chapter, we can extract some useful information about the way we have to build our devices and the experimental conditions.

2.5.1 Electric field versus device length

The design of our device has to consider two parameters; from one side, figure 2.20 informs us about the electric field to apply to achieve the required amplification, but on the other side, we also have to be careful of the device length which has to be set in accordance to the wavelength of the incident THz beam.

For example, if we try to measure amplification in the 0.2–1.7 THz range, we have to apply an electric field between 0.8 and 4 kV/cm. If we want to apply reasonable voltages on the device (let say $\leq$ 20 V), that gives us the maximum length (i.e. the maximum distance between the contacts) by the formula

$$L_{d_{max}} = \frac{U_{max}}{\Sigma_{max}} = 50 \text{ µm} . \tag{2.92}$$

In the same time, for the lowest frequency, the wavelength is equal to

$$\lambda_{max} = \frac{c}{\nu_{min}} = 1.5 \text{ mm} . \tag{2.93}$$

This difference of $L_{d_{max}}$ and λ_{max} may be a problem for the coupling of the incident beam with the device itself. As a consequence, we have to find a way to increase the active surface while keeping reasonable applied voltages. The solution that we have imagined is in the use of interdigitated fingers as a pattern of contacts. As illustrated in figure 2.22, these types of contacts allow to keep a small distance between two consecutive contacts while increasing the total surface.

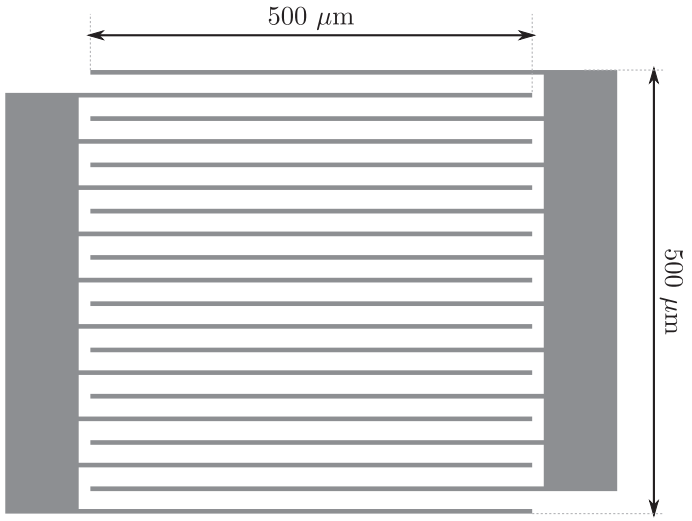

Figure 2.22: Illustration of a pattern of the interdigitated fingers.

At this point, we will confront each other with the technologist people, because they are not able to build endless fingers and are limited by the fabrication process. After a small discussion with our

fabrication laboratory [3], they are able to build fingers of 1 µm width over a maximum total length of 500 µm. We thus finally decided that the samples will be 500×500 µm^2 of total surface.

One drawback of such a pattern is illustrated in figure 2.23; two consecutive zones between fingers present electric field in opposite directions. At present it is not completely clear if this situations may be favorable or not to obtain the final amplification. Indeed, in these zones, electrons go in opposite directions which may affect the amplification mechanism of the global device.

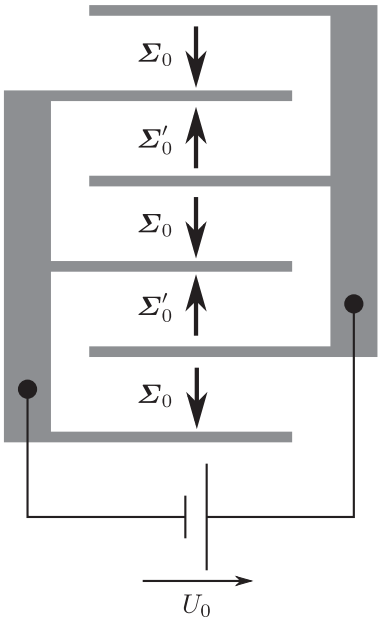

Figure 2.23: Simplified scheme of interdigitated fingers and associated electric fields $\boldsymbol{\Sigma}_0$ and $\boldsymbol{\Sigma}_0'$ under constant biasing.

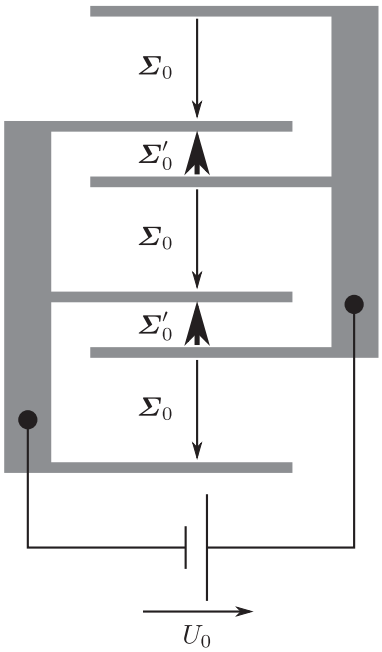

Figure 2.24: Simplified scheme of asymmetrical interdigitated fingers and associated electric fields $\boldsymbol{\Sigma}_0$ and $\boldsymbol{\Sigma}_0'$ under constant biasing.

In order to investigate different situations corresponding to different electric fields we decided to create a set of devices where the two zones of opposite field directions have different lengths, as described in figure 2.24. This leads to different values of electric fields in the two regions: one with a low value of electric field, and the other with a high value of electric field. To obtain the maximum surface for amplification, one possibility is to choose the biggest zone as the *active zone* [4], where the electric field is calculated at the right value for the amplification. The *passive zone* is characterized by a very high electric field value (because this zone is shorter) which may be out of the amplification band sketched in figure 2.20.

The fabrication mask with all the devices built on the same pattern is represented on figure 2.25.

In a second time, the passive zones will be etched during the fabrication process to clearly remove any residual current in these areas.

3. Y. Cordier and M. Chmielowska from the CRHEA – Research center on Hetero-Epitaxy and its Applications, Sophia Antipolis, Valbonne.

4. In this context, *passive* and *active* zones represents the areas of the devices where the electric field is calculated to obtain amplification or not. Not to be confused with the regions of figure 2.5.

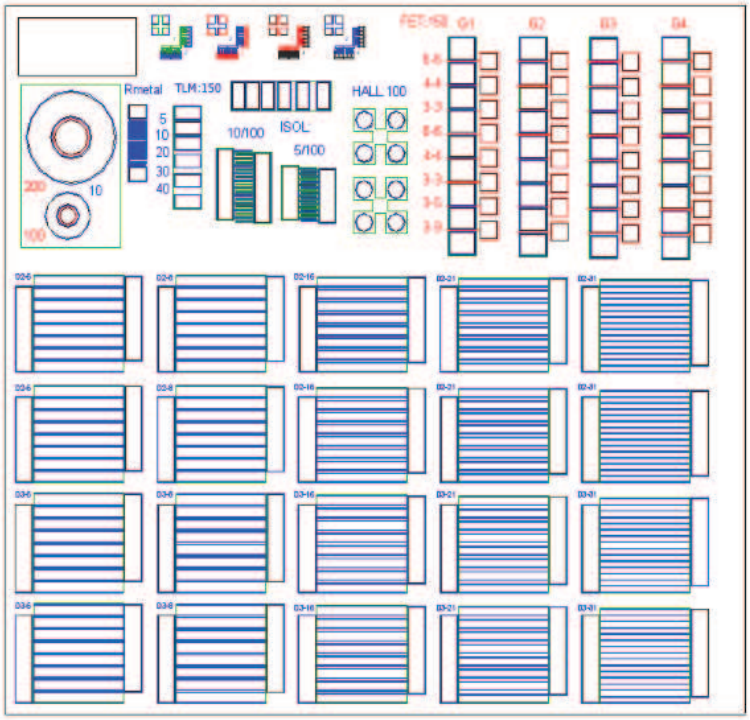

Figure 2.25: Design of the mask of our samples which will be investigated in the following experiments.

2.5.2 Operating temperature

As we saw in section 2.4.2, the operating temperature is an important factor to take into account for successful experiments. Results of simulations can be summarized in a simple sentence: *the coolest is the better*. According to discussions with the experts of the performed Monte-Carlo simulations in [Starikov 08], even if the amplification band is restricted with temperature, it should be operational up to 100 K. As a consequence, the fabricated samples will have to be cooled below this temperature during the experiments.

2.6 Summary

This key chapter is at the basis of the understanding of how the GaN-based devices can be considered as amplificating components in the THz frequency domain. The way to evaluate electron interactions in theses devices has been introduced and applied to the interesting case of GaN. Moreover, the link between these interaction rates and the amplification effect were described. Finally, some experimental restrictions have been extracted from these results to optimize the following investigations.

Part II

Experimental realization

Chapter 3

GaN quantum-wells: towards concrete devices



In this chapter, we will briefly introduce the fabrication process of the samples used for our experiments. First, we will show how the pre-processing of the devices is made; from the needs of the future samples, we design the layers scheme, and the contacts pattern. In a second time the vertical band diagram is simulated to extract the electrons concentration expected in the conduction channel. Then the processing mask is designed for fabrication. A description of the fabrication process from the substrates to the contacts is introduced. Finally, the classical characterizations of the fabricated samples are performed.
The samples are synthesized within the collaboration team of Yvon CORDIER, Magdalena CHMIELOWSKA, and Sébastien CHENOT, from the CRHEA [1].

3.1 Pre-process conception

As it has been discussed in chapter 2, some fabrication requirements are needed to optimize the chances of success of THz amplification in the following experiments. The first is the fact that we need a two-dimensional electron gas channel of the purest possible quality to avoid any parasitic transport problems such as dislocations occuring in the channel. The second is the device surface which have to be as large as possible with interdigitated fingers contacts to match the wavelength of the THz incident beam.

3.1.1 Different layers

The vertical structure of our samples is sketched in figure 3.1. It is an ungated HEMT structure [Cordier 07]. Starting from a 330 µm thick sapphire substrate, a 3 µm thick template of GaN-Fe is grown. On one hand, this first layer, called *template*, is used to compensate the big difference (16 %) of lattice constant between sapphire (2.75 Å) and GaN (3.19 Å) which generates some dislocations in the structure (from $\approx 10^10$ cm^2 at the beginning of the layer to $\approx 10^8$ cm^2 at the top surface of the template) and on the other hand it allows to counterbalance the doping impurities (such as oxygen) introduced during the process by using iron as a deep acceptor. This results in a insulated buffer layer.

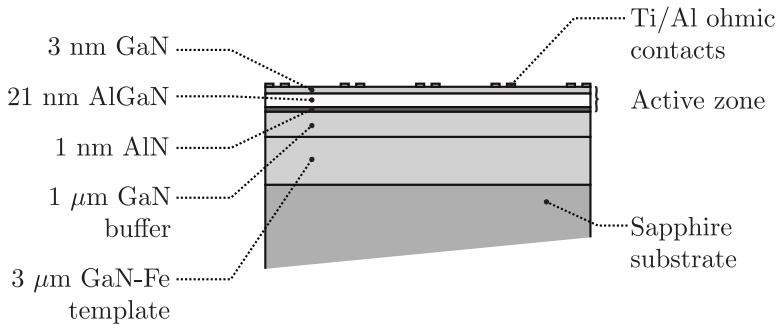

Figure 3.1: Different layers grown on sapphire substrate to build the GaN quantum-well.

The second layer, the *buffer*, will finish to compensate the remainder lattice constant rift with sapphire and create the conduction channel at its top frontier with the next layer. It is a kind of extension of the template. The next layer, made-up of a different material (AlN) will constitute the heterojunction with the buffer to create the electron trap, also known as the channel. This layer is called the *spacer* and is

1. Research Center on Hetero-Epitaxy and its Applications, Sophia Antipolis, France

also used to separate the channel from the next AlGaN layer, reducing electron alloy scattering. In other words, the confinement of electrons in the channel is better and they undergo less alloy scattering. One should note that there is also a lattice constant rift between this layer and the previous one. Although, the lattice constants of AlN (3.11 Å) and GaN (3.19 Å) have a difference of 2.4 %, but the thickness of the AlN layer is sufficiently small to tolerate the mismatch. The next layer, made-up of $Al_{0.29}Ga_{0.71}N$ is the *barrier* and is non intentionally doped. It is used for confining the electrons in the GaN channel. Finally, the last GaN *cap layer* is built to prevent the oxidation of the bottom structure from the aluminum contained in the contacts. The latter are made of a stack of Ti/Al/Ni/Au to create ohmic contacts. Their shape will be discussed in section 3.1.3

3.1.2 Band diagram

The energy band diagram of the structure sketched in figure 3.1 has been calculated by solving the Poisson-Schrödinger equation. The results are shown in figures 3.2 and 3.3 for 10 and 300 K temperatures. In particular, figure 3.2 shows both conduction and valence bands while figure 3.3 shows the conduction band and the first three energy levels of the quantum well at the frontier between AlN and GaN. It turned out that the conduction channel is not strongly affected by the variation of temperature. The simulation

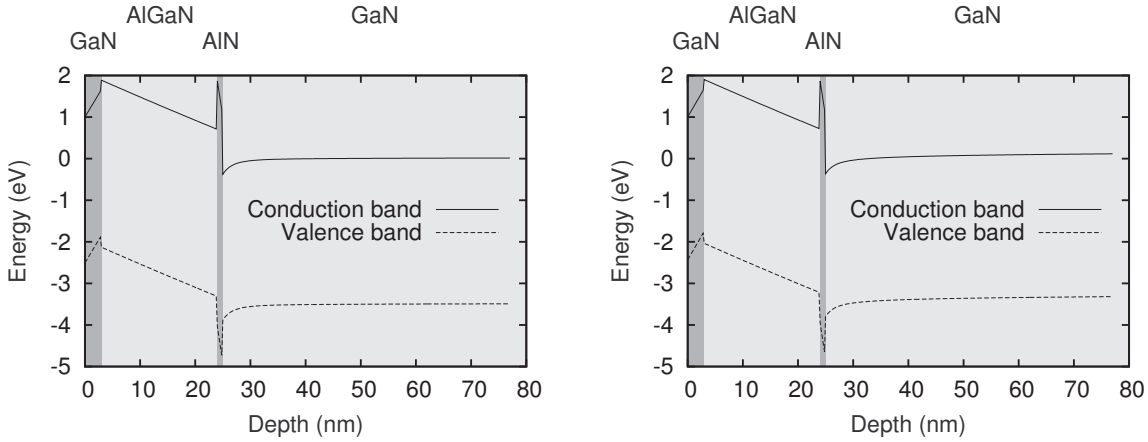

(a) 10 K (b) 300 K

Figure 3.2: Vertical valence and conduction bands diagram resulting from the structure of figure 3.1 for temperatures of 10 K (a) and 300 K (b). The 0 axis in energy corresponds to the Fermi level of the structure.

also informs about the population of the carriers in the device, which is expected to get 1.15×10^{13} cm^{-2} of electrons concentration at both 10 and 300 K. This concentration is at 99.5 % located in the GaN channel and mainly split among the first three energy levels as reported in tables 3.1 and 3.2 which respectively stands for 10 and 300 K. The gap between the two first levels of the quantum well is very important. It has to be greater than the optical phonon energy of the conductive material. Indeed, electrons have to scatter with optical phonons before reaching the energy needed to change of energy level, which might cause a change in the momentum of the electrons and on the period between to scatterings with optical phonons. Moreover, the maximum part of electrons population should be located within the first energy level. In our case, it turned out that the gap between the first and second energy levels is of 96.4 and 104.8 meV for 10 and 300 K respectively. For both temperatures, this value is greater than the optical

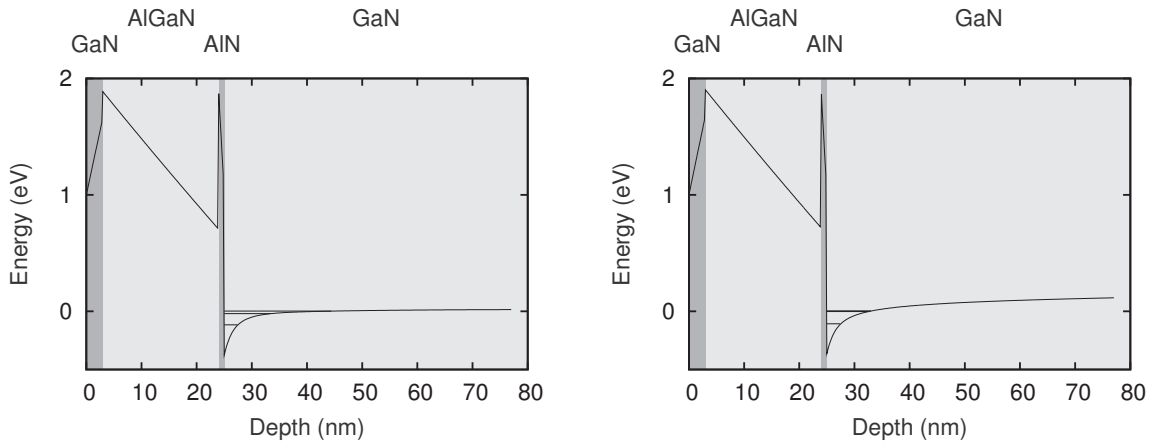

(a) 10 K (b) 300 K

Figure 3.3: Vertical conduction band diagram resulting from the structure of figure 3.1 for temperatures of 10 K (a) and 300 K (b). The horizontal lines correspond to the first three energy levels of the quantum-well. The 0 axis corresponds to the Fermi level of the structure.

Table 3.1: Energy levels occupation in the quantum well for a lattice temperature of 10 K. The value of energy is relative to the Fermi level of the structure.

Magnitude	$\mathbf{E}_1$	$\mathbf{E}_2$	$\mathbf{E}_3$
Energy	-116 meV	-19.6 meV	1.69 meV
Carrier density	9.87×10^{12} cm^{-2}	1.65×10^{12} cm^{-2}	9.48×10^{9} cm^{-2}
Ratio	85.6 %	14.3 %	0.1 %

phonon energy in GaN (91.2 meV). About 85.6 % and 79.7 % of electrons are located on the first energy level for 10 and 300 K respectively.

As a consequence, the simulations demonstrate the viability of the structure designed in figure 3.1 and allows us to step forward to the next phase; the design of the masks in order to realize the devices.

3.1.3 Fabrication of masks

The layer mask of the samples has been introduced at the end of chapter 2, figure 2.25 page 48. Three different colors are represented for three different steps of the fabrication process. The green lines corresponds to the mesa realization. They are the etched areas to electrically isolate a part of the substrate from the others. Outside these zones, the channel does not exist anymore. The blue lines correspond to the realization of ohmic contacts. Contacts are made of a stack of Ti, Al, Ni, and Au. All the interdigitated

Table 3.2: Energy levels occupation in the quantum well for a lattice temperature of 300 K. The value of energy is relative to the Fermi level of the structure.

Magnitude	$\mathbf{E}_1$	$\mathbf{E}_2$	$\mathbf{E}_3$
Energy	-107 meV	-2.15 meV	38.5 meV
Carrier density	9.14×10^{12} cm^{-2}	1.60×10^{12} cm^{-2}	4.41×10^{11} cm^{-2}
Ratio	79.7 %	13.9 %	3.8 %

fingers fabricated on the bottom of the mask are made with these ohmic contacts. Finally, the red lines correspond to the Schottky contacts. This type of contact is mainly used in the top-right area of the mask, corresponding to the fabrication of HEMTs of different gate and drain-source lengths. On these devices, the gate is made of the Schottky contact. The top-left area is filled with testing devices such as *transmission line model* (TLM), *isolation test interdigitated fingers* or *Hall crosses*. These devices will be used in section 3.3.2 for the electrical characterizations of the samples.

For our study, the dimensions of interdigitated fingers are reported in table 3.3 corresponding to figure 3.4. The choice has been made to create devices with different spacing between contacts to further be able to observe the effect of the symmetry on the measured amplification. We also designed symmetrical devices to see if the problem regarding the different orientations of the electric field in the device, and already discussed in section 2.5.1 is real or not. These last symmetrical devices are named D2-31 and D3-31 in table 3.3. The surface of the samples have been maximized with respect to the technology limitations. The **F** length, corresponds to the distance between the tip of fingers and the opposite pad contact

Table 3.3: Dimensions (µm) of interdigitated fingers of the mask of figure 2.25.

Device	**A**	**B**	**C**	**D**	**E**	**F**	**G**	**H**
D2-6	2	6	56	522	464	8	500	100
D2-8	2	8	54	520	464	8	500	100
D2-16	2	16	46	512	464	8	500	100
D2-21	2	21	41	507	464	8	500	100
D2-31	2	31	31	497	464	8	500	100
D3-6	3	6	56	522	464	8	500	100
D3-8	3	8	54	520	464	8	500	100
D3-16	3	16	46	512	464	8	500	100
D3-21	3	21	41	507	464	8	500	100
D3-31	3	31	31	497	464	8	500	100

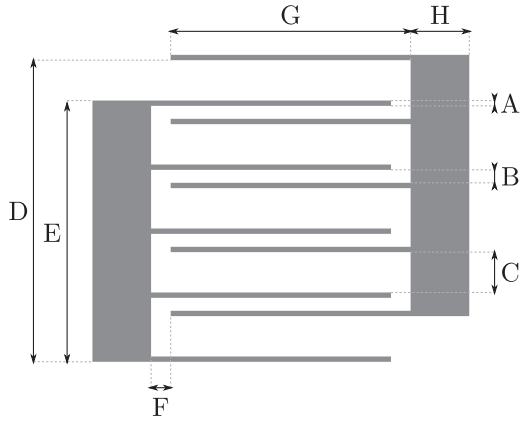

Figure 3.4: Dimensional parameters of interdigitated fingers. The real number of fingers is not exact for clarity.

3.2 Fabrication process

3.2.1 Substrates

For the time being, the realization of native substrates like for Si, InP or GaAs is impossible in the case of GaN. Even if it is possible to fabricate some bulk GaN [Yamane 97, Lucznik 05, Kucharski 09], the fabrication of GaN substrate is still a challenging and expensive task. Such substrates can be fabricated by hydride vapor phase epitaxy (HVPE) technique on an other material and further separated of the latter to keep the GaN part. As a consequence, most of the GaN devices fabrication starts from a sapphire (Al_2O_3), 6H-SiC, 4H-SiC or Si(111) [Morimoto 73, Liu 02], and more recently, Si(001) [Joblot 05] substrates. These substrates have several advantages and drawbacks which are summarized in table 3.4

Table 3.4: Different advantages and drawbacks of some possible substrates for GaN growing.

Substrate	Advantages	Drawbacks
Sapphire	– Acceptable cost ; – thermal stability ; – transparency in a wide range of wavelengths.	– Low thermal conductivity ; – important lattice constant mismatch (14%) ; – important thermal dilatation mismatch (-25%) ; – electrically insulating.
SiC	– Good thermal conductivity ; – low lattice constant mismatch (3.5%).	– Expensive ; – absorbent for some part of the visible spectrum ; – diffusion of Si atoms.
Si	– Low cost ; – good quality (this is the most used substrate, and it is well mastered since a long time).	– Very important thermal dilatation mismatch (116%) ; – important lattice constant mismatch (-17%) ; – diffusion of Si atoms.

We thus chose to use in a first time a sapphire substrate for its optical properties as well as for its cost, but in a near future, samples grown on GaN substrate [2] will be fabricated and tested. Hence there will be less parasitic scatterings in the channel and a better efficiency of the device.

3.2.2 Process

The presently available technical processes to grow GaN structures are mainly hydryde vapor phase epitaxy (HVPE), metallorganic vapor phase epitaxy (MOVPE), and molecular beam epitaxy (MBE). HVPE method was the first to be used in 1969 [Maruska 69] to build single-crystalline GaN. This technique is still used and allows deposition at a speed of the order of 100 µm/h [Cadoret 99]. From an industrial

2. These GaN substrates are to be manufactured by LUMILOG

point of view, the principal technique used is the MOVPE. Indeed it allows the growth of GaN as well as compound of AlGaN with good characteristics (acceptable dislocation density, flexibility, speed). The deposition speed of this technique is of the order of 5 µm/h. Finally, the technique used to grow our samples is the MBE. Its growth speed is slow (typically 1 µm/h), but it allows to control the process up to the monolayer of material. The flow of nitrogen into the chamber of the MBE can be made by two different kind of sources: ammonia, or a nitrogen plasma. In our case the injection of ammonia is used to fabricate the samples.

A schematic diagram of an MBE machine is shown in figure 3.5. Generally, these machines consists of three vacuum sections, of which the growth chamber is the most important. Before entering this section, the wafers transit through the buffer section, where they are prepared and stored. A lock is used between the two chambers to maintain the integrity of the vacuum while transferring a sample. The wafers are loaded onto a rotational magnetic holder known by the acronym, Continual Azimuthal Rotation (CAR). Cryoshrouds are used in conjunction with the conventional vacuum system to keep the partial pressure of undesirable gases such as CO_2 and H_2O around 10^{-10} mbar. The principle of operation is that gaseous substances are bound to the cold surfaces within the pump by means of cryocondensation, cryosorption or cryotrapping. Epitaxial growth starts with the heated cells, called effusion cells or Knudsen cells, that contain a compound required for the addition of a particular atomic species into the vacuum chamber. Each source is independently heated until atoms of the source material are able escape by thermionic emission.

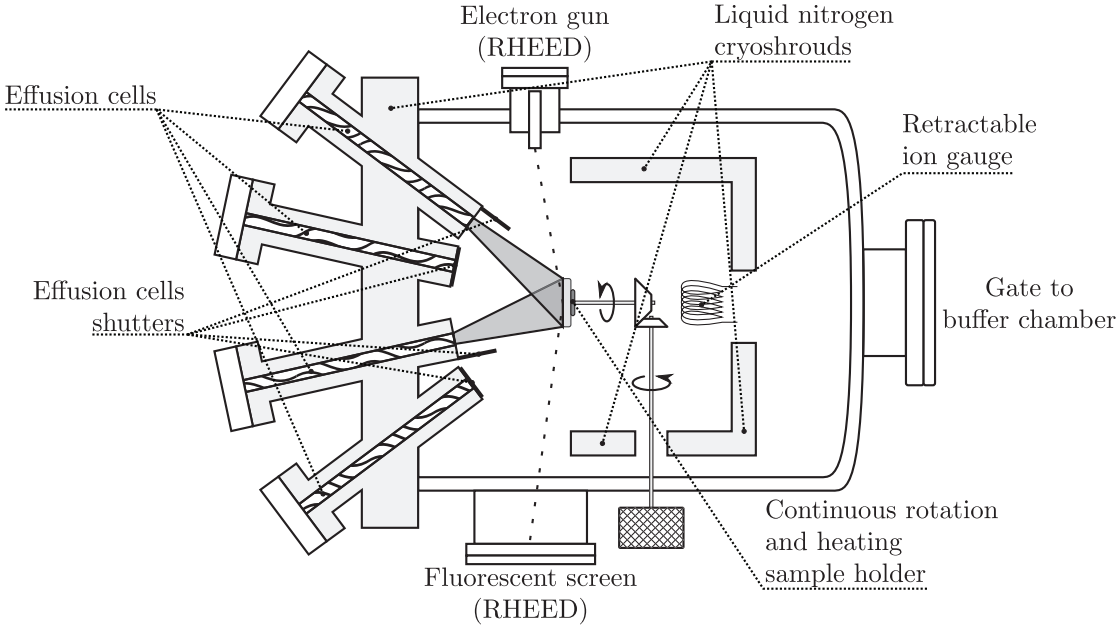

Figure 3.5: Schematic diagram of a MBE machine.

Atoms generated by the cells can have a long mean-free path within the ultra-high vacuum and collisions with other atoms are infrequent. They are traveling in the chamber following a straight line until they collide with the substrate material. The choice of atoms is made by controlling the shutters of the different cells. The typical rate of growth with MBE is around a single mono-layer per second. Although slow, this allows for abrupt changes in material composition. Under the right conditions, the beam of atoms will attach to the substrate material and an epitaxial layer will begin to form.

An ion gauge mounted to face the beam sources and is used to control the thickness growth by

measuring the Beam Equivalent Pressure (BEP) of the material sources. Alternatively, Reflection High-Energy Electron Diffraction (RHEED) is another useful measuring technique. Electrons are emitted from an electron gun at a glancing incidence to the CAR. The reflected and diffracted electrons emit light in a distinctive pattern when they strike a phosphor screen. Starting from a flat substrate, the electrons are not scattered greatly and are recorded as an intense beam. As material is deposited on the surface, the atoms create islands of epitaxial growth with a concomitant decrease of the reflectivity of the surface. As the deposition process continues, material builds up on the surface, the islands join together and create new flat surfaces with the original substrate becoming voids in the newly created material. As yet more material forms, the voids begin to fill up and the reflectivity increases once again. Although in reality, the reflectivity does not reach as high a value, since the process of deposition is random and the surface never regains the completely flat profile of the initial polished substrate, but monitoring the oscillations in the reflectivity gives an appraisal of thickness and rate of growth of the epitaxial material. For increased accuracy of the growing speed measurement, a laser reflectivity device is also embedded in the bench.

3.3 Post-process characterizations

After the completion of the fabrication process, the samples are characterized in order to analyse some properties such as roughness, mobility, etc.. The first group of characterizations is optical, while the second one is electrical.

3.3.1 SEM - AFM imaging

The SEM images can be used to measure the effective lengths of the patterns drawn on the mask. Indeed, there is always a difference between mask design and realized devices. Figure 3.6 summarizes some magnified views of the fabricated samples while table 3.5 reports the real lengths of the devices measured by using SEM studies. It appears that the contacts are bigger than expected, but the asymmetry of active and passive zones is respected.

Table 3.5: Dimensions (µm) of interdigitated fingers measured by SEM.

Device	**A′**	**B′**	**C′**	**F′**
D2-6	4	4	54	6
D2-8	4	6	52	6
D2-16	4	14	44	6
D2-21	4	19	39	6
D2-31	4	29	29	6
D3-6	5	4	54	6
D3-8	5	6	52	6
D3-16	5	14	44	6
D3-21	5	19	39	6
D3-31	5	29	29	6

The second performed characterization is the use of atomic force microscopy (AFM) to evaluate the quality of the surface of the grown sample. It informs on the growth quality. In the case of the sample PTC465, the obtained image is represented in figure 3.7. It indicates a roughness at the surface of 3.97 nm

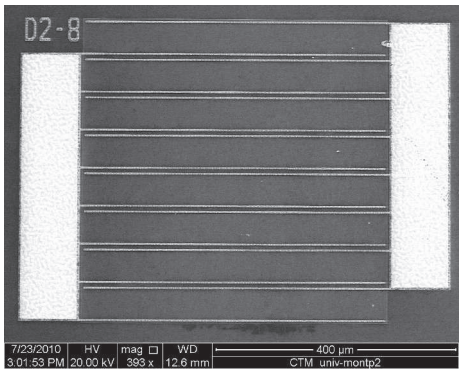

(a) PTC465 fingers D2-8

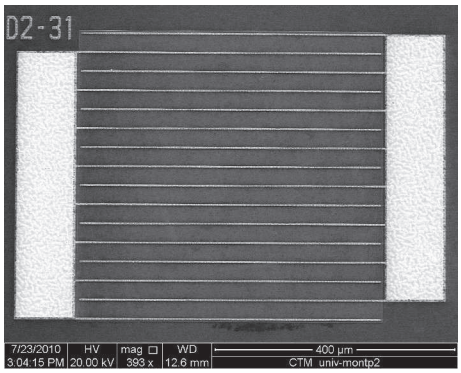

(b) PTC465 fingers D2-31

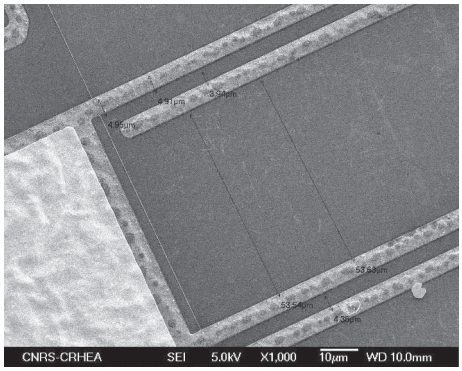

(c) PTC465 fingers D3-6

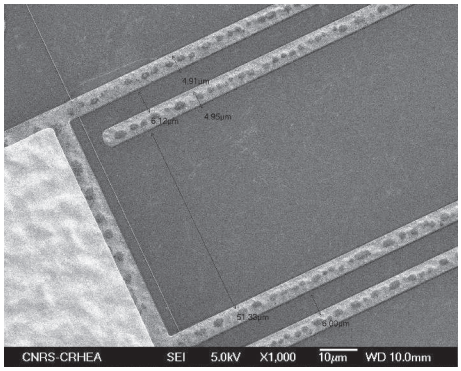

(d) PTC465 fingers D3-8

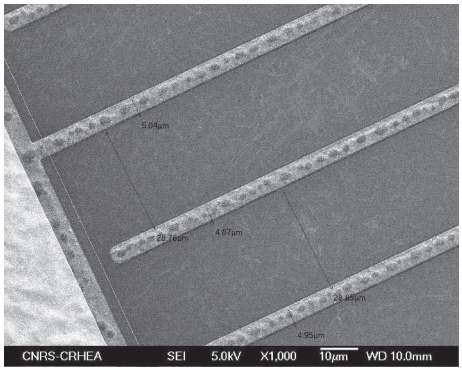

(e) PTC465 fingers D3-31

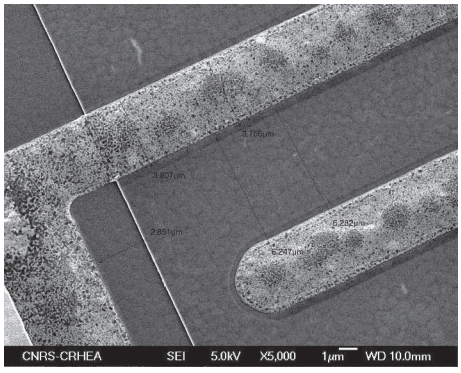

(f) PTC465 fingers D2-8

Figure 3.6: Large and magnified views (a-f) of interdigitated fingers obtained by SEM studies.

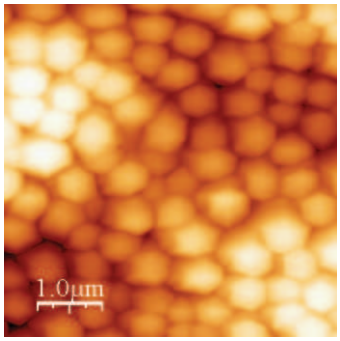

Figure 3.7: Sample surface observed with AFM studies. The measured roughness on the PTC465 sample is 3.97 nm

without visible *nanopipes* [3]. This means that there is few dislocations to be and the conductive channel is of good quality. AFM measurements also reveals a dislocation density of $\approx 4 \times 10^8$ cm^{-2} confirmed by cathodoluminescence techniques. This measurement is in agreement with Lumilog data.

3.3.2 Electrical characterization

The electrical characterizations are performed on the grown samples to measure properties such as concentration of electrons in the channel, mobility, sheet resistance, or quality of insulation after etching [Baron 09]. The results are summarized in table 3.6. The methods used to measure these characteristics (capacitance-voltage, Hall-Van der Pauw, isolated combs, transmission line model) are described in appendix A.

Table 3.6: Summary of electrical properties measured at room temperature of the PTC465 sample.

Magnitude	**Method**	**Value**	**Unit**
Electrons concentration in the channel	Capacitance-Voltage	1.01×10^{13}	cm^{-2}
	Hall measurement	1.03×10^{13}	cm^{-2}
Etching insulation	Etched interdigitated fingers (10×100 µm)	2.10	µA @ 30 V
Sheet resistance	Hall-Van der Pauw	283	Ω/□
	Transmission line model	294	Ω/□
Contact resistance	Transmission line model	1.2	Ω.mm
Electron mobility	Hall measurement	2150	cm^2/V.s

The measured mobility is among the best of today available devices of this kind [Frayssinet 00, Hu 09], and the carriers concentration is close to the one predicted in section 3.1.2. The current-voltage characteristics of interdigitated finger devices reported in figure 3.8 show that all the structures behave like a resistance of the order of 15 Ω.

3. The nanopipes are some lack of crystals at positions where the mismatch of lattice constant could not be compensated by the materials.

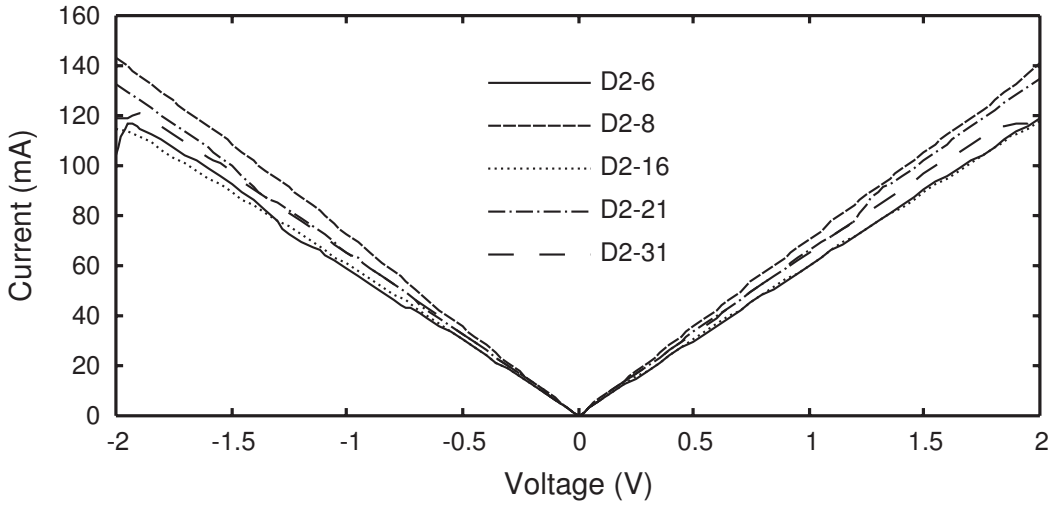

Figure 3.8: Current-voltage characteristics of different fabricated interdigitated fingers.

3.4 Summary

We described in this chapter the logical sequence we followed to fabricate the samples from both theoretical and experimental points of view. The synthesized devices have been both electrically and optically characterized to extract their expected performances. It has been shown that the quality of our devices is among the best of today available samples of this type, which was one of the condition to achieve to expect the better results regarding the simulations of chapter 2. The next step is the realization of the experimental benchs needed to investigate these samples.

Chapter 4

Experimental configurations: a final step before experiments



As discussed in chapter 2, the fabricated devices (chapter 3) may amplify any incident wave having a frequency from 0.2 up to 7.5 THz; the amplified frequency depends on the applied voltage accross the device (i.e. on the applied electric field). This chapter presents the design and building of the experimental setup to investigate this phenomenon. The experimental past of research work was started from scratch followed by the purchase of major equipments from the vendors.

The first section will recall the aim of the experiments and the specifications to respect. The second section will focus on the design of the bench while the third one will describe the full characterization of it. Then, a systematic procedure to achieve as accurate as possible measurements will be proposed, and finally, another setup to measure continuous and pulsed current-voltage characteristics will be introduced.

4.1 Aim of the measurements

Using the devices grown by the CRHEA and detailed in chapter 3, our ain is to detect an amplification of an incident electromagnetic wave, depending on the applied voltage on the device maintained at cryogenic temperatures. Starting from the theoretical predictions presented in chapter 2, the whole experiment has been designed and realized.

4.1.1 Goal to achieve

The main goal of our experiments is to show the amplification of our freshly fabricated devices. For this purpose, we need an experimental configuration able to measure the transmission spectra of both unbiased and biased devices in the considered frequency range. In a first time, the comparison between these two spectra will inform about the effect of the applied electric field on the transparency of the studied sample. In a second time, the power gain of the devices will be investigated. This measurement is rather delicate and the section 4.3.3 will detail our approach to evaluate it.

These measurements are also completed by a detailled investigation of current-voltage characteristics under different conditions: this represents an important step to verify the behavior of the fabricated samples but also it enables the extraction of interesting physical informations.

4.1.2 Experimental conditions

To produce an amplification of the THz radiations as suggested in simulations, the samples have to be maintained at cryogenic temperatures. Keeping the samples cooled down to temperatures below 100 K involves the use of a cryostat. This instrument is always complex to put in place in the experiments and will need special care during the alignment of the bench, due to invisible nature of the THz radiation.

Recalling that the experiments will consist in measuring the transmission spectra of our devices, it implies that the incident beam crosses the device and should be detected after transmission. In other words, the sample holder will have to be either transparent, or pierced to let the THz beam be extracted from the device for measurement. If the first solution is chosen, the transparency have to be effective in the entire frequency band of the investigation. During the present investigation, only two kind of sample holders have been suggested: the first, made-up of a ceramic without any specifications about its transparency within the THz frequency domain, and the other one, made of kovar; an FeNiCo alloy. We decided to use the latter one because it can be easily drilled, and we do not need any THz specification. These samples holders are standard TO-8 with 16 pins as presented in figure 4.1. These holders are

rounded shaped with a diameter od 15 mm. Figures 4.1(a) and 4.1(b) presents a photograph of the raw and 4.5 mm diameter drilled sample holder respectively, whilst figure 4.1(c) shows the final object which will be installed in the cryostat: a sample (one mask) is stuck with the help of silver paste on the pierced sample-holder. The bright paste on the left of the sample-holder is made-up of tin used to solder the cold finger of the cryostat as close as possible to the sample.

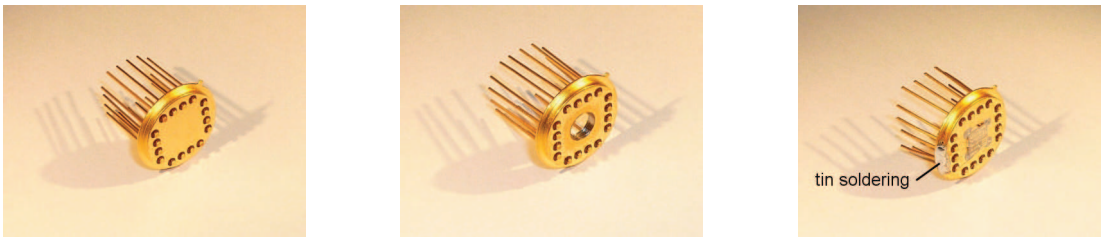

(a) Raw TO-8 (b) Pierced TO-8 (c) Pierced TO-8 with sample

Figure 4.1: Illustration of a TO-8 case with 16 pins, before (a) and after (b) piercing, and with a sample installed on it (c).

4.1.3 Frequency range of operation

The frequencies of investigation are those where the amplification of the investigated devices is effective, that is from 0.2 up to 7.5 THz. Unfortunately, as it has been described in chapter 1, there are only few sources able to generate waves in this particular frequency domain. The sources available at present in our laboratory are: the former, based on Schottky diodes frequency multipliers, converts RF frequencies to upper frequencies, and the latter, using a photomixing antenna, converts the beating frequency of two lasers into a continuous wave of this beating frequency. Both of these sources will be described in detail in section 4.2.1.2, however, the major part of the experimental investigations have been made with the electronic source.

As far as the detection part is concerned, we also dispose of several solutions which will be discussed in section 4.2.1.3. The main components are a spectrum analyzer, a bolometer, and the photomixing detector associated with the previously introduced source.

4.2 Setup design

The main objective of this section is to describe all the technical equipments which are used in our experimental configuration. The role of each part will be described at length.

4.2.1 Instruments

4.2.1.1 Cryostat

The core of the experiment is inside the cryostat, where the samples are installed. A special attention thus have to be taken for this instrument which have to be flexible in terms of temperature as well as of easy opening for sample switching. Indeed, an experimental campaign has been led with one mask of samples installed into the cryostat, because the optical alignments do not allow us to easily switch among several samples. As a consequence, only one or two types of the identical devices (there are two

devices of the same type on a mask) can be connected at the same time inside the cryostat. The choice of the sample holder discussed in section 4.1.2 also limits us in term of number of accessible contacts on the sample (up to 16).

The cryostat (reference HDV-10 of IRLabs) is mounted with a helium closed cycle circuitry which cools down two concentric radiation shields to 77 and 15 K. The cold plate, located in the middle of the cryostat, is the bottom plate of a dewar. This dewar can be cooled with the help of a flow of liquid helium. In this conditions, the cold plate can be cooled down to 4.2 K. A second mode of cooling the cold plate is to directly fill the dewar with liquid nitrogen, without running the cold head. This operation will lead to a cooling of the cold plate down to 77 K. A bottom view of the cryostat is drawn in figure 4.2:

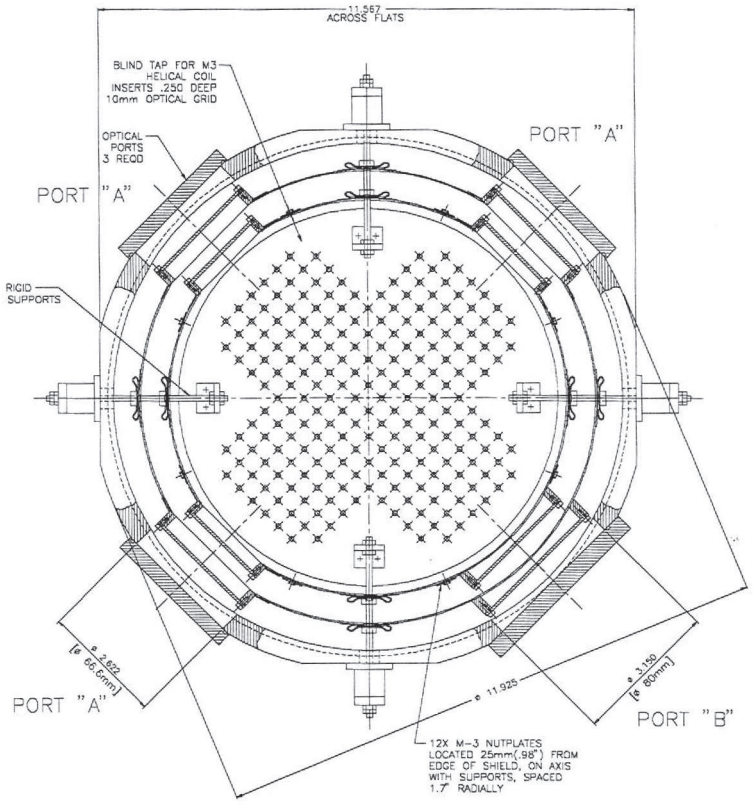

Figure 4.2: Inside bottom view of the cryostat, from IRLabs data sheet.

the cold plate, the windows and the radiation shields are visible. The total surface of the cold plate is quite big compared to our samples, but it will not be a problem for our experiments. Three temperature gauges are placed in the cryostat at different places: two probes are placed on the radiation shields, and the last one on the cold plate. These gauges allows a control of temperature during the experiments.

Figure 4.3 shows a photography of the cryostat. One can see the vacuum port, the pressure gauge, the cold head and the input/output windows which will be used to manage the THz beam.

In order to install the sample in the middle of the incident beam, a base plate has been designed. This plate has several uses: firstly, it is the electrical bridge between the sample holder of figure 4.1 and the feedthrough electrical wires coming from the top of the cryostat. The second utility is to stop the parts of the incident beam that may not cross the device, these parasitic reflexions thus have less chances to be detected at the output of the cryostat. This base plate placed into the cryostat can be seen on figure 4.4.

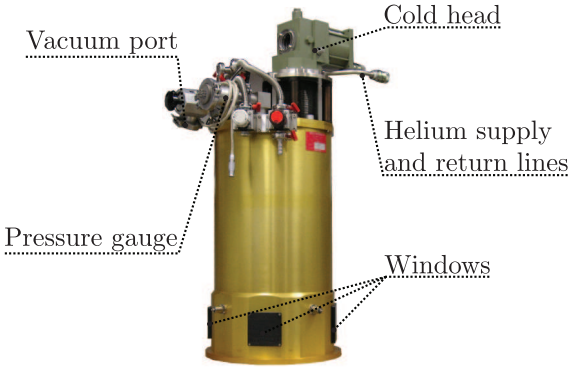

Figure 4.3: External view of the HDV-10 cryostat.

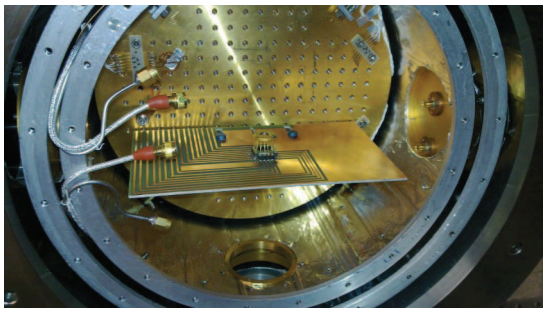

Figure 4.4: Base plate in place in the cryostat.

4.2.1.2 THz sources

Three different sources have been studied during the present work. None of these were available and operational at the beginning of the project, but a long time was dedicated to fix these sources, especially the photomixing source. Finally, due to lack of time, the only source that has been implemented on the complete bench is the first electronic source. The other ones will be used in future investigations.

0.220 – 0.330 THz electronic source

This commercial source is purchased from Spacek Labs. This company mainly builds custom systems in the millimeter and sub-millimeter wavelengths for spatial applications. The schematic diagram of the frequency conversion chain is sketched on figure 4.5. This system is based on frequency multiplication

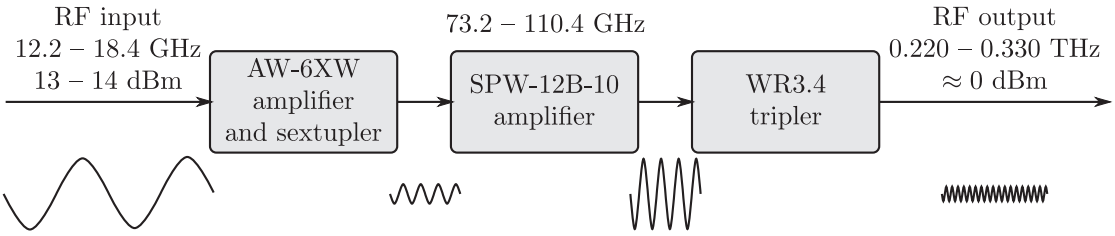

Figure 4.5: Schematic diagram of the 0.220 – 0.330 THz source from Spacek Labs.

using Schottky diodes-based components converting to its second or third harmonics the input frequency. Starting from a RF input ranging from 12.2 up to 18.4 GHz, the signal is amplified and converted by a first frequency sextupler stage to frequencies from 73.2 up to 110.4 GHz. This converted signal is then

amplified before being converted again by a frequency tripler, to finally reach frequencies from 0.220 up to 0.330 THz. The input frequency is thus multiplied by $\times 18$. The output power strongly depends of the considered frequency, as attests figure 4.6, representing the manufacturer test data.

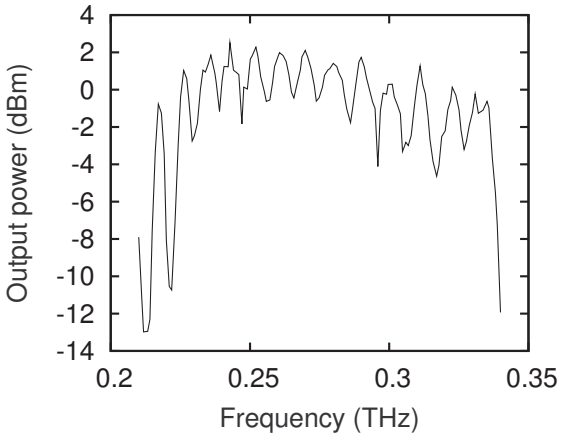

Figure 4.6: Output power as a function of frequency of the 0.220 – 0.330 THz source according to Spacek Labs data.

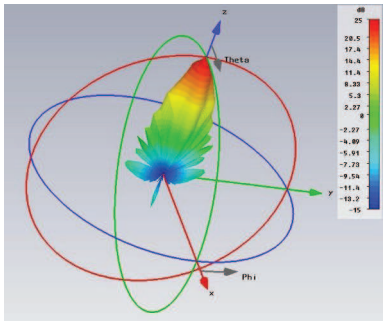

Figure 4.7: Radiation pattern of the output beam from the horn antenna.

The output power is extracted from the system through a waveguide of normalized dimensions WR-3.4 [1]. This wave guide provides a linearly polarized wave. In our case, we will directly screw a horn on the waveguide output to work with a free space beam.

The horn we chose is a rectangular horn. It keeps the polarization linearity of the beam, and generates an almost conic beam of 8.5° of angle (calculated at -3 dB). The radiation pattern of this horn have been simulated with the help of a finite element simulator (CST). The result is shown on figure 4.7.

0.843 – 1.100 THz electronic source

Besides the previous electronic source, a second one have been purchased from the VDi company, also mixing components from Spacek, VDi and Pacific Millimeter. A scheme of the conversion chain is represented in figure 4.8. In this chain, one can remark that there is only one stage of amplification, compared to the previous source that presented two stages. As a consequence, the expected output power is few (typically -20 dBm). The frequency conversion is made by four successive Schottky diode-based triplers, providing a total frequency multiplication of $\times 81$. The input frequency, ranging from 10.4 up to 13.7 GHz is thus converted to a 0.843 – 1.100 THz frequency band. As for the previous source, the output power strongly depends on the frequency, as it can be seen on figure 4.9, representing the VDi test data of our source. The last tripler of the chain (figure 4.10) is realized with an external removable passive component with a built-in diagonal horn, providing a 90 % linearized free space beam [Johansson 92].

0.75 – 1.9 THz photomixing source

We finally dispose of a photomixing source to generate THz waves. The system is composed of two parts: the antenna, and a laser system. The antenna is a commercial antenna from the Lithuanian company EKSPLA while the lasers system was bought to the German company Sacher Lasertechnik.

1. Referenced as such by the American *Electronic Industries Association*. At present, the *International Electrotechnical Commission* standards does not cover this frequency range.

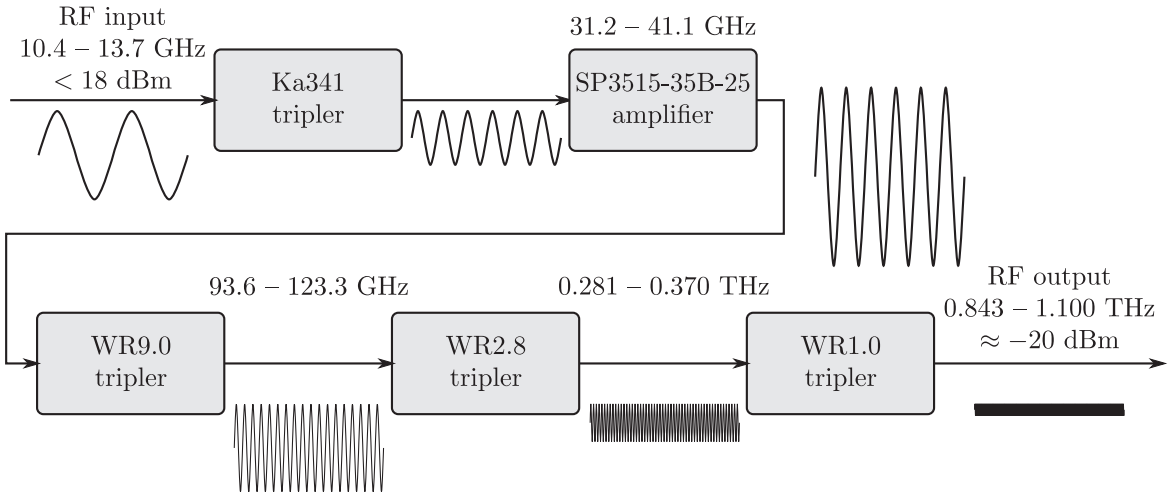

Figure 4.8: Schematic diagram of the 0.843 – 1.100 THz source from VDi.

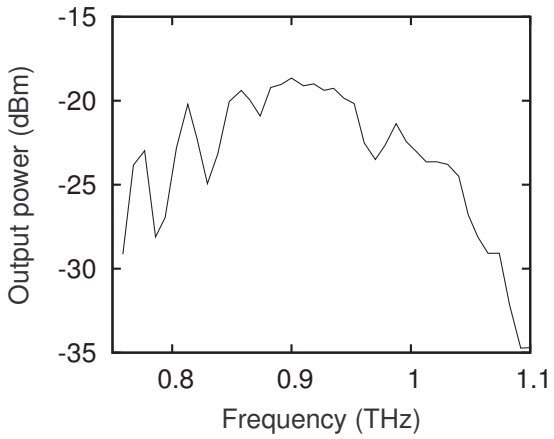

Figure 4.9: Output power as a function of frequency of the 0.843 – 1.100 THz source according to VDi data.

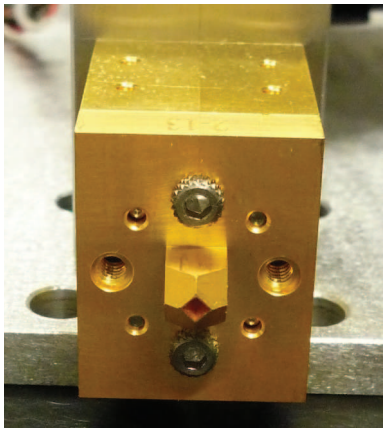

Figure 4.10: Final stage of the 0.843 – 1.100 THz source, showing the built-in diagonal horn.

The EKSPLA emitter consists of a microstrip photoconductive antenna fabricated on low-temperature grown GaAs (LT-GaAs) substrate pumped by an optical beating generated by the Sacher system [Matsuura 97, DiDomenico 62]. THz radiation is collected and collimated by an integrated Si lens, mounted on a X-Y stage. The photoconductive antenna geometry, the parameters of the Si lens, as well as the properties of LT-GaAs epitaxial layers are optimized for highest THz radiation output efficiency while preserving optimal bandwidth. This type of antenna are also able to operate in pulse regime [Tani 02] generally coupled with a Ti:Sapphire femtosecond laser to make time domain spectroscopy [Van Exter 89, Grischkowsky 90], but it is known that a continuous-wave regime is possible with the same objects [Brown 95, Matsuura 97, Czarny 07]. Indeed, the main property needed to generate THz continuous wave is the same that for the pulsed regime: a short life-time of the electrons ($\approx$ 1 ps).

The resistivity of the semiconductor material used in these photomixers is modulated by the optical beams focused on it. This modulation occurs at a frequency equal to the frequency difference between the two lasers beams. As a consequence, if a continuous voltage is applied on it, the photo-generated electron-hole pairs drift to the contacts under the action of the electric field. The simultaneous detection of the two lasers generates a current modulation which stimulates a coupled antenna. The latter thus

radiates the electromagnetic beam corresponding to the modulation frequency. The characteristics of the generated beam directly depends of the properties of the incident laser beams (spectral purity as well as frequency).

The mounted antenna is in our case a resonant dipole antenna [Kominami 85], but other wide-band types (bowtie, logarithmic [Mendis 04], Vivaldi [Greenberg 03], fractal [Gaubert 03, Werner 03], spiral [Dyson 59], etc.) have also been implemented for a better efficiency over the whole frequency band of operation. A scheme of our antenna is illustrated in figure 4.11.

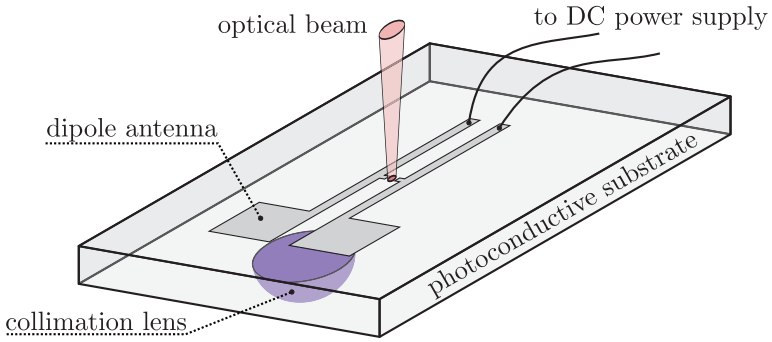

Figure 4.11: Illustration of the photomixing source from EKSPLA.

As far as the lasers are concerned, we have used two distributed feedback (DFB) lasers emitting around 780 nm, wavelength of sensitivity of the antenna. Both of the lasers are controlled in temperature and current to stabilize them as well as to adjust their wavelengths and amplitudes. The latter point is a crucial characteristic to master because these parameters directly rule the frequency of the generated THz beam and the efficiency of the antenna. The optical power recommended by the manufacturer to obtain the optimum operation while staying in the security margin of the component is of the order of 100 mW. Since the generated power of the two lasers is insufficient to reach that value, an additional tapered semiconductor optical amplifier (SOA) have been added to the system. Finally, the laser system is sketched in figure 4.12. We are able to obtain a laser power at the output of the fiber between 100 and

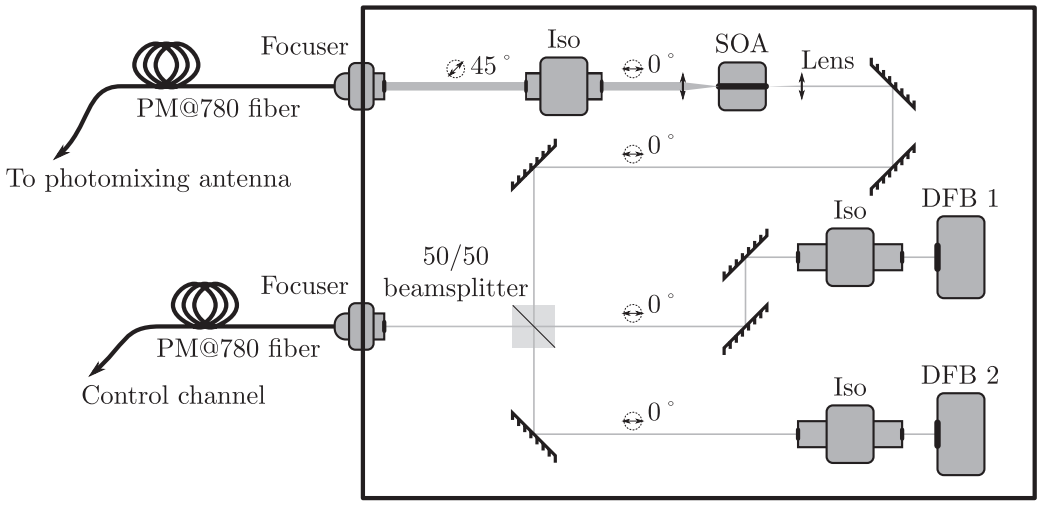

Figure 4.12: Internal scheme of the Sacher laser system. The arrows on the beams reports the linear polarization angle.

200 mW. The *control channel* output of the box was initially made to measure the equilibrium between the two lasers powers. Despite the alignment difficulties of coupling the two laser beams in the fiber of that port, it turned out that the non-linearity of the amplifier is too important to consider that this port faithfully accounts for the wavelengths equilibrium at the output of the second port. We thus decided to use a 99/1 polarization maintaining fiber coupler at the amplified output for control on an optical spectrum analyzer (OSA). Using ths scheme we are ensured to observe a faithful component of the beam which goes to the photomixing antenna. The final system is sketched in figure 4.13.

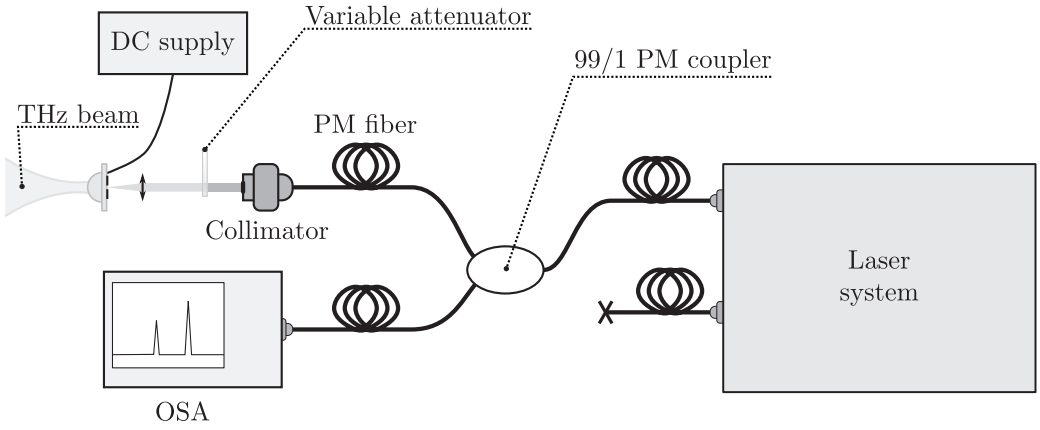

Figure 4.13: Full bench of THz generation with a photomixing antenna.

At this point, it is important to note that the polarization maintaining of both lasers is important until the laser beam reaches the photomixing device. Indeed, the optical beating of the two wavelengths will only occur if both are linearly polarized in the same direction. If this condition is not achieved, the conversion of the beating into a THz wave by the photomixing antenna will not be possible. This is the reason why we chose only polarization maintaining optics from the DFB lasers up to the antenna.

The origin of frequency limitation of the bench is not unique. On one hand, the system is limited in term of frequency by the bandwidth of the antenna, but on the other hand the limitation is also linked to the possible wavelengths variations of the lasers (from 780.5 up to 781.7 nm for the laser 1, and from 783.2 up to 784.5 nm for the laser 2). These variations are directly related to the possible temperature variations of the lasers. Indeed, to sweep the wavelength of a DFB laser, one should play on its temperature. In our case, the manufacturer limited this range from 10 to 40 °C for each laser. The reachable optical beating frequency band is thus from 0.75 up to 1.90 THz as figure 4.14 testifies. This figure have been realized by sweeping the temperature and currents of the two lasers, and measuring the wavelength with the help of the OSA.

In order to control the whole photomixing system (including lasers as well as the photomixing device and the OSA), I realized a Labview program able to automatically sweep the current and temperatures of the two lasers. It is thus possible to make some continuous wave THz spectroscopy in the frequency excursion of operation of the system. The program algorithm is detailed in appendix B, while a brief description of the program use will be exposed in section 4.4.1.

4.2.1.3 THz detectors

Concerning the detection part of our spectroscopic bench, we had the choice among three different systems: a silicon bolometer, a photomixing detector, and an electronic mixer coupled with a spectrum

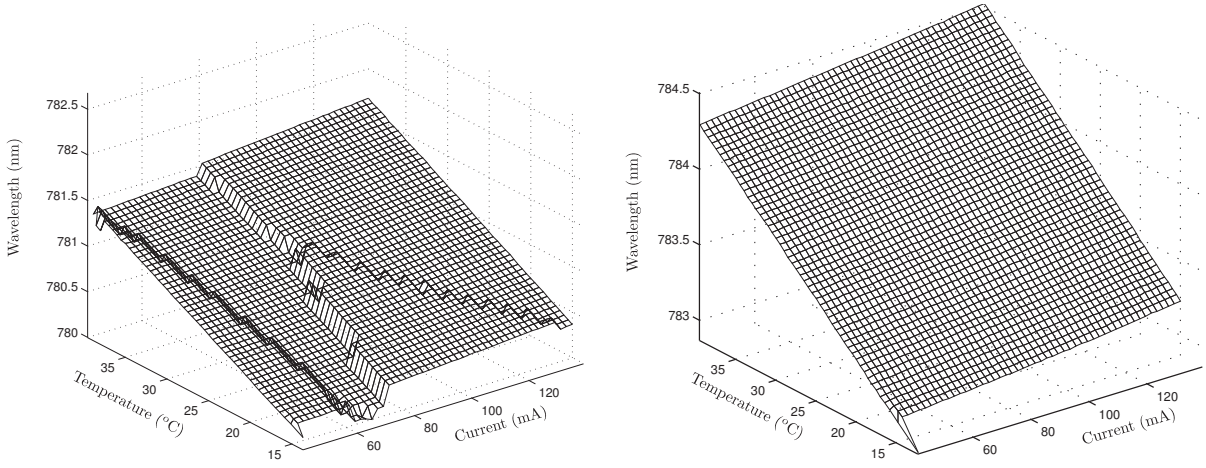

(a) Laser 1 (b) Laser 2

Figure 4.14: Wavelengths characterization of the lasers.

analyzer.

Bolometer

Our bolometer is a commercial one, manufactured by Infrared Laboratories, producing infrared bolometers since 1967. It is a Silicon-based bolometer, and a scheme is reported in figure 4.15. A baffle tube associated with a Winston cone horn, focus the signal to measure from the input window to the detector which is placed in the middle of the cold plate. The cold module (J-FET), bringing the first conversion of the measured signal is mounted on a calibrated feet providing a 60 K temperature to the transistor, which is screwed on the cold plate. The input window is wedged with white polythene and diamond powder layer, while the filter wheel carries three different materials allowing to change the cut-off frequency of the system. Position 1 corresponds to 18 THz far infra-red cut-off type filter consisting of thin white polythene stretched tightly over holder rings and overlaid on one face with 5/10 µm diamond scatter layer, while position 2 is related to 3 THz cut-off type filter consisting of 1.91 cm diamond wedged crystal quartz, 1 mm thick, over coated with garnet powder. However, position 3 corresponds to 1 THz cut-off type filter consisting of wedged fluorogold in series black polythene. The main characteristics of the bolometer are summarized in table 4.1.

Table 4.1: Summary of bolometer characteristics according to IRLabs data.

Magnitude	**Value**	**Unit**
Sensitivity	2.48×10^5	V/W
Noise equivalent power	2.51×10^{-13}	$W/\sqrt{Hz}$
Filter 1 cutoff frequency	1	THz
Filter 2 cutoff frequency	3	THz
Filter 3 cutoff frequency	18	THz
Maximum modulation frequency	500	Hz
Full sensitivity maximum frequency	40	Hz

The main advantage of such an instrument is the very high sensitivity of the power detection (2.48×10^5 V/W). In addition, an amplifier is built-in on the bolometer to provide a 200× or 1000×

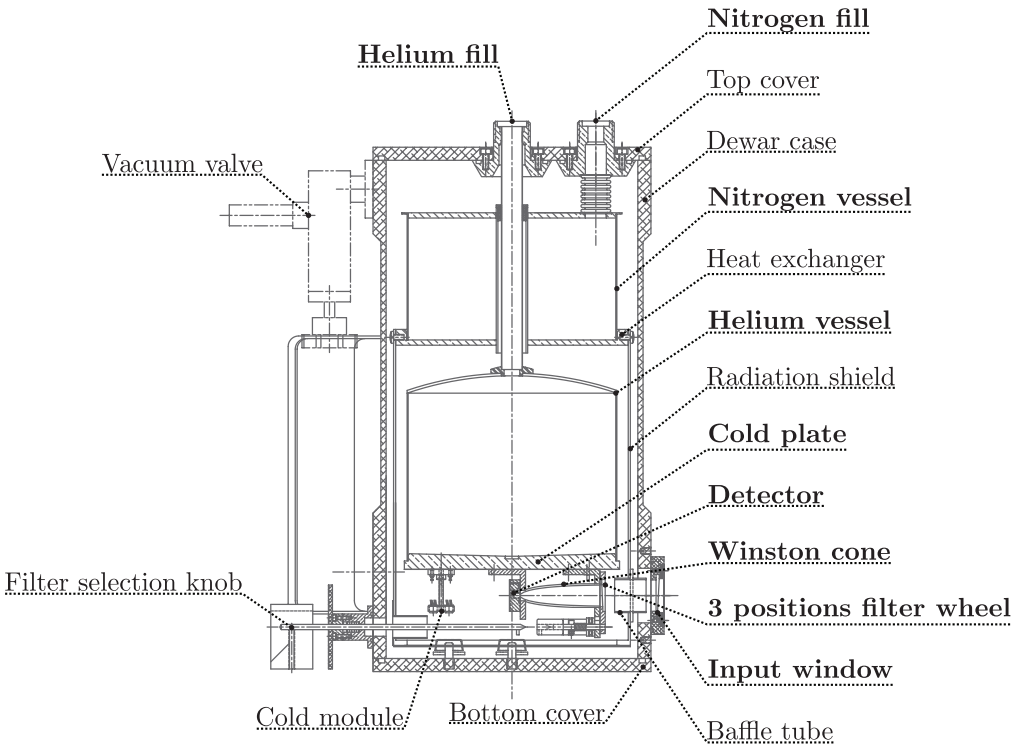

Figure 4.15: Internal scheme of our bolometer. Credits: Infrared Laboratories.

amplification of the detected signal. There are two major drawbacks of this instrument. Firstly, it has to be cooled down to liquid helium temperatures: this involves a serious management of the experiments. In the case of the use of a lock-in amplifier, the chopping frequency of the signal has to stay very low to keep the optimal sensitivity. This involves a long integration time of the downstream lock-in amplifier for high-accuracy measurements.

Homodyne photomixing detector

We detailed in section 4.2.1.2 the functioning of the EKSPLA photomixing source. We also earned the complementary photomixing detector which is homodyne with the source. Such a principle has already been used to obtain the THz imaging of several objects [Gregory 05]. If the same optical beating that is focused on the source is also focused on a detector [2], and if the THz beam generated by the source is sent to the THz antenna of the detector, then the mixing of the two phenomenon will generate (if they are in phase) a continuous current in a short-circuit of the electrodes of the antenna. The value of the generated current is directly proportional to the THz detected power. The variable delay line installed on the detection branch allows to set the phase between the THz signal and the optical beating, to optimize the detected signal. It is thus possible to extract the phase introduced by a given sample on the propagation of the THz waves through it. Figure 4.16 shows a complete THz spectroscopy bench involving generation and detection of THz waves using photomixing devices.

The main advantage of this kind of detection is the possible extraction of the phase introduced by the sample, but the drawbacks are numerous. First it has to be coupled with the photomixing antenna emitter, because the physical mechanism of the detection stands on the fact that the detected beam and the optical beating are coherent. If a third part generates some THz, it would be impossible to generate

2. the detector is the same unbiased photomixing antenna than the detector.

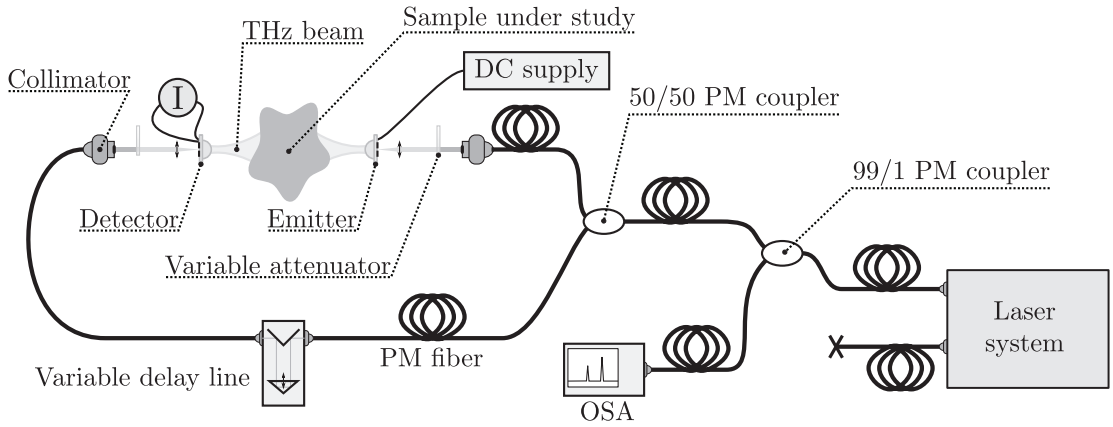

Figure 4.16: Full bench of THz generation and homodyne detection with photomixing antennas.

the coherent optical beating needed for the detection. Moreover, the optical alignment of this kind of system is not easy. In particular, the collimation lenses of the source and the detector are quite hard to handle. Finally, the power of the source is very low, so this system cannot be used on big benches requiring long distance and powerful THz beams.

Electronic mixers

We finally dispose of electronic mixers coupled with a spectrum analyzer. The most interesting mixers we have for this particular experimental bench are a 110 –220 GHz and a 220 – 325 GHz. The principle of these mixers is to mix a local oscillator generated by the spectrum analyzer itself with the signal to be detected. The mixing of the two signals generates a spectral component at lower frequency which can transit through classical RF wires. The spectrum analyzer thus has to *demodulate* the useful signal from the one issued from the mixer.

The main advantage of this technique is the use of a small detector which can easily be used in confined environments, or for quick measurements. It also present a very good noise level (≈ -85 dBm) and have a direct spectral view of the signal. The drawback is that at present we do not have mixers at frequencies higher than 325 GHz, and that the use of a lock-in amplifier to detect very low-power signals is not possible. Anyway, this detector will be mainly used in our experiments for alignment purposes.

Unfortunately the higher frequency mixer (220 – 325 GHz) broke down before I was able to use it on my bench. We still used the lower one (110 – 220 GHz) at its higher frequency to measure the signal of the lower-frequency electronic source (220 – 325 GHz) at its band bottom.

4.2.2 Description

Let us now build the whole setup using the previously described components. The cryostat, described in section 4.2.1.1 was bought with a cradle already mounted for millimetric measurements purposes at lower frequencies than those we are interested in, with two spherical aluminum mirrors. One of the two mirrors was designed to collimate a beam issued from a source, while the second one was used to focus a collimated beam on a detector. Both of these mirrors have the same diameter and are mounted on tilt micrometer screws for adjustment. This first use is described in figure 4.17.

This experimental scheme is not correctly configured according to our needs. Indeed, our goal is to measure transmission spectra of samples mounted in the center of the cold plate. The beam that reaches the sample has to be focused, while the source and detector will be placed outside the cryostat and

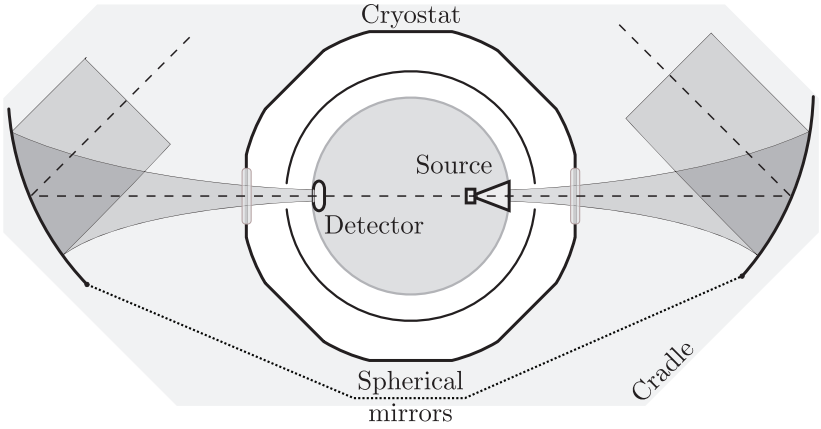

Figure 4.17: Cryostat mounted in its old configuration with its cradle and the spherical mirrors.

will respectively generate and detect divergent and convergent beams. Such a situation is sketched in figure 4.18. The position of the source and detector thus have to be evaluated. This will be calculated by the simulation of Gaussian beams according to the considered frequency range in section 4.2.3.

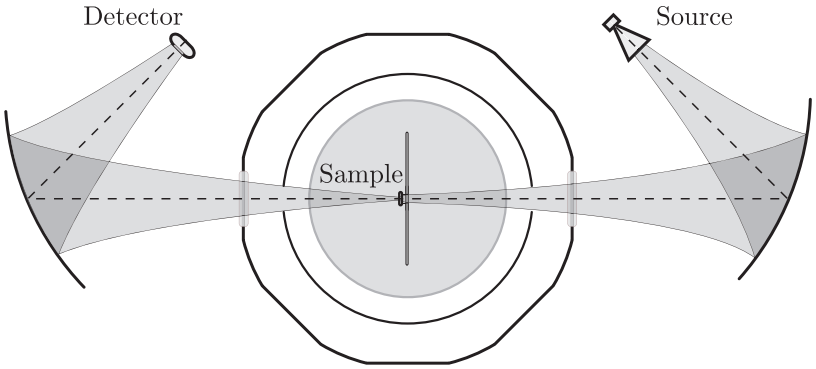

Figure 4.18: Cryostat configured for transmission measurements with the spherical mirrors.

One problem remains concerning the use of the cold head of the cryostat. In fact, this cold head generates many mechanical vibrations on the main body of the cryostat which may propagate on the optical table where the cryostat is maintained. These vibrations may affect the normal behavior of the source and detector used during the experiments. To avoid this problem, we decided to use two different optical tables carrying the cryostat and its mirrors on one side, and the source and detector on the other side. This setup is sketched in figure 4.19. As we will see in section 4.2.3, the position of the source imposes to use a deported arm, maintained on table 1, and able to place the source over table 2. The weight of the source on the arm is compensated by the use of a counterweight disposed at the opposite end of the arm.

The bench is now complete, but a last issue still remains: the setup has to be aligned so that the THz beam is able to cross the cryostat and the sample until it reaches the detector. For that purpose, the arm that supports the source is mounted on a **xy** linear stage, while its **z** (vertical) position is ruled at the middle of the input windows of the cryostat using a **z** linear stage mounted between the source and the arm. The three mirrors (the two spherical, and the last flat) are mounted on tilt adjustments, while their localizations are already set by the cradle of the cryostat. Finally, a lab jack is used to adjust the vertical

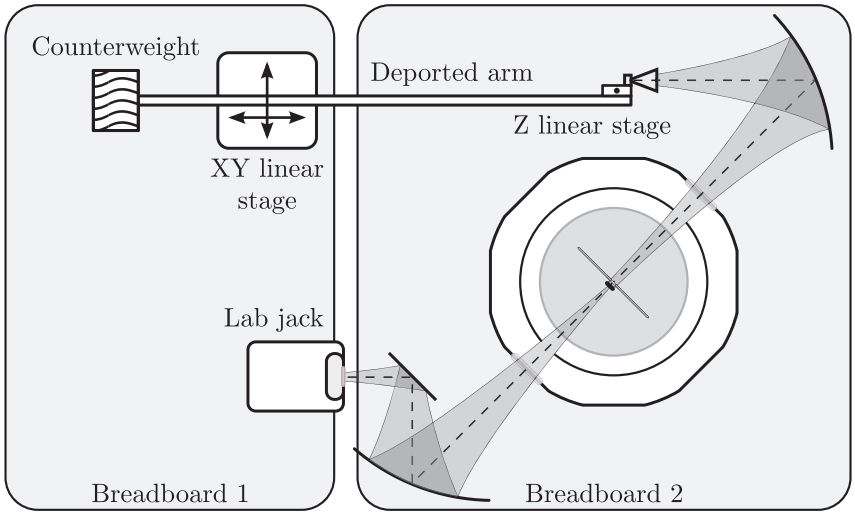

Figure 4.19: Illustration of the full bench with the two separated optical tables to avoid vibrations on source and detector.

position of the detector (especially for the bolometer) while its position in the **xy** plane is manually set. This last point is not critical when using the bolometer because the input window is quite large. The relative positioning of the bolometer with the incident beam can thus be set manually.

4.2.3 Optical alignment

The main problem to adjust a free space beam within the THz frequency domain is related to the fact that it is not possible to easily see and follow the beam during its travel on an experiment, and, to our knowledge, there exists at present no simple equipment to control the exact position of the beam. The electronic mixers introduced in section 4.2.1.3 are the easiest to handle detectors that we dispose of. The main handling difficulty is related to the RF wire connected to the detector which is quite hard to manage. We thus decided to realize, as a preliminary step, a simulation of Gaussian beams using Matlab. Then we realized a pre-alignment of the bench with the help of that simulations, and measured the shape of the real beam with the electronic mixers.

4.2.3.1 Gaussian beams simulation

The simulations were performed having as main objective to know where the source has to be positioned to obtain a focused beam in the center of the cryostat after being reflected on the first spherical mirror. We thus measured the characteristics of the spherical mirrors and the dimensions of the bench. I recall that the relative position of the spherical mirror with respect to the cryostat is constant and cannot be changed because they are directly screwed on the cradle of the cryostat. The distance between the two spherical mirrors is 68.1 cm, their radius is 25.4 cm, and their aperture diameter is 13 cm.

The result of the simulation is shown in figure 4.20. Here we considered a generated beam at 220 GHz from the source with the angle defined by the horn antenna mounted on it. We found that for this frequency, the right distance of the source from the first mirror is about 17.2 cm to obtain the focus point in the middle of the cryostat. One can see that the waist of the beam in the middle of the cryostat is of the order of 1 cm, which is far bigger than the size of the hole pierced in the sample holder. This means that the base plate will play a paramount role to remove the parts of the beam that does not cross the

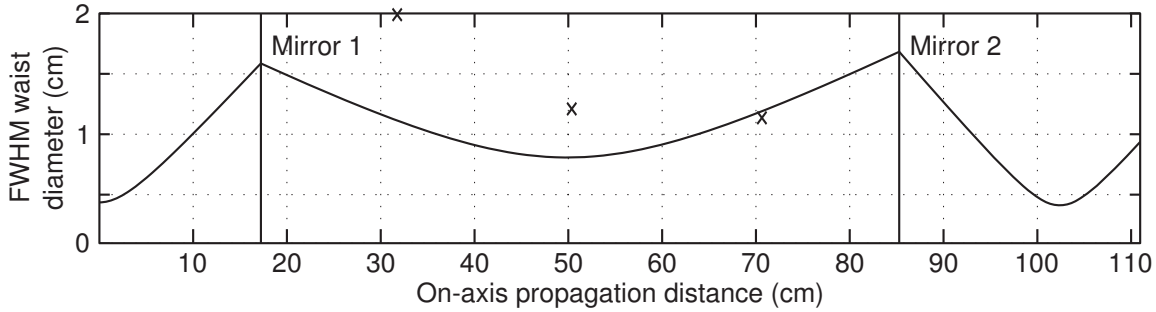

Figure 4.20: Simulation of the beam waist (FWHM) as a function of the on-axis propagation distance at 220 GHz. The crosses correspond to the measured points of section 4.2.3.2.

sample, as we already discussed in section 4.2.1.1. This is illustrated in figure 4.21.

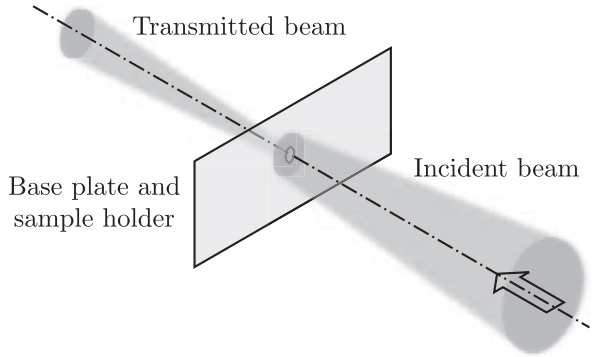

Figure 4.21: Illustration of the truncation of the beam induced by the base plate and the sample holder.

Another noteworthy result deals with the extracted divergent beam from the cryostat. It reaches the second spherical mirror where it is focused to an almost symmetric position that the one of the source with respect to the cryostat. This particular focusing point is the position where the detector has to be set up to obtain the maximum power.

4.2.3.2 Experimental implementation

To verify the simulations performed in the previous section, we realized some measurements with the help of the 220 – 325 GHz electronic source and the 110 – 220 GHz mixer coupled with the spectrum analyzer (see remark of section 4.2.1.3 for explanation). This allowed us to work at 220 GHz. We were able to manually perform 3D measurements of the beam power on its travel through the cryostat and draw a 3D cartography of it, according to the scheme reported in figure 4.22. The measurements were performed in three different planes along the propagation axis of the beam, after optimizing of the orientation of the first mirror and the relative position of the source with the first mirror. The center plane correspond to the center of the cryostat (where the sample is supposed to be) while the two other planes almost correspond to the input and output windows of the cryostat. The crosses reported on each measurement plane illustrate the measured FWHM of the beam on both **y** and **z** axis. As a result, with such a configuration, the beam is almost focused in the center of the cryostat (or, more accurately between the center and the output window), as the simulation predicted.

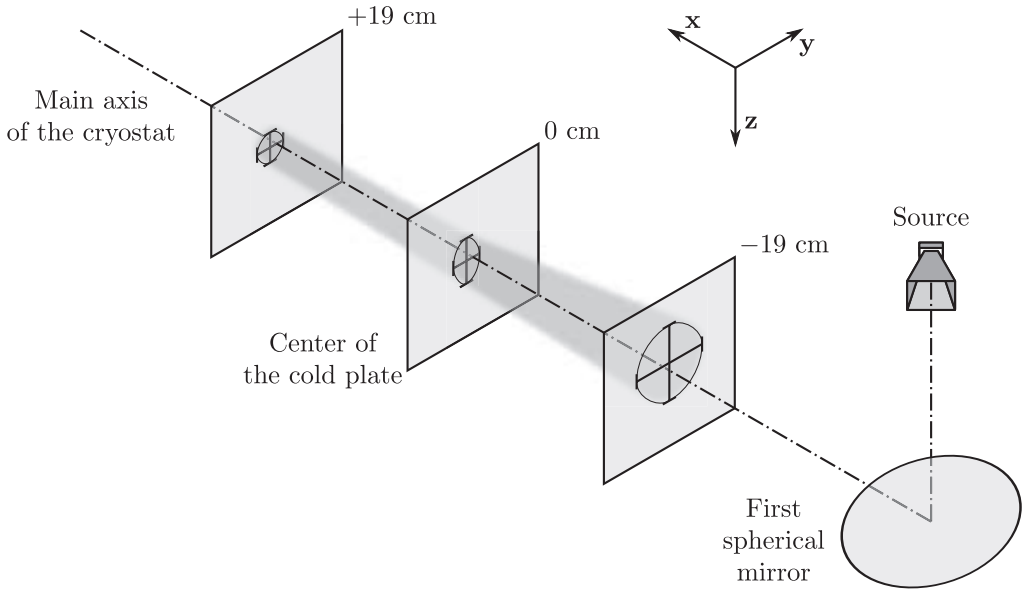

Figure 4.22: Measurements of the beam shape in the cryostat at 220 GHz. The planes correspond to those where the measurements were performed. The middle one is at the center of the cryostat. The drawn crosses correspond to the measured FWHM of power in each direction.

One should note that the configuration is not valuable for every frequency. In fact, the focus point shifts with the frequency value. This shift can be compensated knowing that the more the higher the frequency, the closer the first focus point will to the first mirror, as it can be seen on figure 4.23 showing the evolution of the beam as a function of frequency for a given position of the source. To compensate this effect, the source should be put closer to the first mirror to keep the focus point in the center of the cryostat. This result is not critical for the frequency band of an electronic source (the shift between 220 and 325 GHz is negligible), but one have to pay special attention while changing of source, for example by interchanging the two electronic sources (from 220 – 325 GHz to 0.843 – 1.100 THz).

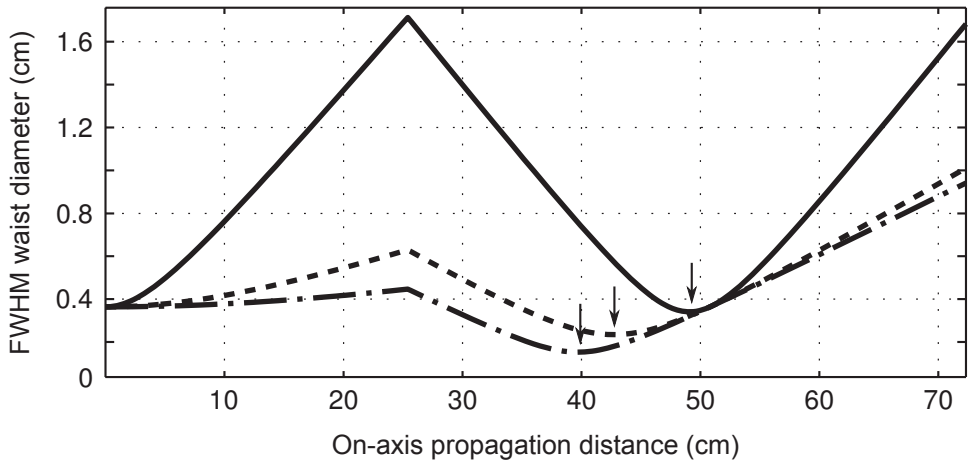

Figure 4.23: Simulation of the beam shape as a function of the on-axis propagation distance for three different frequencies. The plain, dashed and mixed lines respectively stands for 0.3, 1, and 2 THz. The arrows indicate the position of the focus point for the three different frequencies.

4.3 Characterizations of the bench

Now that all the components have been described and the alignment of the bench is achieved, we have to characterize the bench to know the main characteristics and the accuracy of the setup. We will start with the frequency characterization and the power properties, continue with the calibration of the bench without sample, and finally propose a technique to measure the absolute gain of the studied samples.

4.3.1 Frequency properties

As far as the electronic sources are concerned, the accuracy in term of frequency is very good. In fact, the stability is only limited by the upstream RF generator used for the frequency conversion. Concerning the spectral thinness, the non-linearities of the components used for the frequency conversion introduce some higher order resonances, but they are mainly filtered by internal filters as well as naturally rejected by the waveguides which are not adapted for these higher frequency modes. In conclusion, the limit in term of spectral thinness of the emitted beam is mainly limited by the upstream RF generator. These instruments generally show high quality spectral purity, as attest the manufacturer data of our RF generator, which are summarized in table 4.2. In all cases, if we try to measure the frequency thinness of our sources, it will be limited by the ultimate resolution of the spectrum analyzer, not by the source. For example, figure 4.24 shows the free-space spectrum of the 220 – 325 GHz operating at 220 GHz measured with the spectrum analyzer and the 110 – 220 GHz electronic mixer facing the source. The measured FWHM is of the order of 1 kHz, which is close to the resolution of the spectrum analyzer in that frequency domain and conditions of operations.

Table 4.2: RF generator (MG3692B) characteristics according to Anritsu data.

Magnitude	**Value**	**Unit**
Resolution	0.01	Hz
Single-sideband phase noise at 1 kHz offset, 10 GHz carrier	-110	dBc/Hz
Spurious harmonic-related or not	< -60	dBc

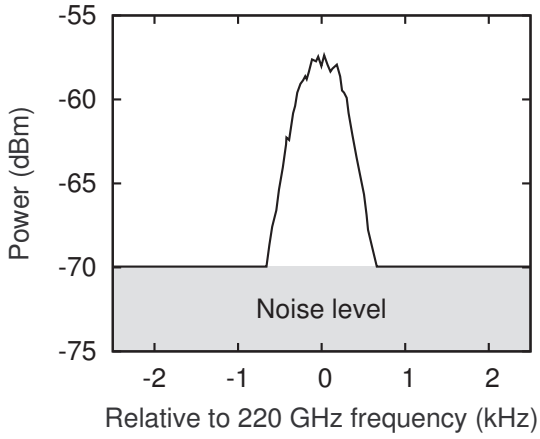

Figure 4.24: Measured spectrum of the electronic source working at 220 GHz in free space with the help of the spectrum analyzer and the 110 – 220 GHz electronic mixer. The low measured power (≈ -57 dBm) is explained by the fact that the source beam is divergent and is not focused on the detector.

Concerning the photomixing source, the limitation mainly comes from the laser system. The frequency resolution as well as the spectral thinness are related to the spectral thinnesses and stabilities of the lasers. The DFB lasers we are using present a FWHM of the order of $\approx$ 1 MHz which corresponds to a THz signal with a FWHM of $\approx$ 2 MHz.

4.3.2 Power properties

The three different sources that we can embed in our experiment present different ranges of frequencies and powers. Figure 4.25 summarizes their power as a function of the emitted frequency. The value of power given for the photomixing source (curve 3) is estimated by the use of the bolometer and a lock-in amplifier. The response of the bolometer is not sufficiently linear to be able to measure an accurate absolute value of the detected power. Anyway, that figure shows that for our sources, the emitted power dramatically drop down to very low values as the frequency increases (corroborating the general trend of sources discussed in chapter 1). As a consequence, we have decided to start our experiments by using the lower-frequency source (emitting sufficient power to be easily detected after crossing the cryostat and the samples), before trying to embed the other sources on the bench.

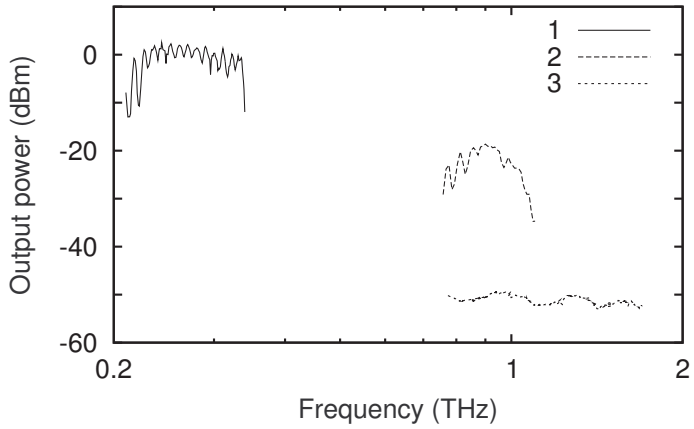

Figure 4.25: Output power as a function of frequency for our three sources. Curves 1 – 3 respectively stands for the 220 – 325 GHz, 0.843 – 1.100 THz electronic sources and 0.75 – 1.9 THz photomixing source. Note that the power of the photomixing source power have been evaluated using the bolometer.

During this thesis, we only had the time to embed the first electronic source on the full bench, even if the other sources have been characterized and optimized. This will be discussed in the conclusion of the manuscript as a near-future perspective of this work.

4.3.3 Gain measurement

As we will see in this section, the evaluation of the gain of a given device is not trivial. A special attention has to be paid in order to be able to obtain an accurate value of the effective gain of the device itself. In this section, a *sample* will designate a piece of wafer under investigation, while a *device* will stand for an object under investigation, typically an interdigitated finger. As a consequence, there are several devices on a same sample.

4.3.3.1 Context

As a first step, one can extract the gain of a sample by directly calculate the ratio of the transmission spectrum through the sample with bias $P_b(\nu)$ and the calibration spectrum of the bench without sample $P_c(\nu)$:

$$G_{raw}(\nu) = \frac{P_b(\nu)}{P_c(\nu)}\,, \tag{4.1}$$

This formula is not exact since the active area of the device under investigation is smaller than the size of the transmitted beam crossing the sample. This point is explained on the figure 4.26. Indeed, we want to extract the gain of a particular device rather than the whole sample. Indeed, a big part of the incident beam does not cross this device but the other parts of the sample. If we want to extract the gain of the device, we have to estimate the part of the beam which effectively passes through the device. That point is explained in section 4.3.3.2, whilst section 4.3.3.3 describes the calculation needed to obtain the effective gain of the device under investigation.

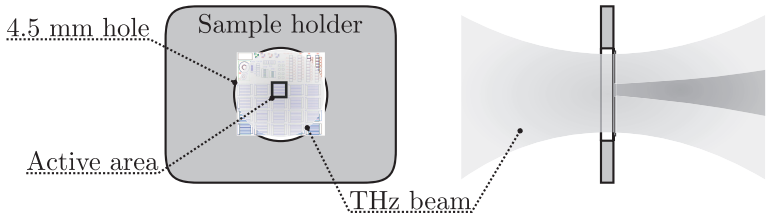

Figure 4.26: Front and side view scheme of the measured transmitted beam with respect to the device area

4.3.3.2 Relative area

In order to extract the part of the measured signal associated only with the device under investigation, a possibility is to evaluate the amount of power which effectively crosses the device. Indeed, the incident beam not only crosses the device but also the remaining area of the hole of the sample holder. If we estimate the relative area K of the device with respect to the hole size, it becomes possible to calculate the part of the beam crossing the particular device under investigation.

Let us assume as a first step that the beam power is uniformly spread over all the surface of the hole. The relative area can consequently be calculated by the formula:

$$K = \frac{device\ area}{hole\ area} = \frac{W_{dev} L_{dev}}{\pi d^2/4}\,, \tag{4.2}$$

where W_{dev} and L_{dev} are respectively the width and the length of the device and d is the diameter of the hole.

In reality, the beam power is not uniformly spread over the hole surface, but it has a Gaussian distribution shape. As a consequence, the part of power crossing the device may be under-evaluated. In other words, it is as if the device was bigger, and also the ratio K.

In our case, the hole diameter is 4.5 mm, and the device can be considered as a square of 500 µm side. The ratio K is thus equal to:

$$K = \frac{(500 \times 10^{-6})^2}{\pi (4.5 \times 10^{-3})^2/4} = 0.0157\,. \tag{4.3}$$

Therefore, we can presume that the real ratio K is above this value.

4.3.3.3 Effective gain calculation

Let us start from the fact that the measured power in the presence of a sample (biased or not) is the sum of the power crossing the device under investigation and the power crossing the remaining part of the hole:

$$P_{b_0}(\nu) = P_{d_0}(\nu) + P_{h_0}(\nu)\,, \tag{4.4}$$

$$P_b(\nu) = P_d(\nu) + P_{h_0}(\nu)\,, \tag{4.5}$$

where $P_{d_0}(\nu)$ and $P_d(\nu)$ are respectively the transmitted power of the device under investigation without and with bias, $P_{b_0}(\nu)$ and $P_b(\nu)$ are respectively the total measured transmitted power of the sample without and with bias, and $P_{h_0}(\nu)$ the transmitted power of the remaining part of the hole.
As discussed before, the slice of measured power attributed to the studied device $P_{d_0}(\nu)$ can be calculated with the help of the K ratio:

$$P_{d_0}(\nu) = KP_{b_0}(\nu)\,. \tag{4.6}$$

Subtracting equations (4.5) and (4.4), one obtains:

$$P_d(\nu) = P_b(\nu) - P_{b_0}(\nu) + P_{d_0}(\nu)\,. \tag{4.7}$$

Now we can replace $P_{d_0}(\nu)$ from equation (4.6):

$$\begin{aligned} P_d(\nu) &= P_b(\nu) - P_{b_0}(\nu) + KP_{b_0}(\nu) \\ &= P_b(\nu) + (K-1)P_{b_0}(\nu) \end{aligned}\,. \tag{4.8}$$

We can extract the part of the measured power due to the biased device under investigation from this last equation.

A last operation to extract the effective gain of the device is to calculate the part of the calibration spectrum measurement due to our device. As for the equation (4.6) we can link the part of power of the calibration that would have cross the device section $P_{d_c}(\nu)$ with the measured calibration spectrum $P_c(\nu)$ thanks to the K ratio:

$$P_{d_c}(\nu) = KP_c(\nu)\,. \tag{4.9}$$

Finally, the calculated effective gain $G_{d_e}(\nu)$ is the ratio of the calculated transmitted power of the biased device $P_d(\nu)$ and the calculated device calibration $P_{d_c}(\nu)$:

$$\boxed{G_{d_e}(\nu) = \frac{P_d(\nu)}{P_{d_c}(\nu)} = \frac{P_b(\nu) + (K-1)P_{b_0}(\nu)}{KP_c(\nu)}}\,. \tag{4.10}$$

This last formula can be directly applied once we know the K ratio of the device under investigation. I recall that this ratio may be *under evaluated* from its real value, so the calculated gain may be over evaluated. Nevertheless this method should be closer to reality than the direct formula of equation (4.1).

4.4 Measurement procedure

Starting from now, we will only consider the bench composed of the 220 – 325 GHz electronic source, the cryostat and the bolometer for detection. An additional lock-in amplifier is used to measure small signals as well as to remove the ambient noise that may be detected by the bolometer. Finally, a computer

is used to control the whole experiment. The full bench is thus sketched in figure 4.27.

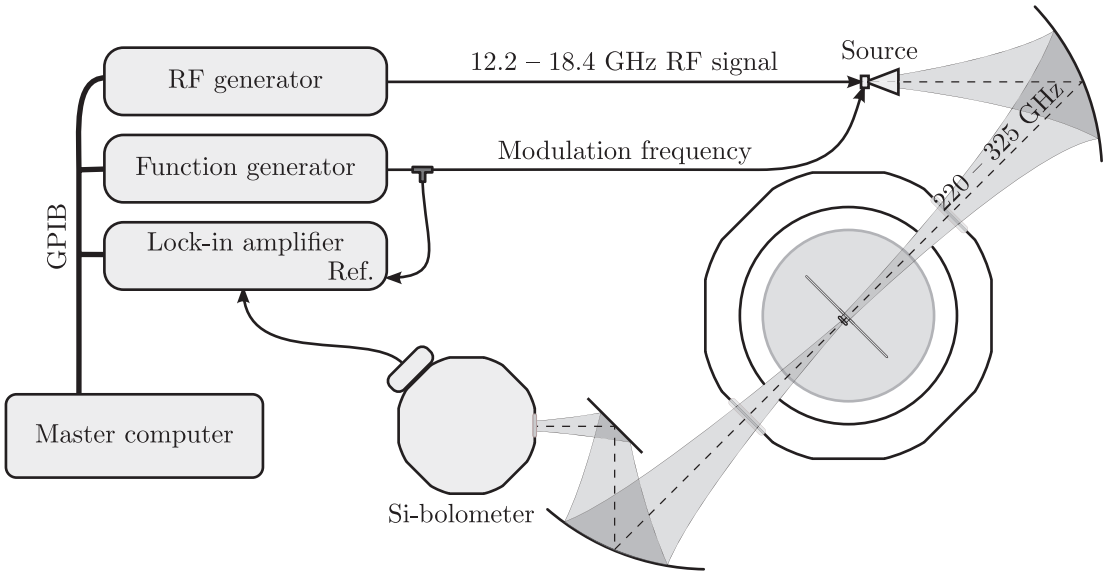

Figure 4.27: Full description of the bench as it will be used in the following experiments, mounted with the 220 – 325 GHz electronic source, a lock-in amplifier and the bolometer. A computer controls the whole experiment.

In the following sections, the LabView programs I realized to control the whole experimental setup will be described. Then, these programs will be used to measure the calibration of the bench.

4.4.1 Experiment control

Many different LabView programs have been made during my thesis to control various types of experiments. The main ones are described below:

Tera-Spectro This program, the most complicated one, was initially written to control the lasers and amplifier coupled with the photomixing device. This one was created the first because we had only this source at the beginning. The user has to choose either if he just want to reach a particular frequency, or measure a complete sweep on a frequency band. In both operating modes, the turn on and off of the lasers and amplifier are automatic. An audio signal is played to warn the people that they have to wear protective glasses since then. A complex algorithm then regulates the currents and temperatures of the two DFB lasers to reach the given beating frequency, and to equilibrate the power of the two laser wavelengths (to guarantee a good beating quality). This operation is fulfilled by using a PID[3] loop control on the temperature of one of the two lasers while an interlaced step by step loop regulates the current of both lasers to obtain the equilibrium between the two wavelengths. The measurement of the parameters (wavelengths and powers) needed for the control is achieved by using an OSA, as introduced in the setup of figure 4.16.
As far as the sweep experiment is concerned, the measurement of the transmitted signal is embedded in the program using the bolometer and the lock-in amplifier. In that configuration, the modulation of the beam is achieved by modulating the DC supply of the photomixing antenna.

3. The PID stands for a proportional, derivative, and integral corrector in the regulation loop.

The basic algorithm of this program is the following (see figure 4.28): after initializing the communications with the instruments and checking the input parameters of the user (in order to be sure that what he asks for is not impossible to achieve), the program switches on the lasers and enters a *for* loop on the frequency where it first reaches the value of frequency, then it performs the measurement, and finally stores the measurement and all the parameters of the lasers in a ASCII file. A new cycle with the next frequency then starts. When the loop is over the program automatically switches off the lasers and draws the most pertinent curves and send the files (curves and data) by email to the experimentalist. This allows to quickly know if the experiment went well. If the user chooses to use the other option to reach a particular frequency, the program only regulates the lesers to obtain the given frequency and wait until the user clicks on a *stop* button to turn off the lasers.
This program allowed to measure the transmission spectrum at room temperature of several samples such as PTFE or Silicon. The results will be presented in chapter 6.

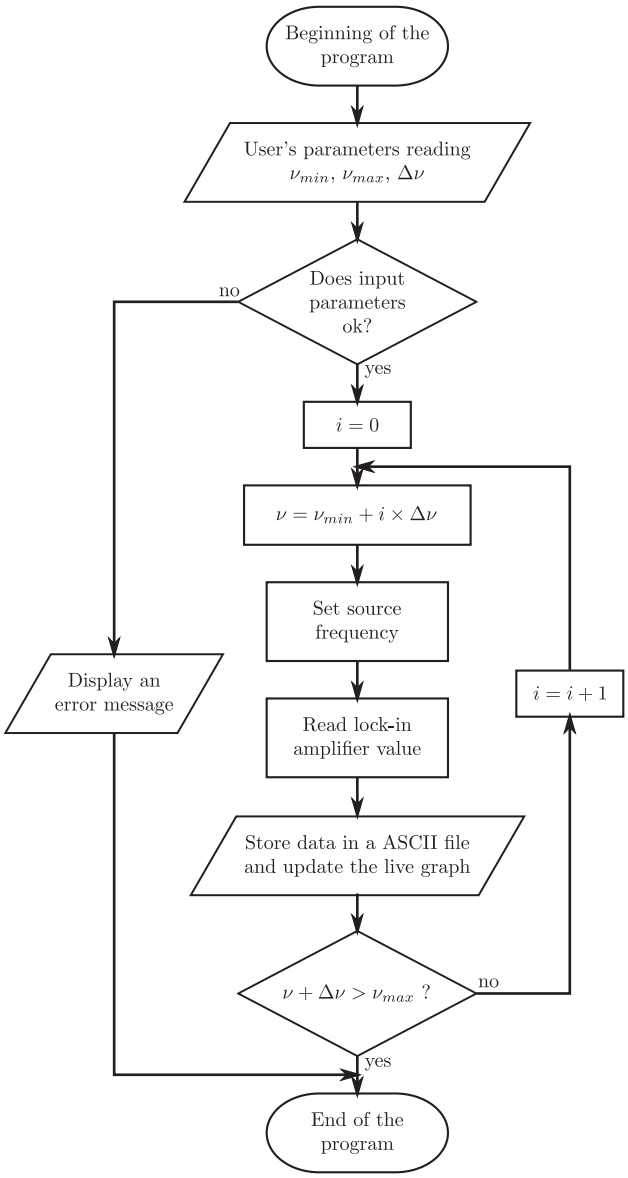

Figure 4.28: Simplified algorithm of operation of the *Tera-Spectro* and *Tera-Spectro*^{mini} programs.

Tera-Spectro^{mini} This second program allows to control the 220 – 325 GHz electronic source and the lock-in amplifier by automatically measuring the transmission spectra in that frequency range. The simplified algorithm of operation of this program is also sketched in figure 4.28. It is the same as for the *Tera-Spectro* program except that the change of the frequency is easier in this case. Indeed the only change to make is to set a different RF frequency delivered by the generator. Nevertheless, the program takes care to not change the frequency by big steps because, according to the manufacturer, this may create some problems to the source. As for the previous one, it also automatically switches on and off the source at the beginning and end of the experiment, respectively.

Tera-Spectro^{mini} with $I_d - V_d$ addon! This package provides an extension to the *Tera-Spectro^{mini}* program that is the ability to measure the current-voltage characteristics of the device under test for each frequency ruled in the upstream program. The utility of that package is to measure the frequency-dependent effect of the incident beam on those characteristics as well as to directly measure the effect on the transmitted signal measured by the bolometer as a function of the applied voltage on the device. A simplified algorithm is sketched in figure 4.30. This program should not be launched with a thin step of frequency since it generates a file by studied frequency, each one containing the current and the bolometer signal as a function of the applied voltage. If the considered device is a transistor, several gate voltages can also be swept to generate as much data. At the end of the execution of the loop, the program automatically draw 3D pictures showing the evolution of the bolometer signal and the current in the device under test as functions of the frequency and the applied voltage. The result is sent by email to the experimentalist in a compressed file. An example of the resulting curves generated can be seen in figure 4.29.

Tera-Spectro^{maxi}* and *Tera-Spectro^{maxi} with $I_d - V_d$ addon! These last two programs are identical to the ^{mini} programs adapted for the 0.843 – 1.100 THz electronic source. The orders sent to the RF generator and the conditions of test for good operation are among some of the changes made between the two versions. Unfortunately these programs have not been implemented on the complete bench due to lack of time.

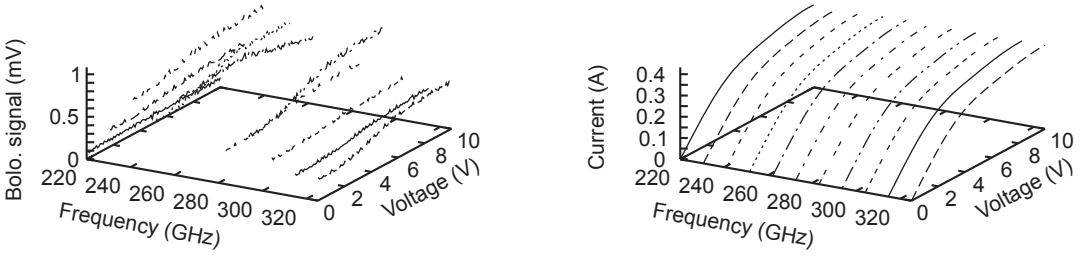

(a) Bolometer signal

(b) Current

Figure 4.29: Some results generated by the *Tera-Spectro^{mini} with $I_d - V_d$ addon!*. (a) and (b) respectively represents the bolometer signal and the current as functions of the frequency and the applied bias. The device under test is an interdigitated structure of the PTC465 sample of chapter 3.

4.4.2 Calibration

As discussed in section 4.3.3, a calibration of the whole bench without sample has to be performed in order to evaluate the gain of our devices. For that purpose, we installed in the cryostat the pierced

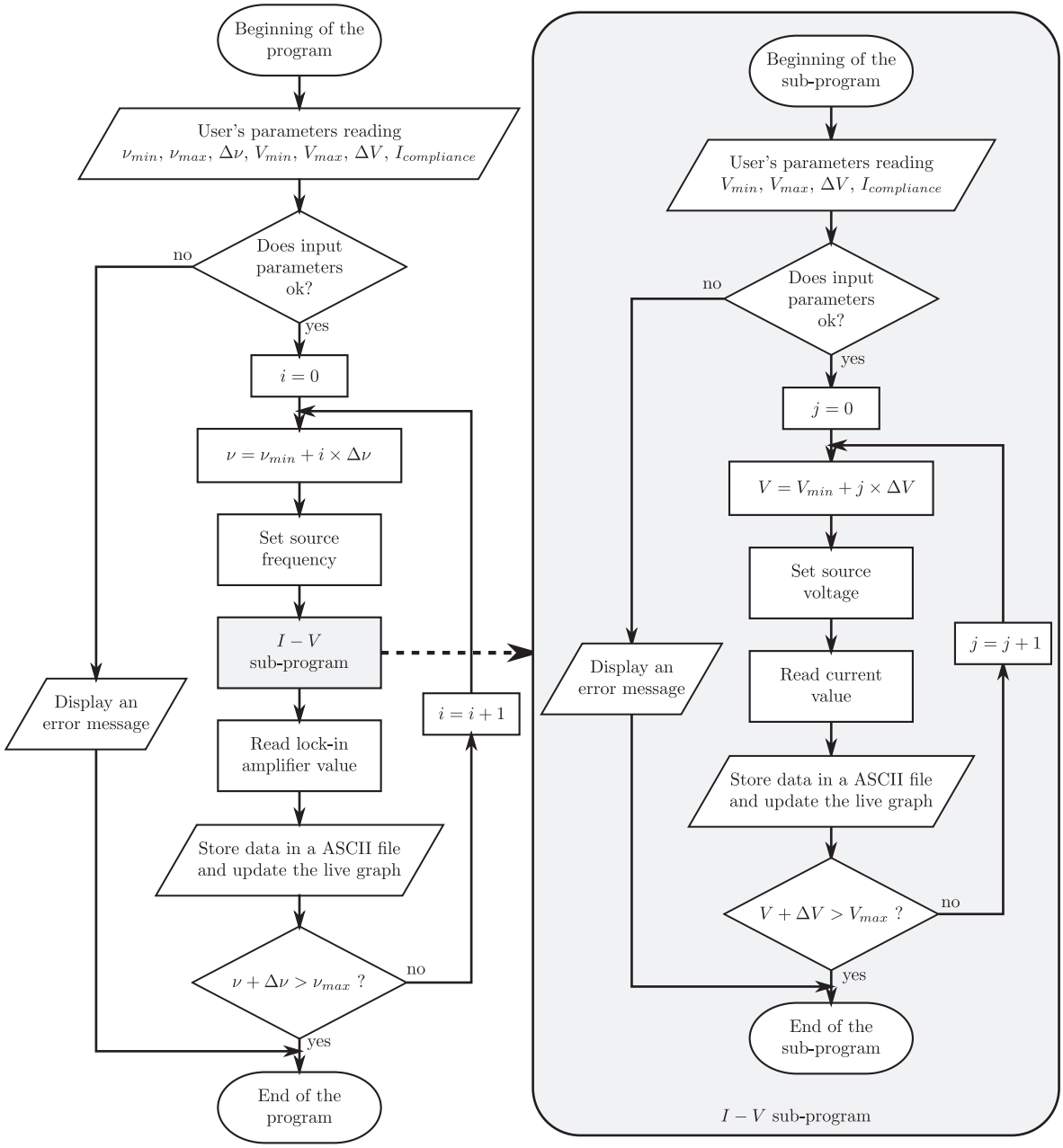

Figure 4.30: Simplified algorithm of operation of the *Tera-Spectro^{mini}, with $I_d - V_d$ measurement addon!*.

sample holder of figure 4.1(b), created the vacuum inside the cryostat, and measured the transmission spectrum $P_c(f)$. The result is shown in figure 4.31.

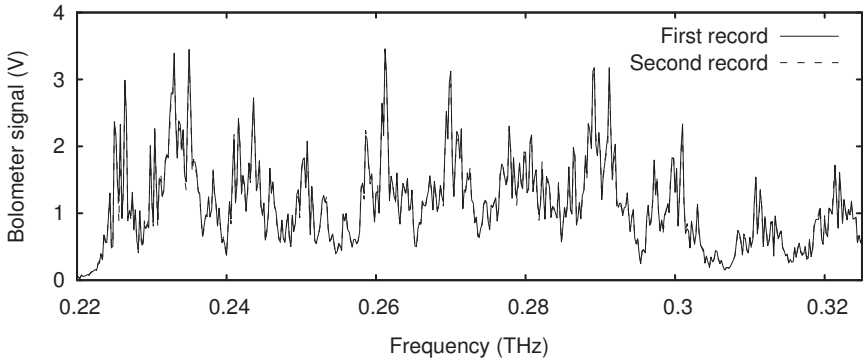

Figure 4.31: Calibration ($P_c(\nu)$) of the transmission setup mounted with the 220 – 325 GHz electronic source and the bolometer. Two different records are reported in the picture: they are superimposed.

We observe the main oscillating shape of the manufacturer curve of figure 4.6, with additional fluctuations. These fluctuations do not only come from the bench itself, but also from the source and detector. We initially measured the detected power by putting the bolometer directly in front of the source, these strong fluctuations were also present. However all these fluctuations are almost perfectly reproducible. This means that we should be able in principle to remove these perturbations from the final gain of the device with the help of equation (4.10).

Unfortunately, this technique does not work as well as we expected. In fact, the measurement of the transmission spectrum without and with a sample is very difficult to achieve in the same experimental conditions. The alignment of the bench is not modified between the two experiments but we have to remove the cryostat, open it and install the sample inside before putting back the cryostat. This manipulation inevitably creates a misalignment of the bench in the two conditions that affects the measured spectrum. As a consequence, to simplify our studies, we decided as a first step to evaluate the effect of the bias of the devices on the transmission (increasing or decreasing), and further calculate the gain. In that conditions, we will only have to measure the quantities $P_b(\nu)$ and $P_{b_0}(\nu)$ of section 4.3.3. Thus, we do not need to move the cryostat between the two experiments, and avoid the risks of misalignment between the two measurements.

4.5 Current-voltage measurements

Besides the above transmission experiments, two specific setups have been implemented to measure both continuous and pulsed current voltage characteristics of the samples installed in the cryostat. These setups are described in the following sections.

4.5.1 Continuous measurements

The continuous measurements are, of course, the easiest to achieve. For this experiment, we dispose of a continuous source-meter (Keithley 2602) able to apply a voltage or current and make a measurement on the same channel. In this case the algorithm of the program to automatically measure the current-voltage characteristics is quite simple. After checking the validity of the choices of the user ($V_{d_{min}}$, $V_{d_{max}}$, ΔV_d, $V_{g_{min}}$, $V_{g_{max}}$, ΔV_g, $I_{d_{max}}$, and $I_{g_{max}}$), two loops on both gate voltage (V_g) and drain-source voltage

(V_d) are executed, each time by measuring the drain current I_d. The limits in term of current ($I_{d_{max}}$, and $I_{g_{max}}$) set before are implemented into the source-meter which will guarantee to stay below these values. Finally, the measurement is stored into an ASCII file.

The only time parameter that is important to set in these experiments is the time to stay on each step of voltage. Indeed, the measurements produces some stairs of voltage as a function of time whose width can be adjusted. In our case, we decided to set this time to 5 ms. This time is long enough to avoid any parasitic transient effects that may occur in our devices, even if, when the devices are installed in the cryostat, the connexion wires are long.

4.5.2 Pulsed measurements

As far as the pulsed measurements are concerned, the procedure is different. The scheme of the setup is sketched in figure 4.32, where the samples are eventually installed into the cryostat. We do not dispose of an instrument able to directly apply a given pulse and in the mean time measure the current induced by the generated pulse. Moreover, the duration of the pulses that we have to apply needs to be short enough to avoid any self-heating effect in the device. We decided to use a pulse duration of 400 ns, with a repetition rate of 100 µs in the case of the GaN samples. To create that setup, I started from a function generator able to generate pulses down to 40 ns with an output impedance of 50 Ω (Agilent 33210A). Setting the generator in *high impedance* output mode allows to rule the voltage upstream to the 50 Ω resistance. This gives us access to the value of the generator itself ($V_{applied}$ in figure 4.32) without considering the output impedance of the generator. This trick will be useful to measure the current crossing our device by using this output impedance of the generator as a current measurement. In the mean time, an oscilloscope (Tektronix TDS2004B) is used to measure the effective voltage applied on the device (V_{ds} in figure 4.32). If the studied device is a transistor, the gate voltage can be adjusted using a DC supply [4]. The value of the current crossing the device (I_d in figure 4.32) is then extracted using the formula:

$$I_d(\mathrm{A}) = \frac{V_{applied}(\mathrm{V}) - V_{ds}(\mathrm{V})}{50} \tag{4.11}$$

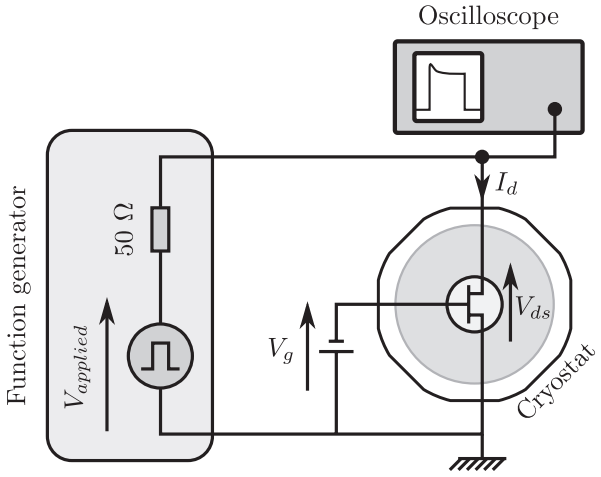

Figure 4.32: Illustration of the pulsed measurement setup.

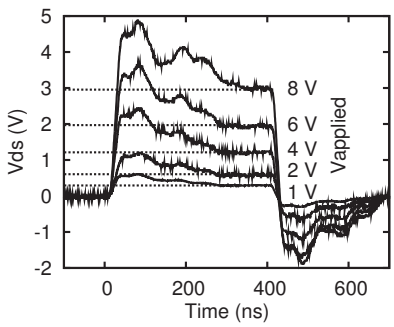

Figure 4.33: Example of pulses measured by the oscilloscope V_{ds} as a function of time. The $V_{applied}$ corresponding voltage for each pulse is reported..

4. We consider that in the case of HEMTs, the leakage current of the gate is sufficiently small to consider that no heating effect can be attributed to a continuous voltage applied on it.

An example of pulse shapes measured by the oscilloscope are reported in figure 4.33, for TLM samples installed in the cryostat and cooled down to a temperature of 15 K. The corresponding $V_{applied}$ voltage of each measurement is reported in the figure. The calculation of V_{ds} is performed by averaging the last part of the pulse, where it is fairly stable. Consequently, the situation reported in figure 4.33 represents the most limiting case in term of pulse duration since a shorter pulse may not present any stable part to extract a correct value of V_{ds}. The instabilities at the beginning of the pulses are mainly attributed to the long wires needed to route the source to the samples.

4.6 Summary

This chapter introduced the line of thought we followed to build the experimental setups needed for to investigate the GaN samples. The different configurations are tested and characterized:

- DC/pulsed current-voltage characteristics to measure the electrical parameters of the samples under study;
- transmission measurements in different frequency ranges with th help of different sources and detectors.

An experimental procedure is proposed, as well as some leads to calculate the effective gain of the devices. The experiments are automatized to the maximum by LabView programs specially created in the framework of this project to optimize the duration of the experiments which can last for several hours. This optimization is needed to ovoid an over consumption of cryogenic fluid during the experiments, specially when liquid helium is used, because of its high cost.

In the next part, the results obtained with these benches are presented, showing the effect of different parameters such as temperature, biasing conditions, sample geometry, etc.

Part III

Results

Chapter 5

Electrical characterization of the samples: DC & pulsed current-voltage characteristics from room to low temperatures



As detailed in section 4.5, two setups have been designed to measure the continuous and pulsed characteristics of the manufactured samples. This chapter will present the results issued from these original configurations.

5.1 Description of the different structures

The mask of the fabricated samples, already presented in figure 2.25 is composed of different structures having different roles. In particular, we will be more interested in the *transmission line model*, the *high electron mobility transistors*, and the *interdigitated fingers*. This choice is explained in the following description.

Transmission lines model (TLM): These devices are generally considered for electron transport characteristics measurements purpose. As it has been introduced in chapter 3, they allow to measure the contact access resistance as well as the sheet resistance of the quantum well of the grown samples. The fact that these devices are basically constituted by a simple n^+nn^+ structure is useful. Indeed, some Monte-Carlo simulations of such structures exist [Iniguez-de-la Torre 10]. We will use these results as a reference for investigation in the following work.

High electron mobility transistors (HEMT): AlGaN/GaN HEMTs are known to be promising candidates for applications such as high power, high frequency, and high temperature operation [Gaquiere 07, Kuzmik 02]. They show high transconductance, high cut-off frequencies and good thermal management [Kumar 03]. Since the actual background is poor on these structures, it is interesting to study them in order to compare with literature as well as to perform original measurements. In the following, L_g and L_{ds} will respectively stand for the gate and drain-source lengths.

Interdigitated fingers (IDF): The study of the devices specially fabricated for the amplification is important. It will allow to understand their operation, their limitations as well as their static performances. The latter point is important from the power supply point of view, because during the transmission experiments they will be used in static regime. In the following, L_s and L_l will respectively stand for the lengths of the shortest and longest regions of the interdigitated fingers.

5.2 Temperature dependence

The experimental setup introduced in section 4.5 allows to maintain the studied samples into three main temperature environments: 300, 77 and 7 K. It is thus possible to study, as a first step, the effect of the temperature on the current-voltage characteristics. This section summarizes the experimental results for the three kinds of structure.

5.2.1 Transmission lines model

The results of current-voltage characteristics measurements on TLM structures for different temperatures are summarized in figure 5.1. In the case of continuous measurements as well as pulsed ones, the lowering of the temperature involves a considerable increase in the current crossing the device. This means that the dynamic of the charge carriers is significantly affected by the cooling effect between 300 and 77 K, which is consistent with the increase of the mobility of the carriers at low temperatures. Between 77 and 7 K, the current has practically attained its maximum value and only a small increase is

measured. On the curves of figure 5.1(a), the increase of the current is limited by what we attribute to the self-heating effects starting to occur in the device. This is consistent with recent reports of HEMT-like structures [Lin 05, Parker 01]. The continuous curves show relatively lower values of the current, as expected by getting rid of the heating effects in the case of the pulsed measurements (figure 5.1(c)).

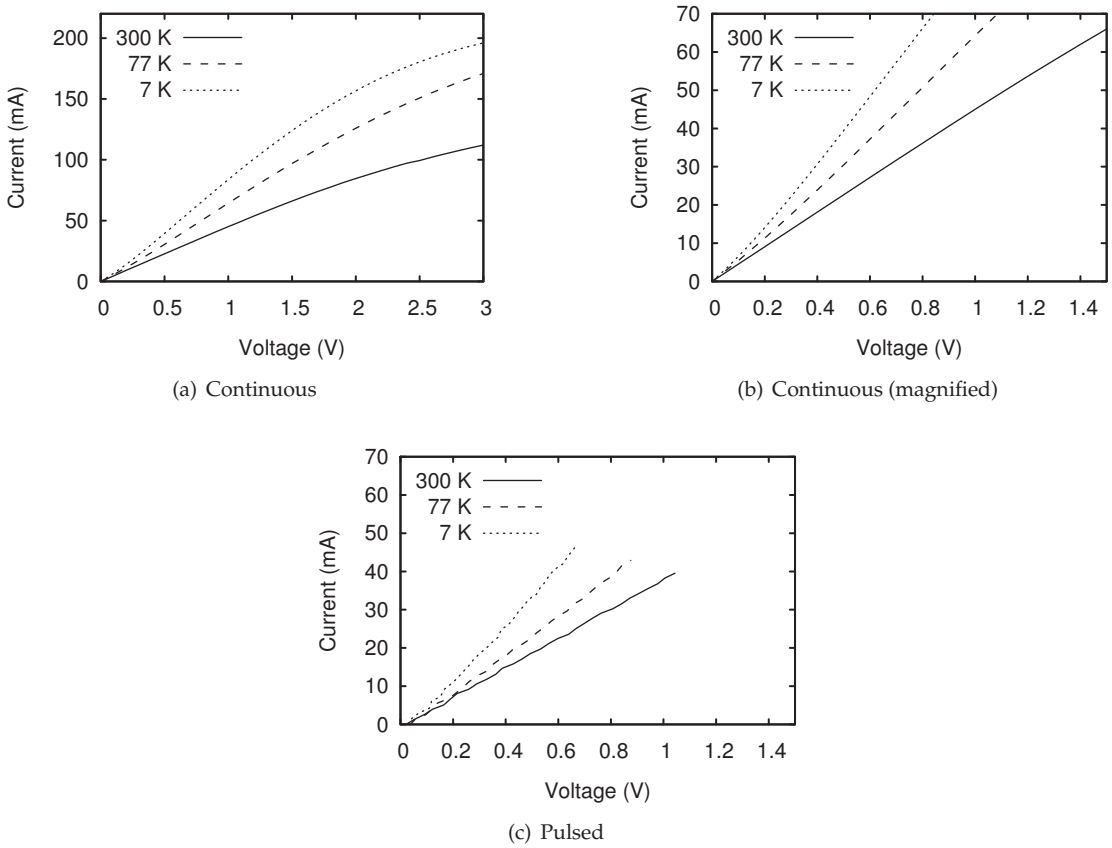

(a) Continuous

(b) Continuous (magnified)

(c) Pulsed

Figure 5.1: Continuous and pulsed (400 ns of pulse-duration) current-voltage characteristics of a TLM structures of 5 µm at 300, 77, and 7 K.

With these curves, the limits of the pulsed measurements are highlighted: compared to the DC ones, the pulsed results show less smoothed characteristics, due to the incertitudes on the current through the measurement method explained in section 4.5.2.

5.2.2 High electron mobility transistors

In the case of the HEMTs results are shown in figure 5.2: conclusions similar to the TLM results of section 5.2.1 can be drawn. The temperature affects the curves with an overall enhancement in the drain current no matter the applied gate voltage or the continuous/pulsed measurement technique are. The difference between the results at 77 and 7 K is negligible and reflects the same behavior than in the case of TLM structures. One can also clearly see the negative slope of the continuous curves for voltages above 3 V indicating the self-heating effects occurring in the devices [Lin 05]. As expected, this negative slope disappears in the case of the pulsed measurements.

Curves of figure 5.2 reproduce the well known output characteristics of GaN HEMTs, and the gate (varying from -1 to -3 V) effect on the drain current is observed.

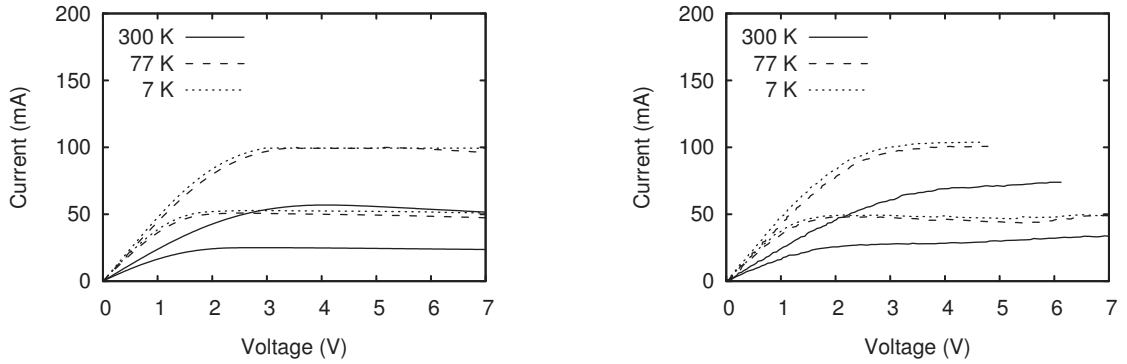

(a) Continuous (b) Pulsed

Figure 5.2: Continuous and pulsed (400 ns of pulse-duration) current-voltage characteristics of a HEMT structure with $L_{ds} = 15$ and $L_g = 3$ µm, at 300, 77, and 7 K. For each temperature, the lower and upper curves respectively correspond to a gate voltage of -3 and -1 V.

5.2.3 Interdigitated fingers

Again comparing the behavior evolution with the temperature of the current-voltage characteristics of the IDF structures, the lower the temperature, the higher the current crossing the device will be. Results for an IDF structure of 44 and 14 µm long in the active and passive regions, respectively, are shown in figure 5.3 for three different temperatures. In all cases, an ohmic behavior is shown.

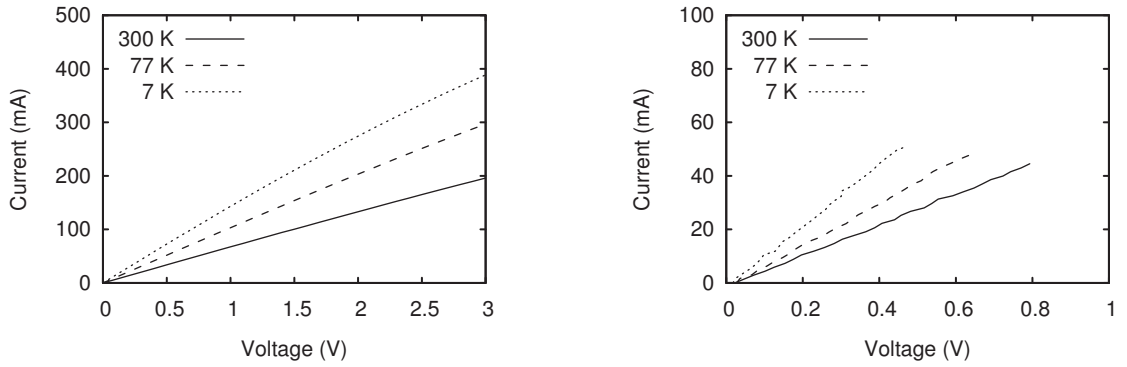

(a) Continuous (b) Pulsed

Figure 5.3: Continuous and pulsed (400 ns of pulse-duration) current-voltage characteristics of a IDF structure of $L_l = 44$ and $l_s = 14$ µm, and 4 µm of finger width, at 300, 77, and 7 K.

5.2.4 Discussion

It has been demonstrated with these measurements, that the pulsed measurements do not show the same negative slope that takes place in the DC curves at high voltages. This effect, the associated with self-heating, is particularly well known in the GaN-on-sapphire devices because of the poor thermal conductivity of sapphire [McCarthy 52]. When the current crossing the device is increased, the resulting heating is hardly evacuated through the substrate to the sample holder. This results in an overheat of the conductive channel, thus degrading the transport properties of electrons. When the pulsed

measurements are performed, the time ratio between the conduction and resting times is enough to take rid of these effects. As a consequence, the current does not present this negative slope anymore, and the curves are released of the self-heating effects.

5.3 Geometry dependence

The studied devices have been realized with different geometrical parameters that have been introduced in chapter 3. Here we present the evolution of the current-voltage characteristics with these parameters.

5.3.1 Transmission lines model

We recall that the TLM devices are made up of two ohmic contacts over the quantum well. Their width are constant but the distances between contacts are different. Whilst, on our mask, the distance between contacts are of 5, 10, 20, 30, and 40 µm, the width of the devices is 150 µm. The comparison of devices of 5, 10, and 20 µm long at room temperature is drawn in figure 5.4.

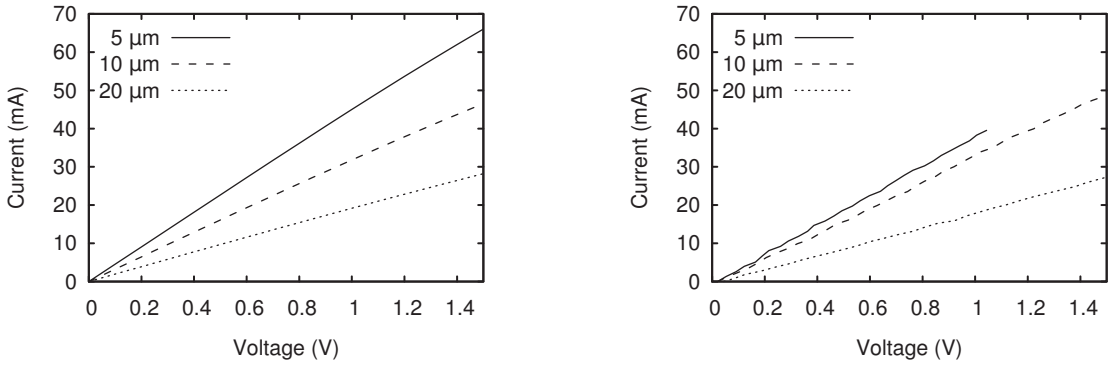

(a) Continuous (b) Pulsed

Figure 5.4: Continuous and pulsed (400 ns of pulse-duration) current-voltage characteristics of TLM structures of 5, 10 and 20 µm, at 300 K.

As expected, the shortest the device the higher the current is because of the smaller resistance. Indeed, if we consider the TLM structure as a resistance made-up of a GaN quantum well channel, the relation $R = R_S \frac{L_{TLM}}{W_{QW}}$, where R_S is the sheet resistance of the channel, L_{TLM} is the TLM length, and W_{QW} the width of the device, roughly evaluates the equivalent resistance of the device, that is the reciprocal slope of the curves. The same trend of increasing current by shortening the device length appears in the pulsed measurements. The 5 µm long device seems to present a lower current increasing compare to the continuous measurement. As this effect is not observed in longer devices, this effect is attributed to a degradation of the device or of the quality of the contacts between the measurements.

5.3.2 High electron mobility transistors

The characteristics for HEMTs with three different drain-source lengths are given in figure 5.5. The studied devices have $L_g = 4$ µm and $L_{ds} = 8$, 12, and 16 µm. Their width of 150 µm is the same for all the devices. As for the TLM structures, an increase in the drain current is found with the decrease

of the drain-source length. The self-heating, discussed in section 5.2.4 produces a higher effect on the shorter devices which is consistent with the fact that the current is increased in the case of the smaller geometries.

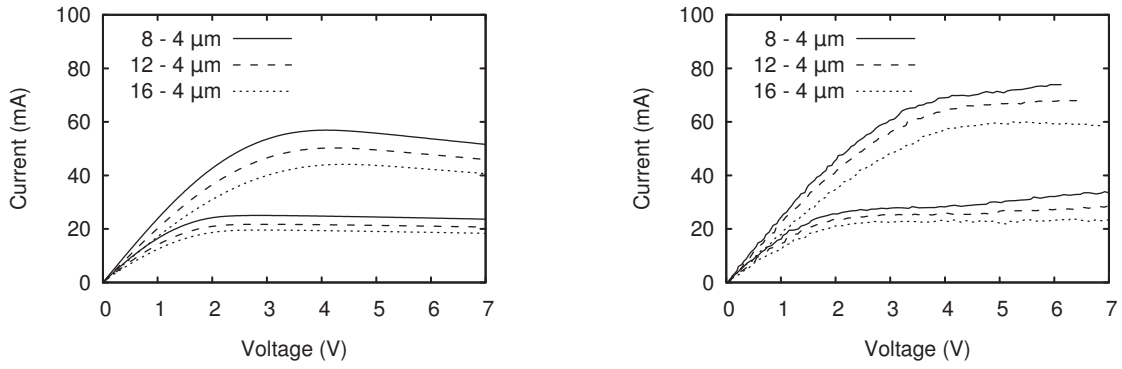

(a) Continuous (b) Pulsed

Figure 5.5: Continuous and pulsed (400 ns of pulse-duration) current-voltage characteristics of HEMTs with $L_{ds} = 8$, 12 and 16 µm, and $L_g = 4$ µm, at 300 K. For each device, the upper and lower curves respectively correspond to a gate voltage of -1 and -3 V.

Comparing the continuous with the pulsed measurements, we note that an effect can be detected at high voltages on the latter one which is absent on the continuous ones. At high voltage in the saturation regime, the current resumes its growing behavior in the case of pulsed measurements. This is observed on the three different structures. This effect has been already investigated in the literature and has been attributed in some cases to impact ionization occurring in the channel [Ernst 97, Suemitsu 98, Parker 01], and in other cases to the presence of traps in the structure [Fathallah 10]. The detection of this effect only occurs in the case of the pulsed measurements, because in the case of the continuous measurements, the effect of impact ionization is compensated by trapping effects: some electrons are trapped in sites outside the channel, thus creating an additional built-in potential which acts like a gate for the remaining electrons in the channel [Parker 01].

5.3.3 Interdigitated fingers

In the case of IDFs, figure 5.6 summarizes the effect of the different geometries fabricated on the mask. Three different structures are reported with $L_l = 39$, 44, and 52 µm and $L_s = 19$, 14, and 6 µm respectively. The curves seems almost perfectly superimposed, but, by carefully analyzing the curves, the more the device is asymmetric, the higher is the current. This result can be interpreted as follows: if L_A, L_P, and L_T are respectively the length of the active and passive zones and the sum of these two lengths, they are related, no matter the considered device, by the relation:

$$\begin{cases} L_A = x \times L_T \\ L_P = (1 - x) \times L_T \end{cases} \tag{5.1}$$

where x is a real number between 0 and 1. The length L_T being constant over all the devices (refer to table 3.3 page 55), all of the IDFs can be defined by the *asymmetry factor* x, representing the asymmetry of the considered device. The equivalent resistances of an active or passive zone can be defined as for the

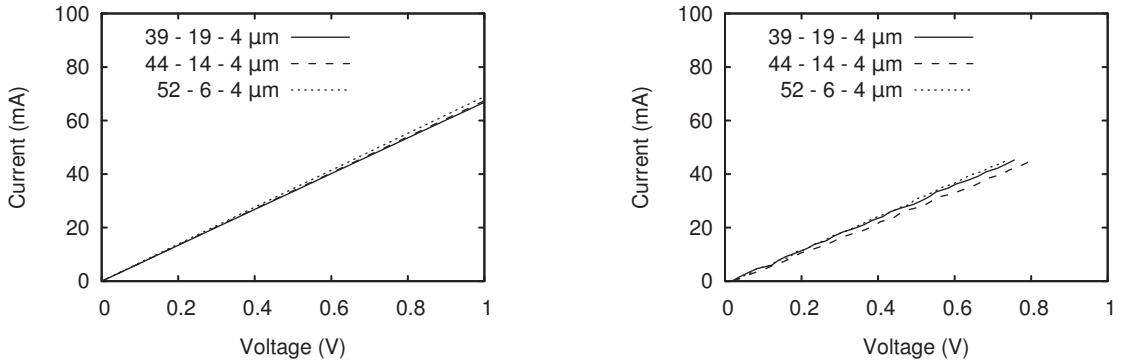

(a) Continuous (b) Pulsed

Figure 5.6: Continuous and pulsed (400 ns of pulse-duration) current-voltage characteristics of IDF structures with three different geometries, at 300 K. The three numbers in the titles of the curves indicates L_l, L_s, and the width of the fingers, respectively.

TLM structure by:

$$\begin{cases} R_A = R_S \frac{L_A}{W_{QW}} = R_S \frac{xL_T}{W_{QW}} \\ R_P = R_S \frac{L_P}{W_{QW}} = R_S \frac{(1-x)L_T}{W_{QW}} \end{cases} , \tag{5.2}$$

where R_S is the sheet resistance of the quantum well (see table 3.6 page 60) and W_{QW} is the width of the quantum well (length **G-F** in figure 3.4 page 55). For a given structure, there are 8 fingers on each contact: they generate 8 active and 7 passive zones, all being electrically connected in parallel. Thus, the total resistance of the structure is:

$$R_T = \left(\frac{R_A}{8}\right) // \left(\frac{R_P}{7}\right) . \tag{5.3}$$

Finally, the x dependence of R_T is given by the relation:

$$R_T = \frac{R_S L_T}{W_{QW}} \frac{x(1-x)}{8-x} . \tag{5.4}$$

This dependence is drawn in figure 5.7. It is obvious that the asymmetry of the structure involves different electrical behavior from source point of view.

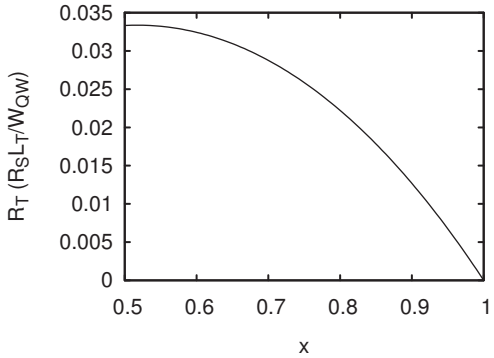

Figure 5.7: IDF global resistance as a function of the asymmetry factor x. The resistance is normalized to $\frac{R_S L_T}{W_{QW}}$.

In the case of the three structures of figure 5.6, the asymmetry factor is 0.93, 0.76, and 0.67, the length between fingers is $L_T = 58$ µm and the width of the quantum well is $W_{QW} = 492$ µm. This means that for these devices the theoretical channel resistance alone (i.e. without access resistance) is 0.31, 0.84, and 1.01 Ω. However, the measurements presented in figure 5.6 show a resistance of the order of 15 Ω: therefore, the remaining part of the resistance must be related to the access resistances of the contacts.

In conclusion, a very special care have to be paid to this effect because the major part of the applied voltage on the IDF structure will be spread over the contacts whilst less than 10 % will effectively be applied on the channel itself. The worst case being for the more asymmetrical structures whose channel resistance is smaller. For example, if 1 V is applied on an IDF with an asymmetry factor of 0.67, then 0.93 V will be spread over the contact layers and only 0.07 V on the channel. As a consequence, the value of electric field in the channel of the active (passive) zones cannot be simply calculated by the ratio of the applied voltage by the length of the active (passive) zone.

5.3.4 Optimization of the devices proposal

In the previous sections, we have analyzed some limitations of our interdigitated structures. Indeed, it is shown that the main part of the voltage is spread over the contact resistances, which are more than 10 times higher than the channel resistance. For example, if we want to apply an electric field of 1 kV/cm in a 50 µm long channel, the voltage to apply on the channel alone, is 5 V. However, by taking into account the access resistances, the total applied voltage will be more than 50 V. This voltage value is very high and may lead to the device break down.

It is thus important to find a solution to this issue. Firstly, technologically speaking it may be possible to decrease the access resistances, even if it will not completely solve the problem. This first point may be done by increasing the thickness of metal layers on the contacts. Another solution is to increase the channel resistance compared to the contacts: this will decrease the ratio between the electric fields in the contacts and the channel. To achieve that goal, two possibilities can be foreseen:

– increase the lengths of the zones between contacts;
– decrease the width of the fingers.

Whilst the former solution does not imply a change of the total surface of the sample (less fingers can be used in the structure), the latter one involves several changes in the structure to obtain the same area. A possible solution, proposed in figure 5.8, is to add intermediate bridge contacts to artificially decrease the width of each zone.

5.4 Pulse duration dependence

We measured the effect of the pulse duration on the current voltage characteristics of the HEMT. The result is shown in figure 5.9 for a transistor with $L_{ds} = 8$ and $L_g = 4$ µm. For the two gate voltages (-1 and -3 V) the shortest the pulse width, the higher the current. The kink effect due to impact ionization (as discussed in section 5.3.2) is enhanced in the case of the smaller pulse width. This is consistent with the results described in [Parker 01] showing that impact ionization becomes more and more important in the measurement as the pulse width decreases.

The heating effects occurring in the continuous measurements is here clearly visible. For voltages above 2 V, the continuous curves present less current than in the pulsed regimes, testifying the degradation of electrons transport in the channel, as described in section 5.2.4.

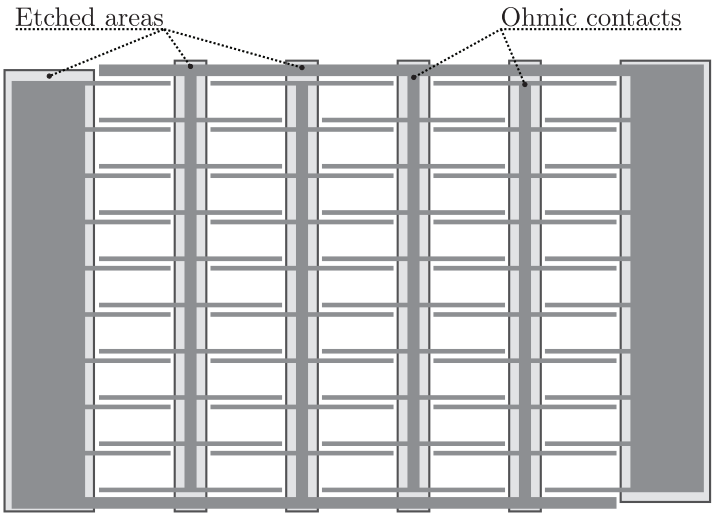

Figure 5.8: New interdigitated fingers pattern proposal. The light gray areas are etched to avoid conduction between the fingers tips and opposite contacts.

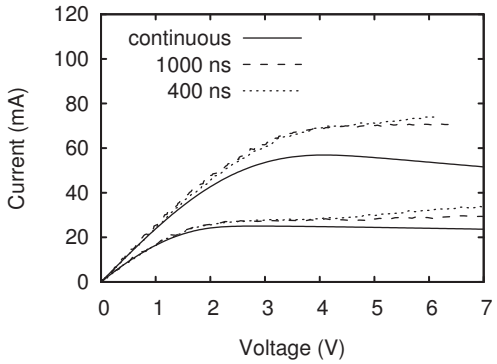

Figure 5.9: Output characteristics at room temperature of a HEMT with $L_{ds} = 8$ and $L_g = 4$ µm, measured in continuous and pulsed regimes, with a pulse duration of 1000 and 400 ns. The top and bottom curves respectively correspond to a gate voltage of -1 and -3 V.

5.5 OPTTR investigation

It has been demonstrated using Monte-Carlo simulations that when the plasma frequency f_P is close to the inverse of the time interval between two successive optical phonon emissions (see figure 2.7 page 36), important current oscillations at the frequency of the cyclic movement due to OPTTR may appear in the device [Iniguez-de-la Torre 10]. The observed phenomenon is highly temperature dependent, and, as the temperature raises, the cyclic movement of electrons becomes more and more chaotic (as already illustrated in figures 2.8(a) and 2.8(b) page 38).

The group of Salamanca University also demonstrated that the current-voltage characteristics of GaN based n^+nn^+ diodes at low temperatures presents some marks associated with the activation of the OPTTR mechanism in the device (figure 5.10(a)). The signatures of the kinks are related to the values of voltage where they appear in the characteristics. When the value of voltage is enough for the electron to reach the energy needed to emit an optical phonon, there is a first kink testifying the loss of energy of electrons. The corresponding value of voltage is easy to evaluate: as the optical phonon energy value in GaN is 91.2 meV, the first kink will occur at 91.2 mV. This voltage is needed to increase electron energy

of electrons along the channel to the value of the optical phonon energy, no matter the geometry of the device. Other kinks will occur at integer multiplied values of the first kink voltage, when electrons can undergo multiple emissions of optical phonons along their travel in the channel. This result is illustrated in figure 5.10, extracted from [Iniguez-de-la Torre 10].

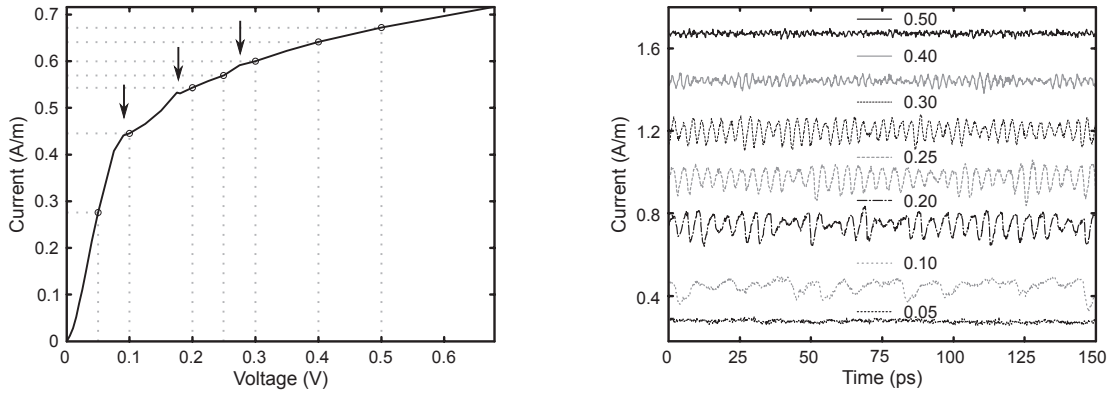

(a) Current-voltage characteristic

(b) Current time evolution

Figure 5.10: Monte-Carlo simulation of a n^+nn^+ bulk GaN diode showing the effect of OPTTR mechanism on the current-voltage characteristic (a), and the time evolution of the current for different applied voltages (b). In order to improve the readability of (b), the curves are vertically shifted by 0.2 A/m each, starting from the one corresponding to 0.2 V. The arrows of (a) indicates the visible kinks due to OPTTR occurring in the device. Pictures extracted from [Iniguez-de-la Torre 10].

We thus decided to investigate the closest devices we have from the results presented in [Iniguez-de-la Torre 10]. Their devices, made-up of bulk GaN n^+nn^+ diodes are close to our TLM structures already presented, except for the fact that they studied a bulk structure, while our channel is composed of a quantum well of GaN material. Anyway, since the value of the optical phonon energy is the same in both cases, the results should be similar. As for the results of figure 5.10(a), the voltages range of study must be in accordance with the optical phonon energy value. In the case of our GaN devices, this value is 91.2 meV, which correspond to a first kink appearance near 91.2 mV. We present here the results investigating with continuous measurements the TLM structures maintained at low temperatures in the 0 – 0.5 V voltage range. Note that our pulsed setup is not enough accurate to investigate such a small effect, which might be masked by measurement fluctuations. The results are presented in the figures 5.11, 5.13, and 5.14 (for 5, 10, and 20 µm long TLM structures, respectively), showing the continuous measurements and its derivative to emphasize the current variations.

Even if no significant effect can be detected on the continuous curves, the derivative function of the data highlights some singular points. In the curves at low temperatures (figures 5.11(a), 5.12(a), 5.13(a), and 5.14(a)) there is a clear effect occurring around the value of 0.1 V, which is close to the first simulated OPTTR appearance as mentioned before in figure 5.10(a).This effect may be considered as one of the first reported evidence of the occurrence of the OPTTR mechanism. The same effect is detected on most of the devices at 77 K, but is less pronounced. Nothing can be detected at room temperature. This effect clearer as the device length is shorter, which can be explained with the parasitic interactions undergone by electrons during their travel in the channel that becomes more and more important as the length of the device increases.

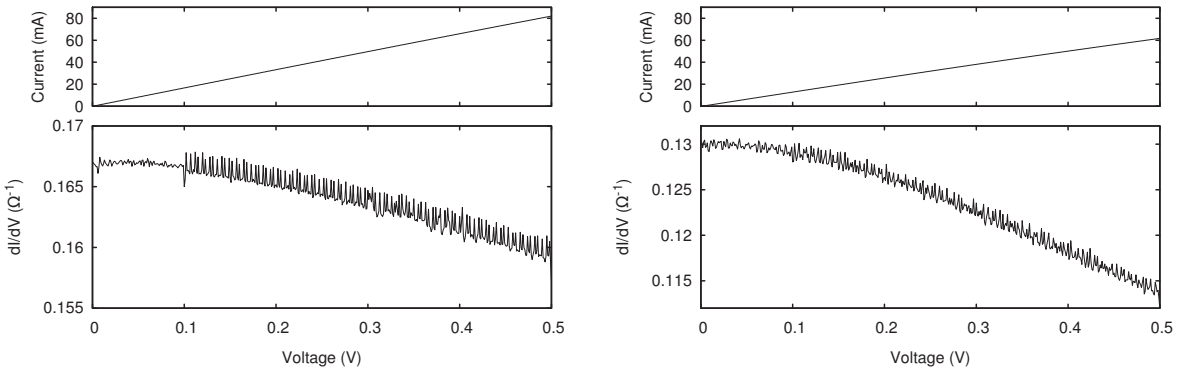

(a) 7 K (b) 77 K

Figure 5.11: Current-voltage characteristics and its derivative for a 5 µm long TLM structure maintained at 7 K (a) and 77 K (b).

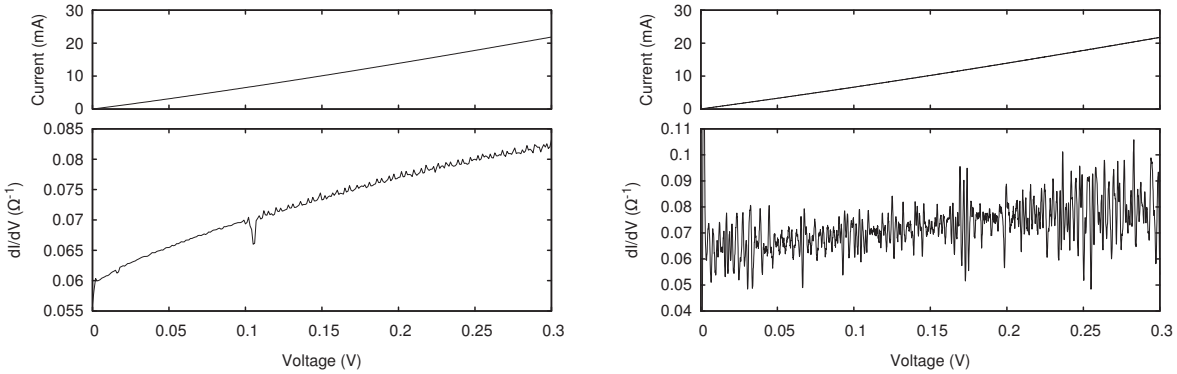

(a) 7 K (b) 77 K

Figure 5.12: Current-voltage characteristics and its derivative for a 5 µm long TLM structure maintained at 7 K (a) and 77 K (b).

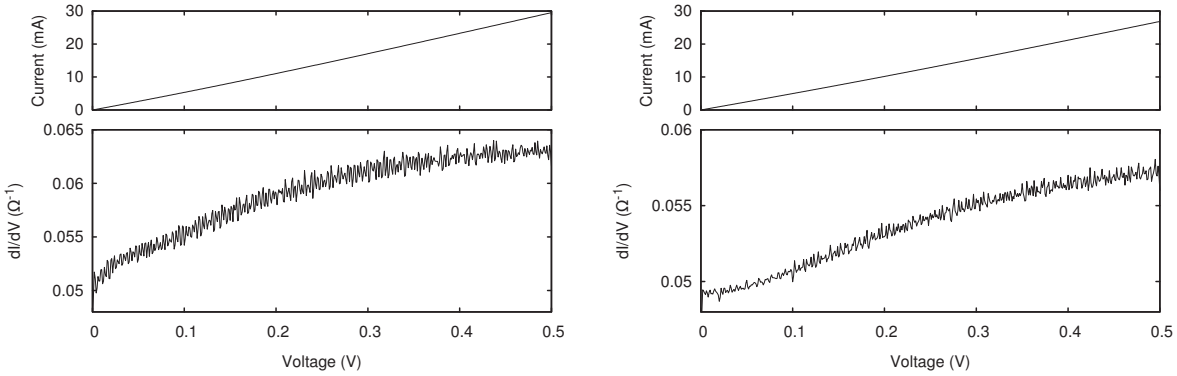

(a) 7 K (b) 77 K

Figure 5.13: Current-voltage characteristics and its derivative for a 10 µm long TLM structure maintained at 7 K (a) and 77 K (b).

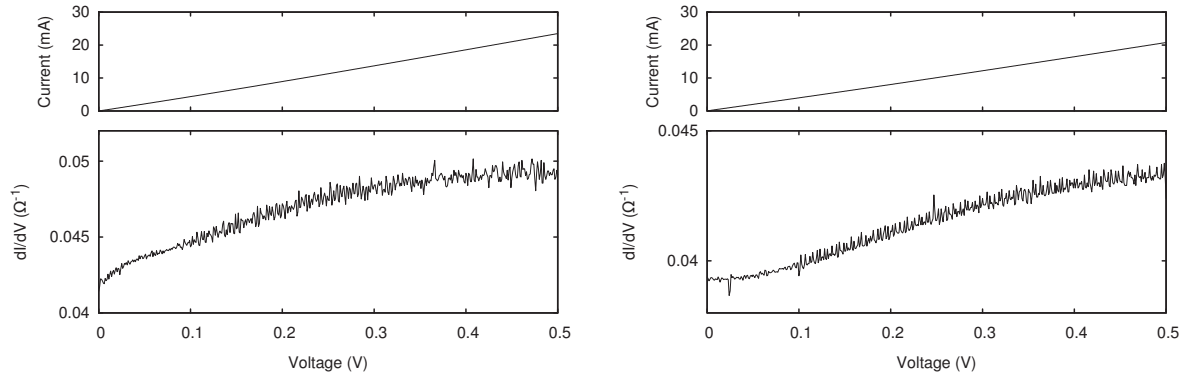

(a) 7 K (b) 77 K

Figure 5.14: Current-voltage characteristics and its derivative for a 20 µm long TLM structure maintained at 7 K (a) and 77 K (b).

5.6 Summary

In this chapter, we have presented the results of continuous and pulsed measurements performed on different GaN devices. The effect of different parameters such as temperature, geometry of the devices and pulse duration (for pulsed measurements) have been highlighted. These characteristics have been analyzed and interpreted in terms of the main physical mechanisms such as self-heating of the samples, mobility variation, impact ionization, etc. In the last section, an original result is found by investigating the smallest devices when compared with the results of Monte-Carlo simulations [Iniguez-de-la Torre 10]. A kink detectable in the derivative of the current-voltage characteristics occurs at voltages near 0.1 V which corresponds to the energy of the optical phonon in GaN. To our knowledge, this represents the first proof of the onset of the OPTTR mechanism found in nitride-based structures.

Chapter 6

Experimental investigation of terahertz transmission



This chapter summarizes the results obtained with the spectroscopic benches described in chapter 4. The first section deals with the use of the photomixing source as an emitter and the bolometer for the detection. This experiment were only performed at room temperature and the experiment conditions are described in section 6.1.1. The second section deals with the results obtained to date with the complete bench (cryostat included) mounted with the 0.220 – 0.325 THz electronic source.

6.1 Room temperature passive measurements with the photomixing bench

The first experiments performed in the framework of this thesis were done using the photomixing source described in section 4.2.1.2. The frequency range covered by this source is from 0.75 up to 1.9 THz. In a first time, a short description of the experiment and data processing is given. Then the results are described in the case of the samples of chapter 3. Finally, results obtained for other kinds of samples, tested to compare with what already exists in the literature, are introduced.

6.1.1 About the experiment and data processing

The photomixing experiments were the first choice for spectroscopic measurements because of the large tunability of the THz beam, its good spectral selectivity, and its ability to work at room temperature. Even if the full experiment with heterodyne detection – as sketched in figure 4.16 – has not been completed due to optical alignments difficulties of the antenna and built-in lens, the setup including the source alone with the Si-bolometer as a detector worked well. The route of the beam on the setup is limited to the minimum since the power of the source is very low ($\approx -50dBm$). We thus used two parabolic mirrors of focal length 7.5 cm to collimate the beam issued from the source in a sufficient volume to be able to introduce some samples, and to focus it on the bolometer. This experiment is sketched in figure 6.1: the sample under investigation is maintained in the collimated part of the beam. This solution is easier to align compared to the solution of figure 4.18 since the distance between the two mirrors (the collimated part of the beam) is not critical. A lock-in amplifier is used to extract the part of

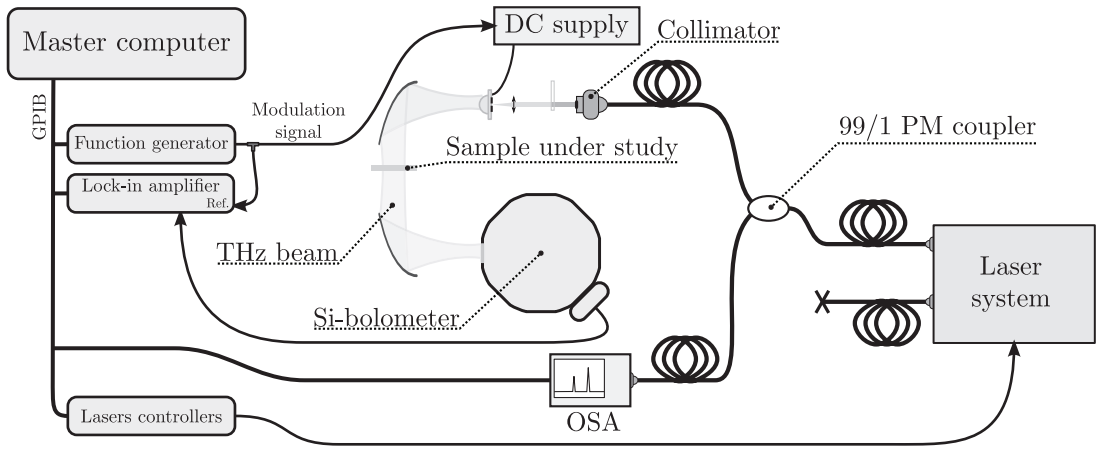

Figure 6.1: Experimental configuration of the measurements performed using the photomixer and bolometer at room temperature. The devices under study are placed in the collimated beam.

the bolometer signal issued from the source. For that purpose, the DC supply of the source is modulated

by a square signal of 37 Hz (frequency chosen in accordance with the band-width of the bolometer). The diameter of the collimated beam is of the order of the diameter aperture of the parabolic mirrors (that is ≈ 5 cm). This implies to use wide samples to avoid diffraction effects. Finally, the whole experiment is controlled by a computer running the *Tera-Spectro* program, described in section 4.4.1.

Concerning the data processing, we performed a calibration spectrum $P_c(\nu)$ without sample before measuring the spectrum $P(\nu)$ with a sample installed in the THz beam. The frequency points of the two spectra does not exactly match due to the instability of the laser system involving a non-perfect repeatability of the frequencies. The transmission spectrum (gain) of the studied sample $G(\nu_j)$ is thus calculated by the ratio of $P(\nu_j)$ by a linear approximation of the calibration at the same frequency point ν_j:

$$G(\nu_j) = \frac{P(\nu_j)}{P_c(\nu_{c_{j-1}}) + \frac{P_c(\nu_{c_{j+1}}) - P_c(\nu_{c_{j-1}})}{\nu_{c_{j+1}} - \nu_{c_{j-1}}}(\nu_j - \nu_{c_{j-1}})}\,, \tag{6.1}$$

where ν_{c_j} and ν_j are respectively the frequency values of the calibration and measurement with a sample spectra for the jth measurement.

This procedure is justified by the fact that all the beam surface crosses the sample, by opposition to the calculation of section 4.3.3, where we consider that only a part of the beam passes through the device under study. This is true assuming that the sample introduced in the beam does not generate any misalignment of the beam compared to the case without sample. We will see in the results of sections 6.1.2 and 6.1.3 that this latter point is not always fulfilled and generates an artificial lowering of the calculated transmission.

We tested four different samples that are a wafer of the GaN samples of chapter 3, a 450 µm thick GaAs non-conductive substrate, a 5 mm thick plate of polytetrafluoroethylene (PTFE, best known as Teflon®), and a 20×100 µm stack of polyethylen (PE) sheets. The results are presented in the following sections.

6.1.2 GaN over sapphire sample

The most interesting sample to investigate in our study is of course the GaN samples specially grown in the framework of this project. We thus placed an uncut piece of wafer with the GaN structures grown on it in the THz beam of the bench. The result of the transmission measurement after data processing using equation (6.1) calculation is shown in figure 6.2.

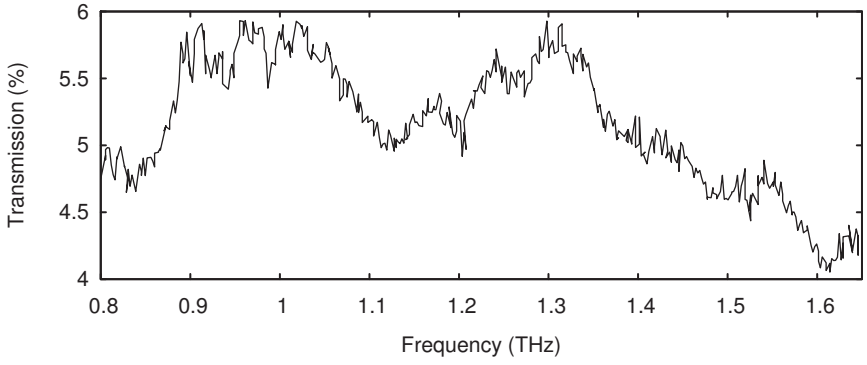

Figure 6.2: Transmission spectrum of a GaN over sapphire sample (see chapter 3 for details).

Overall, the variations of the transmission coefficient are of the order of ± 20 % on the whole

investigated frequency band. This result is not in agreement with that of [Ferguson 01] ($\approx$ 5 % of transmission on the investigated band), where similar sample exhibit a transmission of the order of 30 % in this part of the electromagnetic spectrum. We suspect the sample to introduce a misalignment on the transmitted beam which results in a lowering of the detected signal on the bolometer. This loss in the calculated transmission is also found on the PTFE sample, as we will see in section 6.1.3.1. Anyway, the results should be qualitatively good, as the results of section 6.1.3.1 will demonstrate, by comparing with existing results.

6.1.3 Investigation of other samples

Several other samples have been investigated to increase our knowledge of the photomixing bench. Here the results obtained with these samples are presented.

6.1.3.1 Teflon (PTFE)

The result shown in figure 6.3 is obtained by introducing a 5 mm thick plate of PTFE in the THz beam of the photomixing bench. The obtained transmission is compared to a result reported by the RIKEN Laboratory in [RIKEN 10] for a 30 µm sheet of the same material with a time-domain spectroscopy experiment. The latter result is divided by 10 to obtain a transmission coefficient near our results and thus improve the clarity of the curves.

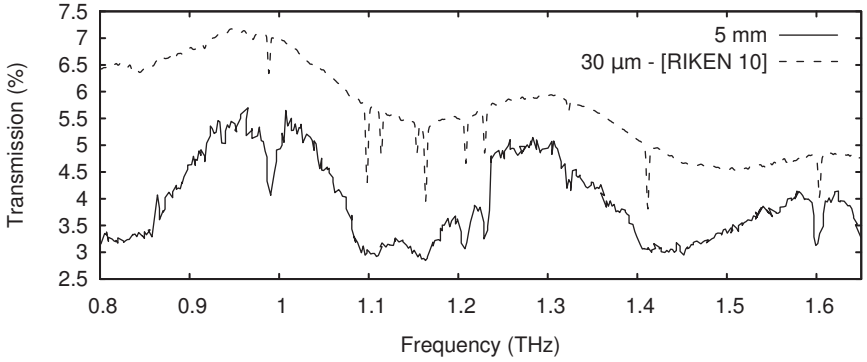

Figure 6.3: Transmission spectrum of a 5 mm thick PTFE sample compared with the results divided by 10 obtain in [RIKEN 10].

It is shown that the result obtained with our bench is qualitatively very close to the results obtained by the Japanese laboratory. Indeed, the main oscillating shape as well as the absorption peaks are detected at the same frequencies as RIKEN's results. These absorption peaks are related to the material constituents absorbing the incident phonons matching their energy gap. However, there is quantitatively a big difference between the two spectra. This effect can be attributed to different reasons:

– Concerning the RIKEN's results, if we evaluate the absorption coefficient γ_R resulting from their results (for example at 1 THz, a transmission of 65 %), we find:

$$\gamma_R(1\ \text{THz}) = -\frac{\ln(0.65)}{30 \times 10^{-6}} = 1.4 \times 10^4\ \text{m}^{-1}\ . \tag{6.2}$$

If we apply this coefficient to our sample thickness, we find a transmission value of:

$$G(1\ \text{THz}) = e^{-\gamma_R(1\ \text{THz})L} = 4 \times 10^{-29}\ \%\ . \tag{6.3}$$

This implies that the RIKEN's value is not applicable to our case. In fact, if one looks in the literature, he will find that the absorption coefficient strongly depends on the thickness of the studied sample. To better clarify this point we have summarized in figure 6.4, existing absorption coefficients as functions of the thickness of the sample. As a general trend, the measured absorption coefficients is strongly dependent on the thickness of the sample. It is thus clear that the absorption

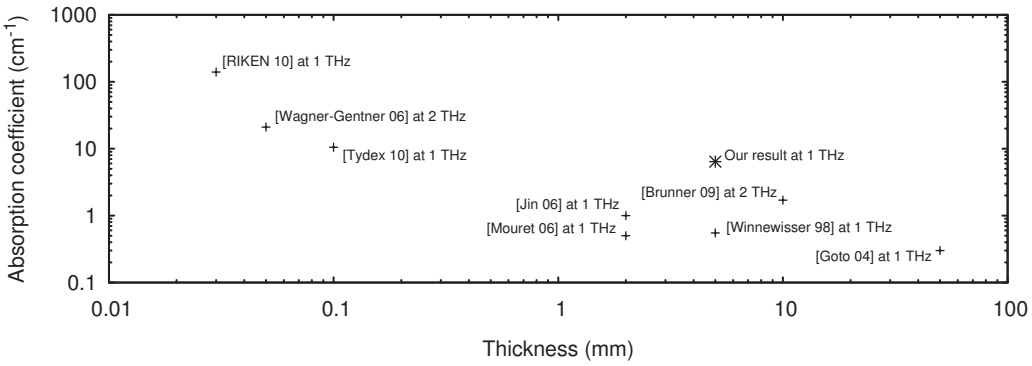

Figure 6.4: Absorption coefficient of PTFE as a function of the thickness of the studied sample, as found in the literature [Brunner 09, Wagner-Gentner 06, Mouret 06, Goto 04, Winnewisser 98, Tydex 10, RIKEN 10, Jin 06], compared with our study.

coefficient adapted to our case should be taken from experiments performed with thick samples, for example [Brunner 09, Winnewisser 98].

– Even if the results of [RIKEN 10] cannot be applied to our experiment, the calculation of the absorption coefficient with our data (see 'Our result' in figure 6.4) is still higher that other results obtained for samples of similar thickness. A possible reason is associated with different experimental setups to perform the abosrption measurement. Indeed, when the sample is introduced in the THz beam, it may slightly misalign the beam with respect to the second mirror. This misalignment results in a loss of a part of the beam on the second mirror that artificially reduces the detected signal with the sample. When the calculation is performed, the transmission is thus lower. An experiment to verify this point could be performed with a bigger second mirror which would be able to collect the beam even with a misalignment introduced by the sample.

6.1.3.2 GaAs substrate

The initial idea with this sample was to investigate if it could be used as a beam splitter in the THz frequency domain. The bench, as it has been initially designed is not able to measure the reflexion coefficient. Anyway, figure 6.5 shows the transmission spectrum of a 450 µm thick undoped GaAs piece of wafer. The calculated transmission of $\approx$ 20 % is good if, as for the PTFE sample of section 6.1.3.1, the transmission is under evaluated. Besides this study, it has been shown with an experiment at lower frequencies (0.110 – 0.325 THz) that this kind of sample could be used as a beam splitter with a $\approx 40/40$ % ratio and 20 % loss for THz near-field microscopy [Guillet 10].

6.1.3.3 Polyethylen (PE)

This last measurement is made using a stack of 20 sheets of 100 µm of polyethylen (PE). The result is shown in figure 6.6. The particularity of this material is the exceptional flatness over the whole investigated frequencies. As for the PTFE of section 6.1.3.1, the misalignments could explain the low

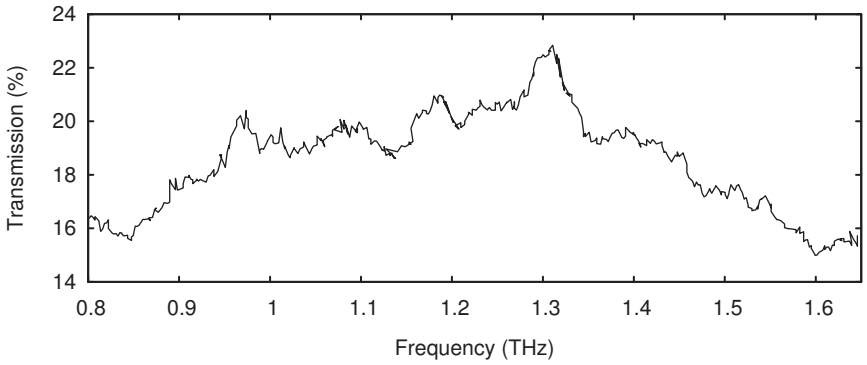

Figure 6.5: Transmission spectrum of a 450 µm thick undoped GaAs sample.

transmission value compared to the expected 85 % of a 2 mm thick sample investigated in [Tydex 10]. This material (in its high density bulk form – HDPE) has been used to fabricate the input and output windows of our cryostat used in the experiments of section 6.2.

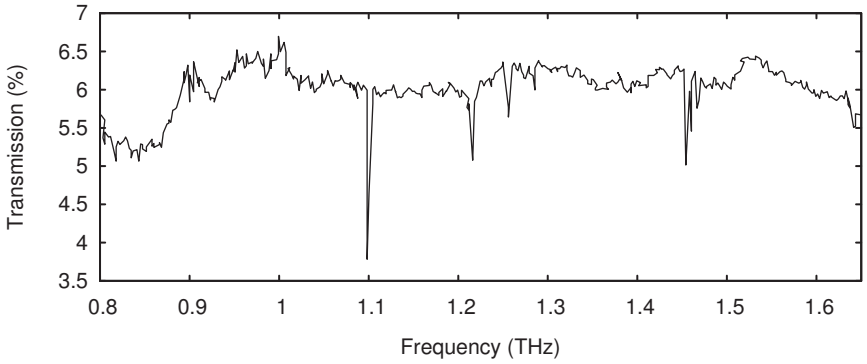

Figure 6.6: Transmission spectrum of a stack of 20 sheets of 100 µm of PE.

6.2 Room and low-temperature measurements with the electronic source

This section presents the results obtained by investigating the samples of chapter 3 under different conditions to extract their dependency on polarization, temperature, geometry, and bias. The results are sorted by varying each parameter to clearly understand the effect of each. As an introduction to the section, the way the experimental data is processed is explained in section 6.2.1.

6.2.1 About the data processing

The results presented in the following sections are issued from the setup of figure 4.27: the 0.220 – 0.325 THz electronic source and the bolometer are used. The samples are installed in the cryostat to keep the samples in temperature environments of 7, 15, 77, or 300 K.

The calibration spectrum of the bench with a pierced sample holder (figure 4.1(b)) installed in the cryostat is shown in figure 4.31. When we use this spectrum to calculate the gain of a sample using equation (4.10), it turns out that the result is not readable because between the calibration experiment

and the spectrum measurement with a sample, the cryostat has to be removed from the cradle, opened, and put back on the table. This creates different experimental conditions that causes the problem.

As a consequence, we decided, as discussed in section 4.4.2 to directly compare the spectra of the sample embedded into the cryostat with and without applied bias. The calculation is thus directly performed by dividing the spectrum with an applied bias $P_b(\nu)$ by the spectrum without bias $P_{b_0}(\nu)$. The result of this operation will be referred to as the transmission coefficient $\alpha(\nu)$:

$$\boxed{\alpha(\nu) = \frac{P_b(\nu)}{P_{b_0}(\nu)}} \,. \tag{6.4}$$

This coefficient allows us to evaluate the effect of the biasing conditions with respect to the unbiased condition. $\alpha(\nu) > 1$ means that the applied bias involves more detected power on the bolometer (i.e. the bias involves more transparency of the sample or even amplification), while $\alpha(\nu) < 1$ means that the applied bias involves more absorption of the sample. If $\alpha(\nu) = 1$, the bias has no effect on the transmission.

Moreover, the results have been smoothed to increase the readability of the curves. Indeed, even if the conditions are the same between the two experiments, there is a residual noise coming from the association bolometer/lock-in amplifier, added on the results. The smoothing is performed on $\alpha(\nu)$ by averaging a measure over the nine closest points:

$$\alpha(\nu_j) = \frac{1}{9} \sum_{k=j-4}^{j+4} \alpha(\nu_k) \qquad , \forall j \geqslant 4 \,. \tag{6.5}$$

Figure 6.7 shows the effect of the smoothing operation on a typical result obtained with our setup. One can see that the main features of the curve are still present after the smoothing process.

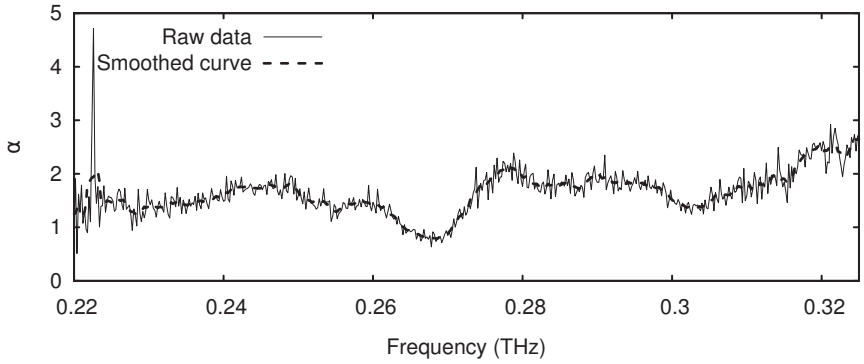

Figure 6.7: Illustration of the smoothing effect on a typical direct result of the transmission coefficient.

Finally, it is noteworthy to emphasize that the data at lower frequencies (< 0.225 THz) are not accurate due to the low power of the source in that domain (see the output power ot the source in figure 4.6).

6.2.2 Polarization dependence

In this section, two different experiments are performed to check the effect of the orientation of the sample with respect to the linear polarization of the incident beam on the sample. The sample is rotated by 90° between the two experiments, as sketched in figure 6.8: the direct polarization corresponds to the case where the polarization is along the conduction axis (i.e. perpendicular to the fingers), whilst the

crossed polarization corresponds to the case where the polarization is perpendicular to the conduction axis (i.e. along the fingers). The transmission coefficients measured in both cases are reported in figure 6.9.



(a) Crossed polarization (b) Direct polarization

Figure 6.8: Definition of the direct and crossed polarizations. The arrows illustrate the linear polarization of the incident beam.

It is clear that in the case of the crossed polarization, only small variations around 1 are found compared

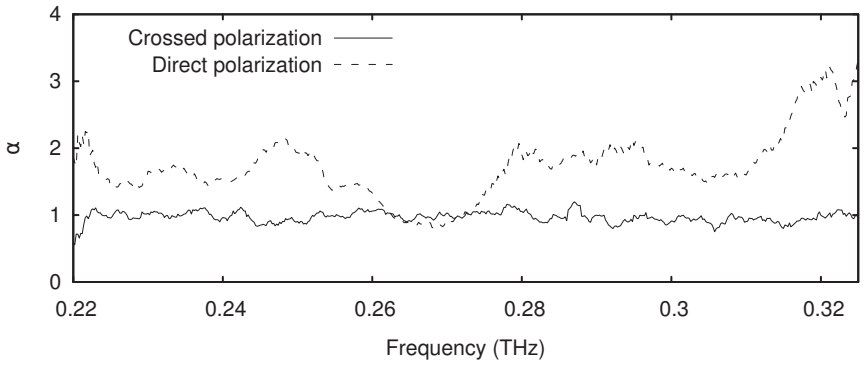

Figure 6.9: Effect of the polarization of the source with respect to the orientation of the sample on the transmission coefficient $\alpha(\nu)$. The studied sample is 6 and 52 µm long in the shortest and longest zones respectively, maintained at 77 K, with an applied voltage of 5.5 V.

to the direct polarization. In the case of the direct polarization, the spectrum is mainly always above 1, except for the frequencies between 0.262 and 0.272 THz, where the transmission coefficient fall down below 1. Thus, to obtain the maximum effect of the sample on the transmission coefficient, it has to be in direct polarization configuration.

As the wavelength of the incident wave is far bigger than the distance between two consecutive fingers, the fingers act like a metallic polarizer for the incident THz wave. In one hand, if the polarization of the wave is in the same direction as the fingers, the latter act like mirror, but in the other hand, if the polarization of the beam is perpendicular to the fingers, the wave can pass through them.

This result is very important since it demonstrates that the enhancement measured with the bias is linked to an interaction between the incident wave and the device under investigation. Thus, the increasing in the signal can not be simply attributed to a parasitic phenomenon occurring in the device itself, like heating of the device with the current, but to a physical phenomenon that actually occurs in the two dimensional electron gas.

6.2.3 Temperature dependence

Another parameter to investigate is the temperature. Recalling that the cryostat is able to generate temperature environments of 7, 15, 77, and 300 K, we investigate the variations on the transmission coefficient with the temperature. Figure 6.10 shows for the sample detailed in the caption the evolution of $\alpha(\nu)$ for temperatures of 7, 77, and 300 K. We chose not to try the experiment in the 15 K environment because of the complexity to use the cryostat in that configuration (the cryostat has to be dismounted to thermally link the cold head and the cold plate, which is not the case while using cryogenic fluids), as well as because of the vibrations of the cold head that would have occur during the experiment.

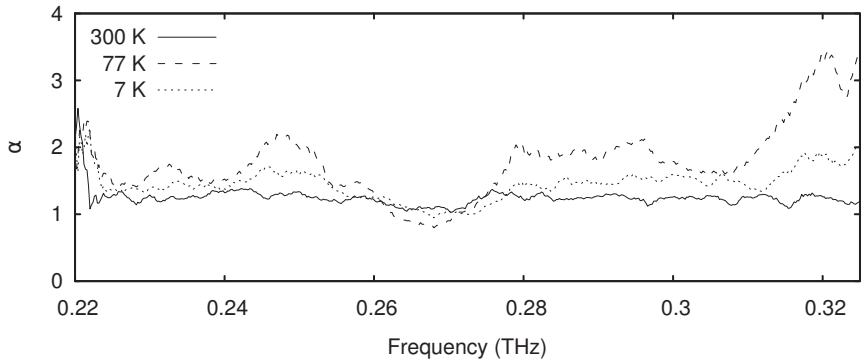

Figure 6.10: Effect of the temperature on the transmission coefficient $\alpha(\nu)$. The studied sample is $L_P = 19$ and $L_A = 39$ µm long, with a direct polarization configuration, and an applied voltage of 6.1 V.

In this figure, it is demonstrated that even if the applied bias has a small effect on the transmission coefficient in the case of the sample maintained at room temperature, it is negligible compared to the enhancement found at 77 and 7 K. This result shows that the properties of the sample modified by the decreasing of the temperature agree with the theoretical expectations. This is in accordance with the results of section 2.4.2, highlighting the fact that the deformation acoustic scatterings decreases with temperature, thus increasing the chances of the OPTTR mechanism to be activated in the device.

Another featured result is the lower transmission coefficient at 7 K compared to 77 K. This at present remains unexplained, but some possible explanations could be the following ones:

- the experimental setup may not be as appropriate as we thought in this temperature range. In other words, the cooling of the cryostat could be responsible of different parasitic effects such as material deformations because cooling is fast with liquid helium transfer (due to different expansion coefficients), or condensation on the windows resulting in additional misalignments or artificial power lowering ;
- the optical properties of the sample could have turned worst in that temperature range causing some measured power losses.

Finally, it is also emphasized that the absorption effect between 0.262 and 0.272 THz is also temperature dependent. The 300 K result does not show a transmission coefficient below 1 whilst both 77 and 7 K present the absorption effect. This effect is thus also related to properties variations of the sample with the temperature.

6.2.4 Geometry dependence

Besides the above investigations, we have analyzed the effect of the different geometries of contacts we dispose of on the fabrication mask. We recall that, as reported in section 2.5.1, an open problem

is still represented by the different role of the active and passive zones of the interdigitated fingers. Figure 6.11 summarizes our observations regarding the transmission coefficient for three samples of different asymmetry factor. The other parametric conditions (temperature, voltage, and polarization) are chosen to obtain results as clear as possible.

In this study, we did not investigated the symmetric devices because they are located on the border of the mask (see figure 2.25). So when a given mask is sticked on a pierced sample holder, these devices are located at the limit of the sample holder hole: this situation is the worst one in term of influence of the sample on the transmitted beam due to the appearance of diffraction phenomena.

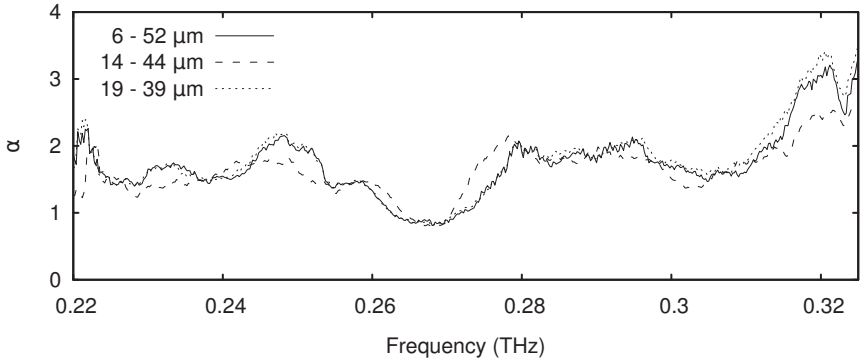

Figure 6.11: Effect of the geometry of the samples on the transmission coefficient $\alpha(\nu)$. The studied samples are maintained at 77 K in a direct polarization configuration with an applied voltage of 5.6 V.

We demonstrate with this result that for any of the device under consideration the response with the applied electric field remains similar. If the transmission enhancement were sensitive to the presence of electric fields in opposite direction in the active and passive zones, the transmission coefficient should decrease as the device becomes more and more symmetric. However it is not the case in our result, so the symmetric device should lead to the same results. These devices will be the subject of a particular investigation in a near future.

6.2.5 Electric field dependence

The last but not least parameter involved in our transmission results is the influence of the applied electric field. For that purpose, as for the other parameters it is possible to directly compare the spectra measured under different biasing conditions, or to use the *Tera-Spectro^{mini} with $I_d - V_d$ addon!* program, specially developed to measure the effect of the electric field on the transmission coefficient.

6.2.5.1 Direct comparison

Figure 6.13 summarizes the effect of increasing the applied bias on the transmission coefficient for three devices of different geometries. For each device, the applied voltage is varied in a reasonable range (to avoid device break down). It appears an overall considerable enhancement of the calculated transmission coefficient as the voltage is increased, specially between the low and middle voltages. The further enhancement between the middle and higher voltages is still recorded, but is less important than in the former case.

Concerning the shape of the spectra, it seems that all the peaks, valleys, and variations recorded for each voltages match with each other, except for the absorption area between 0.262 and 0.272 THz: we

find in all the studied samples that this frequency band, where the applied electric field results in an absorption, shifts to the lower frequencies as the bias increases. At the moment, this phenomenon is not yet understood, and would need further experiments to be explained.

This result demonstrates that our devices are able, under biasing conditions to modulate the transparency of the sample, or even to create some amplification. This latter point is fairly true if, as for the gain calculation of section 4.3.3, we consider that the effect on the transmission coefficient with the applied bias compared to the relative area of the device under study is enormous. Indeed, $\alpha(\nu)$ is found to be over 2 on some frequency bands, which would be hardly the consequence of the transparency modulation of the studied sample, alone.

Let us evaluate the effective gain of our samples. Recall that the value of $K = 0.0157$ found in equation (4.3) page 81 is under-evaluated, and that the gain can be calculated with the formula of equation (4.10) page 82. The calculation of the gain in the case of the 19 – 39 µm sample gives the results of figure 6.12. The calculations are here performed with the smoothed data (see formula of equation (6.5)) to try to take as rid as possible of the variations in the measured spectra.

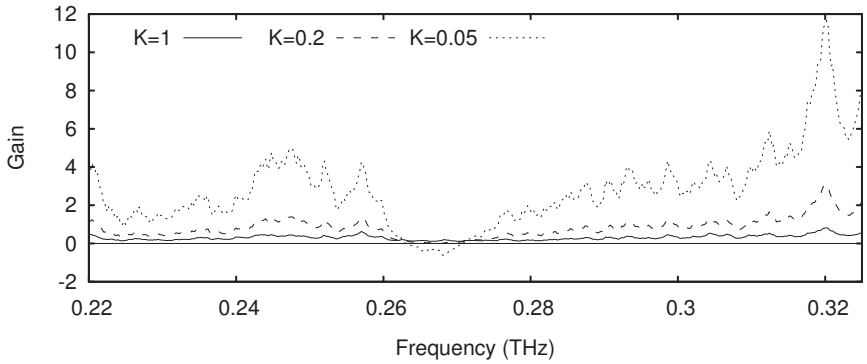

Figure 6.12: Gain calculation of a 19 – 39 µm device maintained at 77 K with an applied bias of 6 V for different values of the K factor. $K = 1$ corresponds to the direct calculation of the gain by dividing $P_b(\nu)$ by $P_c(\nu)$.

As seen, if the value of K is below a certain value, the gain is found negative in the absorption part of the spectrum, which is, of course, not possible. To understand this result, we have to look at the condition needed for this calculation to become negative. Starting from equation (4.10), we find the condition on the measured spectrum under biasing conditions:

$$P_b(\nu) < (1 - K)P_{b_0}(\nu) \; . \tag{6.6}$$

Assuming that the value of K is well established, this condition means that the total power measured with an applied bias is less than the power found without bias excluding the device under investigation area. This latter point can only be achieved for two reasons:

- The value of K is more than expected: even if this may be true, we found with our results that to avoid negative values we have to use a $K \geqslant 0.2$. This value is more than 10 times greater than the calculated one, which may not be realistic.
- The applied bias, by its consecutive effects (increasing the local temperature or deforming the sample [1]), artificially decreases the measured power under biasing conditions.

1. The deformation of the sample could be either due to dilatation mismatch between materials or to piezo-electric effects occurring in the device itself.

The explanation might come from both of these reasons. Anyway, it is still found that the gain is still above one in some parts of the spectrum, whatsoever the value of $K < 0.5$ is considered. This means that our devices may present a real gain in these regions. This point will be further investigated in the following of the project by trying new ways to do the experiments, such as placing a detector right after the sample to be sure to collect all the beam transmitted through the sample. This will be discussed while drawing the perspectives of this thesis.

Finally, a last effect that may disturb the measurement when the transmitted power is increased by the biased device is the fact that the transmitted beam is more concentrated close to the device under study (i.e. the power profile of the beam after the sample is not homogeneous but with a high concentration close to the amplificating sample). This involves an increased divergence of the beam after the sample compared to the unbiased case, which eventually creates losses of power under biased conditions. This latter point can be checked by using a smaller detector directly placed in front of the device inside the cryostat. For example, a pyro-detector or a Schottky diode could be used for that purpose, if their sensitivity and temperature operating range are in accordance with the power and temperatures involved in the measurements.

6.2.5.2 Using the *Tera-Spectro^{mini} with $I_d - V_d$ addon!* program

A different way to evaluate the effect of the electric field on the transmission coefficient is to use the *Tera-Spectro^{mini} with $I_d - V_d$ addon!* program. Indeed, with this program the problem is reversed. A constant frequency is generated by the source whilst the applied voltage is swept to record the effect on the bolometer signal.

The results for three different device geometries and for five different frequencies are summarized in figure 6.14, where the curves are smoothed with bezier lines to increase the readability.

We can see that overall the behavior is the same for the three different geometries. Every curve can be linked with the spectra of figure 6.13, showing that the enhancement proportion depends on the frequency. Except for the curve of 0.262 THz, all the curves present a threshold ($\approx$ 2 V) before starting to increase the transmission coefficient.

These results may represent the first signature of the amplification of the samples by the activation of the OPTTR mechanism, but more investigations have to be led to confirm this interpretation. Anyway, the applied electric fields of the beginning of the enhancement matches the OPTTR amplification band calculated with the Monte-Carlo simulations (see figure 2.20 page 45). To confirm the link with the OPTTR, it should be demonstrated that the enhancement is decreasing after the observed maximum as the voltage is still increased. The whole curve will thus present a *bell-shape*, which will be characteristic of OPTTR. At the moment our experimental setup does not enable to investigate the transmission at voltages higher than 6 V.

Let us focus on the case of the 0.262 THz curve: this curve is measured in the lower part of the absorption region of the devices. One can see that the starting of the curve is similar to others, with some kind of threshold, but, around 4 V, on the opposite to the other curves, the transmission coefficient starts to decrease, even bellow 1, confirming the *absorbing effect* of the bias in that region.

6.3 Summary

In this chapter, we summarized the main results obtained with the transmission setups described in chapter 4. For the case of the interdigitated fingers, we demonstrated an enhancement of the transmission

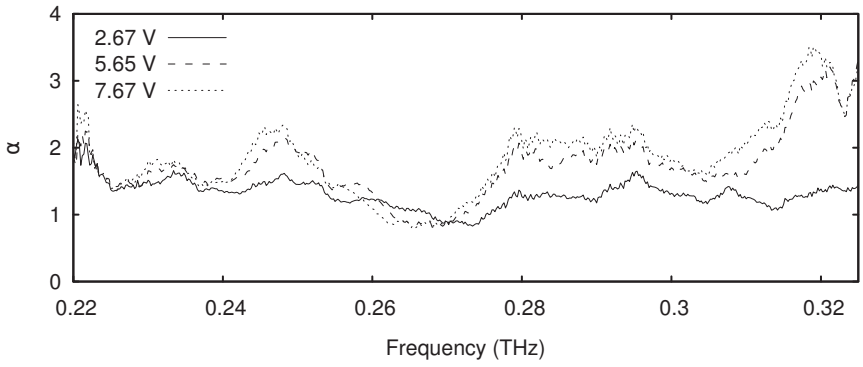

(a) 6 – 52 µm

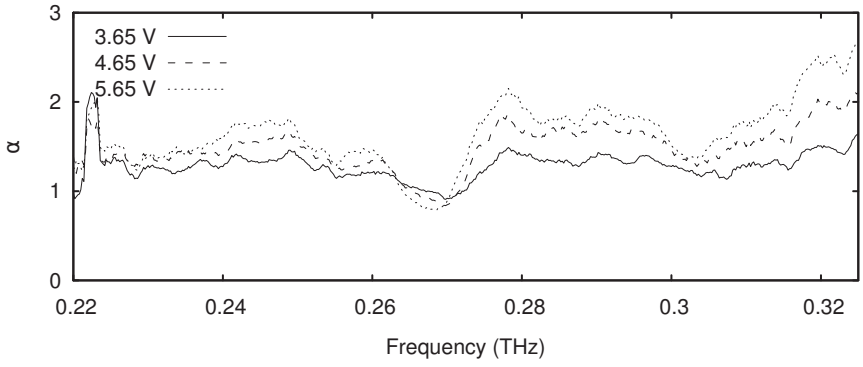

(b) 14 – 44 µm

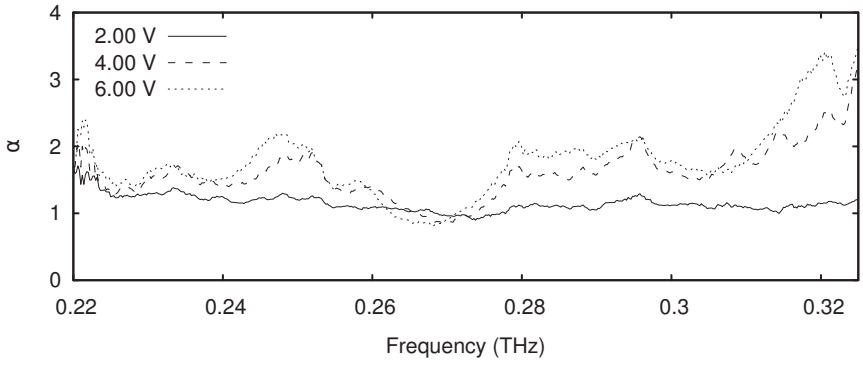

(c) 19 – 39 µm

Figure 6.13: Effect of the applied electric field on the transmission coefficient $\alpha(\nu)$. The studied samples are maintained at 77 K in a direct polarization configuration. The lengths indicated in the captions correspond to the short and long zones of the interdigitated fingers of the investigated device.

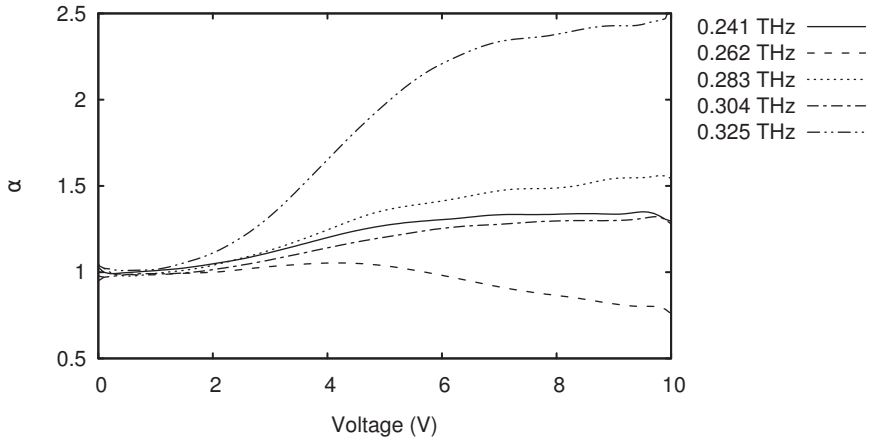

(a) 6 – 52 µm

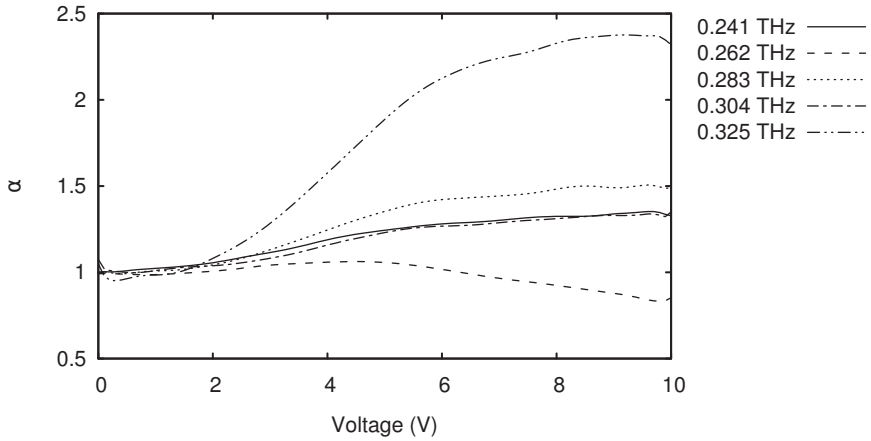

(b) 14 – 44 µm

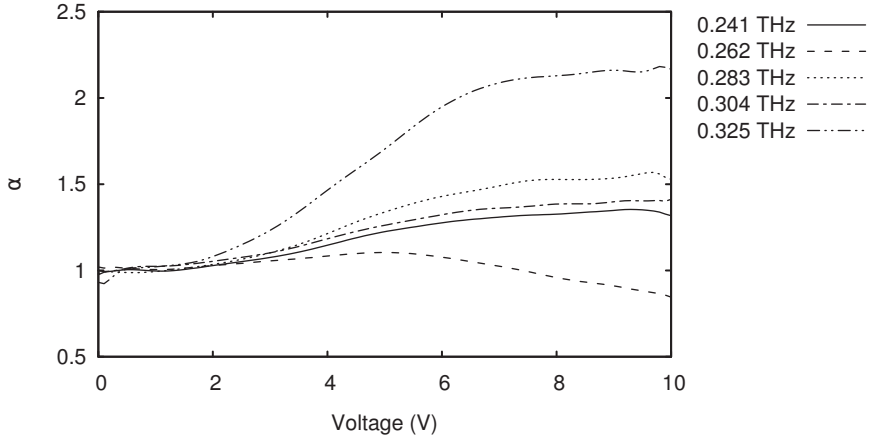

(c) 19 – 39 µm

Figure 6.14: Effect of the applied electric field on the transmission coefficient $\alpha(\nu)$ for different frequencies. The studied samples are maintained at 77 K in a direct polarization configuration. The lengths indicated in the captions correspond to the short and long zones of the interdigitated fingers of the investigated device.

coefficient with the increasing of the bias which is both temperature and polarization dependent. No effect is found in the case of the samples maintained at room temperature or in a crossed polarization configuration (see figure 6.8). This shows the fact that the detected effect only occurs when the incident beam has the right polarization to cross the fingers and when the material is cooled down to temperatures limiting effects such as acoustic phonons interactions.

We have presented experimental results showing clearly the effect of applied bias on the transmission of electromagnetic radiation in the frequency band 0.220 – 0.325 THz. Taking into account the surface of the biased devices this leads to a gain which is higher than unity. This result can be considered very promising in view of the development of a THz MASER and moreover is in agreement with the theoretical predictions attributing this phenomenon to the OPTTR mechanism.

General summary

The beginning of this thesis almost coincided with the kick-off of the AITHER project in February 2008. The close collaboration with our partners allowed to be able to start the experimental design and assembly quickly after the official launch of the project. This timetable was suitable to build and characterize the experimental setup within the IES during the first year of the project while the first samples to study was fabricated by the CRHEA. During this first year, most of the time was devoted to find and buy the experimental equipment, as well as to make the new sectional photomixing bench work. The latter point took a long time since the optical alignments had to be perform, as well as to create the LabView program able to control the laser system to transform the individual devices and instruments into a spectroscopic bench.

The results obtained with the photomixing bench presented in section 6.1 were measured at the end of year 2008 and presented in different national and international conferences: JNRDM [2], JTHz [3], and EDISON [4]. The measurements also highlighted the low power of the photomixing source and the need to find another solution for the low temperature bench, including the cryostat. At that time the first electronic source (0.220 – 0.325 THz) were bought with the promise to deliver sufficient power to embed it on the cryogenic setup.

The first GaN samples were delivered by the CRHEA in March 2009. The first electrical measurements in real condition on the DC/pulsed test benches were carried out. Some transmission measurements were attempted, but these samples were grown with an existing mask mostly including HEMT structures and without interdigitated structures. As a consequence, nothing conclusive have been extracted from these results. Anyway, these first samples still have delivered some of the results regarding the electrical measurements of chapter 5, and the passive transmission with the photomixing bench of section 6.1.2.

Several months later, a post-doctoral researcher, Dr. Rajesh SHARMA, started his work at the IES laboratory. Dr. Sharma were helpful to perform the measurements with the samples as well as to provide new ideas. We performed many measurements on the old mask until March 2010, when the new samples were available for test. A new mask (figure 2.25) including the interdigitated structures were used to grow these ones. As a consequence, the year 2010 was the most productive in term of experimental results and provided the main part of the outcome introduced in this thesis.

Concerning the perspectives of this work, several lines could be drawn to improve the results:

The samples: from the basis of the investigations performed in the framework of this thesis, several improvements of the sample structure can be imagined:

- It has been shown that the resistance ratio between access and channel resistances is unfavorable from a electrical point of view. Most of the applied voltage is spread over the access resistances

2. National Days of the Doctoral Network in Microelectronics 2008, Bordeaux.
3. TeraHertz Days 2009, Lille.
4. 16th international conference on Electron Dynamics In Semiconductors, Optoelectronics and Nanostructures, 2009, Montpellier. The articles were published in the Journal of Physics: Conference Series.

instead of the channel. It is thus important to lead some research in that sense in order to be able to have more facilities to reach higher electric fields in the channel without breaking down the device. We proposed a novel structure, consisting in dividing the structure in smaller zones by adding contact bridges, but a special care have to be taken to avoid the same *polarizer* effect when the source polarization is in the same direction than the fingers. The bridge thus have to be moved further apart from each other accordingly to the studied wavelength.

- The same objective to decrease contact effects can be improved from a technological point of view by lowering the access resistances from the contacts to the channel.
- At present, some of the samples still haven't be tested (in particular the symmetric ones). They should be investigated to confirm our thoughts on the fact that the different electric field directions in the two opposite zones of the interdigitated structures does not have influence on the results.
- Finally, a new generation of samples should be delivered by the end of the year. The CRHEA is growing some new samples on a GaN substrate instead of the sapphire one. This may result in samples of better quality since the dislocation concentration is far less when GaN structures are directly grown on GaN substrates. As a consequence, we expect better results with these new samples since electron transport properties will be better and the OPTTR mechanism will undergo less parasitic effects.

The electrical measurement setups: especially in the case of the pulsed setup, the bench could be improved to increase the accuracy as well as the voltage range. Indeed, our source and oscilloscope association is too limited to be able obtaining the accuracy needed for the OPTTR investigation. We know that the detection of the activation of the OPTTR mechanism is close to 0.1 V. Although our pulsed setup have an accuracy of the order of 0.1 V. This performance could be improved by optimizing the connections between the source and the sample (inside the cryostat), partially responsible of the worsening of the pulse shape, and by consequence, of the measurement.
Moreover, in the case of the interdigitated structures, the pulsed setup is limited by the applicable voltage range, because of the high power needed to supply this kind of sample. This could be solved by purchasing a new source able to deliver higher power, still with sub-microsecond pulse width.

The photomixing bench: the weakest point of this bench is the lack of power and the mid-term mechanical stability of the optical alignments. Consequently, everything have to be optimized in the sense of reducing as much as possible all the power losses on the bench. For example, the parabolic mirrors have to present the greater numerical aperture to collect the biggest part of the beam, while their focal length should be reasonable to avoid long travels of the beam whose absorption in the atmosphere is important. As mentioned in section 6.1.1, a special care has to be given to the second mirror whose numerical aperture should be much greater than the beam diameter to avoid losses of power after introducing a sample in the beam.

The low-temperature transmission measurements: this is the core of the subject and could be improved in several ways:

- Concerning the cryostat itself, the whole experiment could be easier to manage if we would dispose of a smaller cryostat. The cryostat we are using is very big compared to our real needs. Nowadays some small cryostat with high cooling performances and very low vibrations exists and would be a good investment.
- With another cryostat, the focusing spherical mirrors could also be changed for parabolic mirrors which have better performances in term of optical distortions.

- In term of frequency, the second electronic source (0.843 – 1.100 THz) should be embedded in the bench to compare with the existing results. This should confirm that the enhancement detected with the first source is related to the OPTTR mechanism or not. Indeed, if we can show that the applied electric field needed to get the same enhancement is higher in the case of the higher frequency source, this means that the enhancement is following the amplification behavior demonstrated by the Monte-Carlo simulations (see figure 2.20).
- The measurement of the transmitted beam is problematic: the diffraction introduced by the sample itself as well as by the sample holder (the pierced hole is smaller than the beam) leads to doubts about what is detected by the bolometer which is outside the cryostat. This point could be improved by placing a detector directly after the sample, inside the cryostat. For the liquid helium cooled experiments, a silicon bolometer of the same type as the one used in the existing bolometer could be used. But in the case of other temperatures measurements, this will not work. Another detector to use could be some pyro-electric sensors, which works from low to room temperature [Bravina 07], even its behavior is affected at very low temperature: thermally isolating the sensor from the cold plate may solve that issue.

As a conclusion, the present thesis only constitutes the first part of the project which will surely produce, in a short time, some international communications on the subject. The results obtained in the framework of this work show the great potential that we can expect from our devices and benches. Many experiments are still pending to be performed, and some improvements of the experimental setups should clarify some results.

Part IV

Appendices

Appendix A

Electrical characterizations of grown samples

The different techniques used to measure the electrical parameters of our devices are described in this appendix. These measurements have been performed by our collaborating group of the CRHEA laboratory in Sophia Antipolis.

A.1 Capacitance-voltage measurements

This measure is realized with the help of a mercury probe and an Agilent 4284A impedance-meter. The mercury associated with the semiconductor create a Schottky contact (gate contact), but its poor quality and the wide contact surface of the source port allows to consider the latter as an ohmic contact. A scheme of this kind of probe is illustrated on figure A.1.

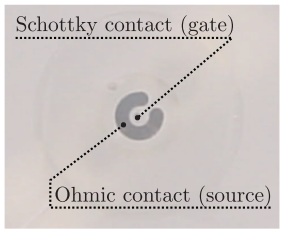

Figure A.1: Photography of a mercury probe used for capacitance-voltage measurements.

As a negative voltage V_{gs} is applied on the Schottky contact, the space charge zone is enhanced on the semiconductor side. The quantum well of the structure is completely depleted of electrons for a pinch-off voltage $V_{gs} = V_p$. The space charge zone thus behave like a parallel plan capacity whose electrodes are on one side at the metal/semiconductor interface, and on the other side on a plane where the free carriers are maintained, at a distance W from the top of the structure, depending on the applied voltage on the gate. This capacity C is measured as a function of the applied voltage V.

$$C(V) = -\frac{dQ}{dV} = qAN_d\frac{dW}{dV}\ , \tag{A.1}$$

where Q is the charge in the semiconductor, W is the width of the space charge zone, A is the Schottky

contact area, and q is the charge of an electron. A typical curve of $C(V)$ measurements is sketched in figure A.2.

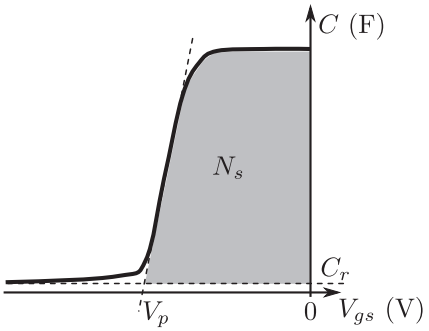

Figure A.2: Typical capacitance-voltage measurement with a mercury probe.

The integration of the $C(V) - C_r$ curve between $V_{gs} = 0$ V and $V_{gs} = V_p$, where C_r is the residual capacity measured below the pinch-off voltage, is equal to the surface density of carriers in the channel N_s:

$$N_s = \frac{1}{qA} \int_{V_p}^{0} (C(V) - C_r)\, dV \,. \tag{A.2}$$

Moreover, if we consider a uniform doping of the material, it is possible to calculate the carriers density profile in the layers of the structure.

$$N_d = \frac{2}{q\varepsilon_r\varepsilon_0 A^2 \frac{d\left(1/(C(V)-C_r)^2\right)}{dV}} \,, \tag{A.3}$$

where ε_r is the dielectric constant, and ε_0 the vacuum permittivity.

A.2 Van der Pauw and Hall effect measurements

In the case of a quantum well channel, the resistance can be calculated by the formula:

$$R = R_S \frac{L}{W} \,, \tag{A.4}$$

where R_S is the sheet resistance, L is the length between the contacts, and W is the transversal width of the channel.

The measure of the sheet resistance can be achieved using the *Hall cross* pattern (figure A.3), which has a correct geometry to apply the Van der Pauw method. This method uses four probes allowing to remove the contact resistances from the measure.

A.2.1 Van der Pauw – sheet resistance measure

The sheet resistance of an arbitrary shaped sample can be calculated from the measure of the resistances along the two axes **x** (R_x) and **y** (R_y). The Van der Paw formula links the sheet resistance R_S with R_x and R_y [van der Paw 58]:

$$\exp\left(-\pi\frac{R_x}{R_S}\right) + \exp\left(-\pi\frac{R_y}{R_S}\right) = 1 \,. \tag{A.5}$$

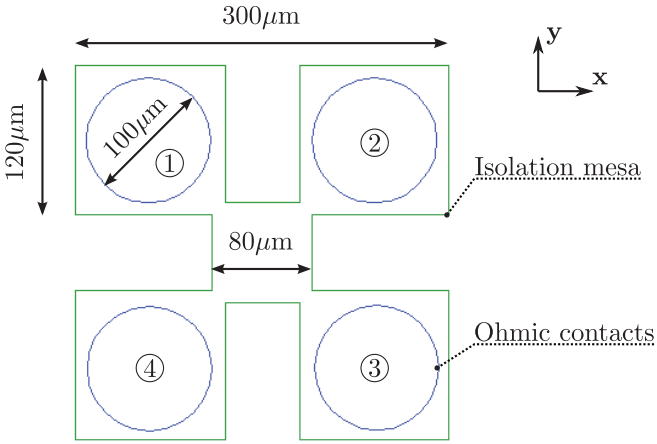

Figure A.3: Pattern of a Hall cross used on our samples.

The sheet resistance can thus be evaluated by the formula:

$$R_S = \frac{\pi}{\ln(2)} \frac{R_x + R_y}{2} f\left(\frac{R_x}{R_y}\right) , \tag{A.6}$$

where f is a function of the ratio $\frac{R_x}{R_y}$ used to correct the asymmetry of the sample. This function satisfies the formula:

$$\frac{R_x - R_y}{R_x + R_y} = f \cosh^{-1}\left(\frac{\exp\left(\frac{\ln(2)}{f}\right)}{2}\right) . \tag{A.7}$$

The evolution of f as a function of the $\frac{R_x}{R_y}$ ratio is reported in figure A.4.

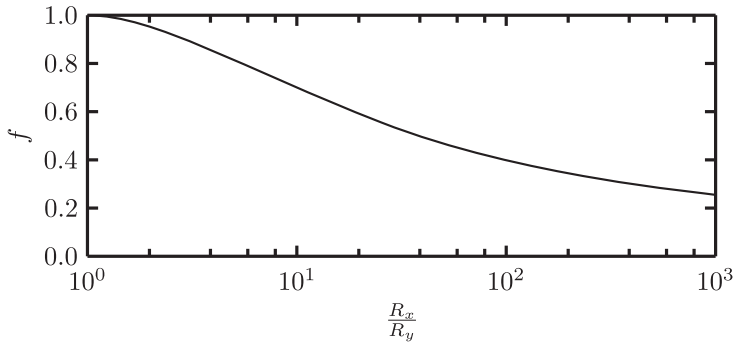

Figure A.4: Evolution of the asymmetry function f as a function of the $\frac{R_x}{R_y}$ ratio.

Finally, the measurement of R_S is performed by applying a current between ports 1 and 2 – I_{12} – (see figure A.3) and measuring the voltage between ports 3 and 4 – V_{34} –, followed by a current injection between ports 2 and 3 – I_{23} – and measuring the voltage between ports 4 and 1 – V_{41} –. The two resistances defined by the ratios $R_{34,12} = \frac{V_{34}}{I_{12}}$ and $R_{41,23} = \frac{V_{41}}{I_{23}}$ respectively correspond to R_x and R_y.

The accuracy of the measurement can be enhanced by performing the reciprocal measurements

$R_{12,34} = \frac{V_{12}}{I_{34}}$ and $R_{23,41} = \frac{V_{23}}{I_{41}}$ and average the calculation over the two measurements:

$$R_x = \frac{R_{12,34} + R_{34,12}}{2} \tag{A.8}$$

$$R_y = \frac{R_{23,41} + R_{41,23}}{2} \tag{A.9}$$

A.2.2 Hall effect – mobility and surface density of charge measurement

When an magnetic field $\mathbf{B}$ is applied perpendicularly to the current I in the studied material, the electrons are deflected to a side of the sample by the Lorentz force $\mathbf{F_l}$:

$$\mathbf{F_m} = -q\mathbf{v} \wedge \mathbf{B} \, , \tag{A.10}$$

where $\mathbf{v}$ is the velocity vector of the electrons, and q the element charge of carriers. This force involves a disequilibrium of the space repartition of charges between the two sides of the device. The disequilibrium creates an electric field $\mathbf{E_H}$ in the perpendicular direction of travel of electrons which also breeds a Coulombic force $\mathbf{F_e}$:

$$\mathbf{F_e} = -q\mathbf{E_H} \, . \tag{A.11}$$

This force acts on carriers and partially compensates the first effect. This is the so-called *Hall effect*. The *Hall voltage* V_H is thus measurable and is related to the surface density of charges N_S:

$$V_H = -\frac{IB}{qN_S} \, . \tag{A.12}$$

This measurement can thus be used to measure the surface density of charge in the channel:

$$\boxed{N_S = -\frac{IB}{qV_H}} \, . \tag{A.13}$$

When the measurement is performed, the Hall cross of figure A.3 is used. In a first time, a positive magnetic field is applied perpendicularly to the surface of the sample, whilst a current I_{24} is injected between ports 2 and 4. The voltage V_{13}^+ is measured between ports 1 and 3. The same operation is performed with I_{13} and V_{42}^+. As for the van der Paw measurements, the current can be applied in the opposite direction to measure V_{31}^+ and V_{24}^+ for the applied currents I_{42} and I_{31}, respectively. A negative electric field will produce, with the same measurements the values V_{31}^-, V_{13}^-, V_{24}^-, and V_{42}^-. The voltage differences induced by the change of the magnetic field direction are:

$$\begin{cases} V_{13} &= V_{13}^+ - V_{13}^- \\ V_{31} &= V_{31}^+ - V_{31}^- \\ V_{24} &= V_{24}^+ - V_{24}^- \\ V_{42} &= V_{42}^+ - V_{42}^- \end{cases} \tag{A.14}$$

Finally, the Hall voltage is given by the average:

$$V_H = \frac{V_{13} + V_{31} + V_{24} + V_{42}}{8} \tag{A.15}$$

In addition, the mobility of electrons can be calculated by the formula:

$$\boxed{\mu = \frac{1}{qN_S R_S}}\,. \tag{A.16}$$

A.3 Buffer layers resistivity

The resistance of the buffer layers R_B is measured between two ohmic contacts separated by a deep etching of 150 nm. In our case, some symmetric interdigitated fingers patterns of 100 µm long and separated by 10 or 5 µm are used, as sketched in figure A.5.

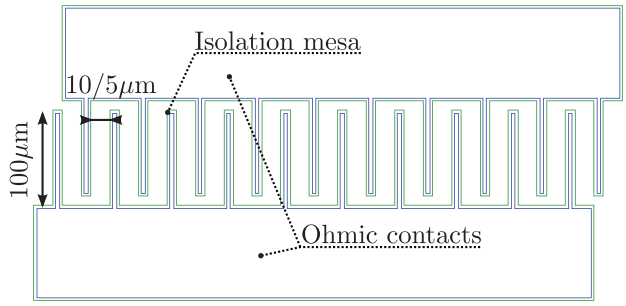

Figure A.5: Isolation pattern used to measure the resistance of the buffer layers R_B.

A.4 Contact and sheet resistances measurements

The classical way to measure the contact resistance R_C, as well as the sheet resistance R_S, is the transmission line model (TLM) technique. It is based on the hypothesis that the contact resistance is determined by the metal/semiconductor interface and the uniformity of the resistivity under the contact. The TLM technique requires a pattern composed by several ohmic contacts separated by different lengths, as sketched in figure A.6.

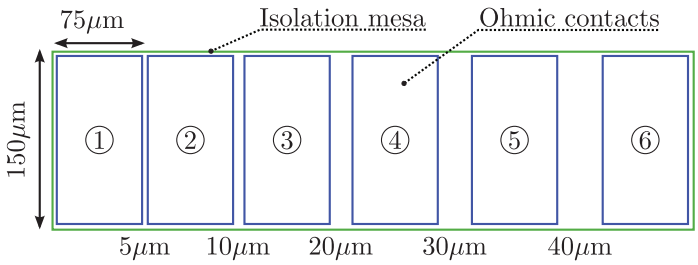

Figure A.6: Transmission Line Model pattern used to measure the contact resistance R_C and the sheet resistance R_S.

From this structure, continuous current-voltage characteristics are performed between consecutive contacts, and the calculated resistance is reported in a graph as a function of the distance between contacts. The contact and sheet resistances are calculated from the curve which equation is:

$$R(L) = R_S \frac{L}{W} + 2R_C\,, \tag{A.17}$$

where L is the length between contacts, W the width of the channel, and R is the measured resistance, as illustrated in figure A.7

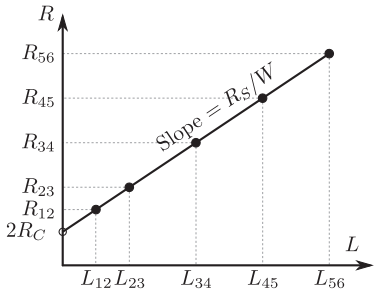

Figure A.7: Measurement of the resistance as a function of the length between contacts L on the TLM structure.

The contact resistance is usually expressed in Ω.mm, by multiplying the calculated value by the width of the contacts W (0.150 mm in our case).

Appendix B

Description of the *Tera-Spectro* program

B.1 Introduction

In order to be able performing spectroscopic measurements with the photomixing antenna, the main problem is to control the wavelength and power of the two upstream lasers that creates the optical beating.

The couple (λ_i, P_i) where λ_i and P_i are respectively the wavelength and the power of the laser i, are determined by the couple of parameter (I_i, T_i), where I_i and T_i are respectively the current and temperature of the laser i:

- The temperature mostly acts on the wavelength. The manufacturer of the lasers measured a temperature tunning of our lasers of ≈ 36 GHz/°C.
- The current is classically acting on the emitted power (a quasi linear increasing after the lasing threshold) as well as on the wavelength (mostly due to the self heating with the increasing of the current). The current tunning is ≈ 1.33 GHz/mA.

It is usually considered that for a given couple (I_i, T_i), there exists only one couple (λ_i, P_i). In reality, the laser system includes a semiconductor optical amplifier which induce some power perturbations on the output signal depending on the two lasers. This is due to the competition between the two lasers to share the gain of the amplifier which is in saturation regime. The global system is by consequence complex to control.

B.2 Regulation of the lasers

The choice we used for this purpose was the following: considering that a given beating frequency ν has to be reached, we apply the following procedure

- One of the two lasers is kept with constant parameters (I_1, T_1) chosen in accordance to ν (this choice is made to be able to reach the beating frequency by only playing on the parameter of the other laser in its operating ranges);
- Then, the parameters of the other laser are controlled by two overlapped regulation loops on the temperature and current two reach the wanted beating frequency.

This latter point is the hardest to settle, because it can add some instabilities to the setup. In one hand, the regulation on the current is performed by a step-by-step loop, and in the other hand, the regulation on the temperature is performed by a proportional, integral, derivative corrector (PID controller). For

each iteration, the power of the laser after the amplifier is measured and compared to a reference: if the power is less than the reference, the current is increased by a current step ΔI, and in the opposite, the current is decreased. This loop is active with a tolerance of 5% around the reference: if the power is within this reference, the current remains. This loop is detailed in figure B.1.

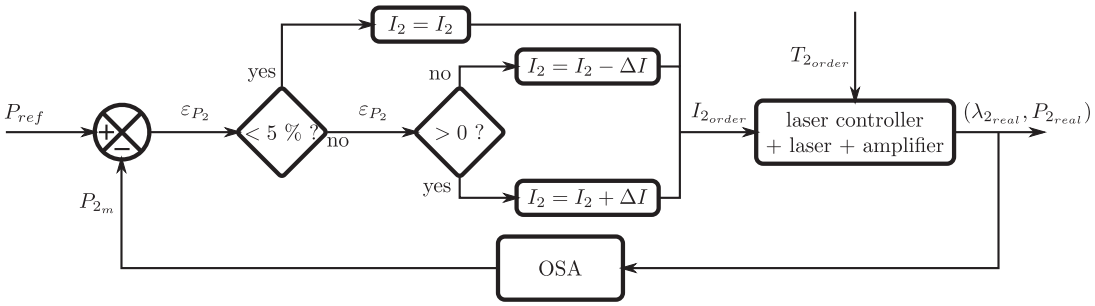

Figure B.1: Step-by-step regulation loop of the power of the laser 2.

As far as the temperature regulation is concerned, a full PID correction is involved. The wavelength is measured after the amplifier with the help of an optical spectrum analyzer and compared to the reference wavelength, which is calculated from the value of ν and the wavelength of the second laser. The error signal (difference of the measurement and the reference) is sent to the PID corrector. The output of the corrector constitutes the temperature order to send to the controller of the laser. The regulation loop of this side of the program is illustrated in figure B.2.

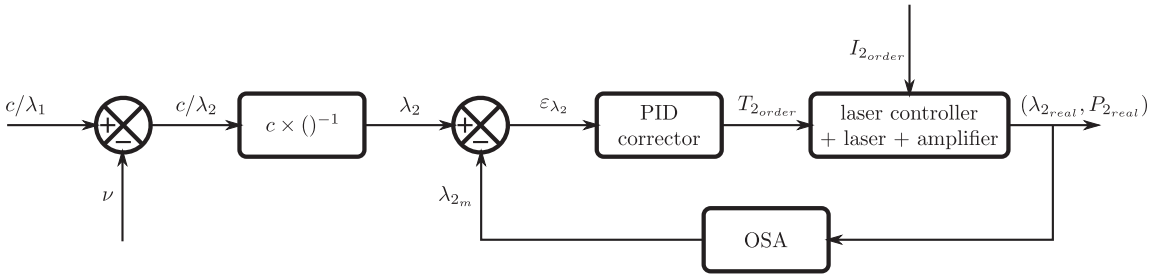

Figure B.2: Regulation loop of the wavelength of the laser 2.

The rules of the PID corrector were performed by a measuring the open-loop step change response of the whole system and applying the Ziegler and Nichols criterion [Ziegler 93]. The values ruled the first set of PID parameters for the regulation, but the non-linearities present in the system created instabilities of the regulation. This is mainly due to the time response of the wavelength and power measurements which depends of the communication between the OSA and the computer. This time can vary between several experiments. As a consequence, the PID parameters are further manually adjusted to reach a stable and as fast as possible regulation of the wavelength.

List of Figures

1.1 Terahertz domain in the electromagnetic spectrum 8
1.2 Terahertz radiography of a decayed tooth 9
1.3 Non-destructive control of an electronic RFID tag through the packaging 9
1.4 Whole-body imaging system developped by L-3 communications® 10
1.5 Example of whole-body imaging 10
1.6 Projection of the full sky in Galactic coordinates at a frequency of 1.4611 THz 11
1.7 Current-electric field characteristics of a gunn diode 12
1.8 Typical layers scheme of a resonnant tunnel effect diode 12
1.9 Step by step building of the current-voltage characteristics of a tunnel effect diode 13
1.10 Typical layer scheme of a high electron mobility transistor (HEMT) 13
1.11 Typical layer scheme of a heterojunction bipolar transistor (HBT) 14
1.12 Schematic picture of the energy levels in two adjacent blocks of a quantum cascade laser . 14
1.13 Illustration of the mixing of two lasers 16
1.14 Refractive index variations induced by electric field in InP 17

2.1 Evolution in the phase space of a system between times t and $t + dt$. 21
2.2 Scattering of a wave packet centered at $k = k_0$ to one centered at $k = k'_0$. 23
2.3 Scattering mechanisms in cubic semiconductors [Reggiani 85]. 27
2.4 Illustration of a scattering event. 28
2.5 Perfect scattering rate as a function of electron energy needed for OPTTR. 34
2.6 A constant electric field applied on a perfect material. 35
2.7 Illustration of the cyclic energy of electrons moving in a perfect material 36
2.8 Illustration of the deterioration of the cyclic movement. 38
2.9 Scattering rates due to polar optical phonon emission in different materials. 39
2.10 Real part of differential mobility spectrum. 39
2.11 Maximum value of the DNDM and frequency limits of the amplification band. 40
2.12 Real part of the differential mobility and dynamical gain as a function of concentration. . 40
2.13 Main scattering rates in bulk wurtzite GaN at 10 K temperature. 41
2.14 Evolution of deformation acoustic scatterings for different temperatures. 42
2.15 Evolution of polar optical phonon scatterings for different temperatures. 42
2.16 Evolution of ionized impurities scatterings for different doping concentrations. 43
2.17 Amplification band in bulk GaN. 43
2.18 Main scattering rates in a 5 nm wurtzite GaN quantum well at a temperature of 10 K. . . 44
2.19 Evolution of scatterings with DA phonons for different temperatures in a 2DEG. 44
2.20 Amplification band in a 5 nm GaN quantum well. 45

2.21 Comparison of different materials amplification bands. 45
2.22 Illustration of a pattern of the interdigitated fingers. 46
2.23 Simplified scheme of interdigitated fingers. 47
2.24 Simplified scheme of asymmetrical interdigitated fingers. 47
2.25 Design of the mask of our samples 48

3.1 Different layers grown on sapphire substrate to build the GaN quantum-well. 52
3.2 Vertical valence and conduction bands diagram. 53
3.3 Vertical conduction band diagram 54
3.4 Dimensional parameters of interdigitated fingers. 55
3.5 Schematic diagram of a MBE machine. 57
3.6 Large and magnified views of interdigitated fingers obtained by SEM. 59
3.7 Sample surface observed with AFM studies. 60
3.8 Current-voltage characteristics of different fabricated interdigitated fingers. 61

4.1 Illustration of a TO-8 case with 16 pins 65
4.2 Inside bottom view of the cryostat. 66
4.3 External view of the cryostat. 67
4.4 Base plate in place in the cryostat. 67
4.5 Schematic diagram of the 0.220 – 0.330 THz source from Spacek Labs. 67
4.6 Output power as a function of frequency of the 0.220 – 0.330 THz source. 68
4.7 Radiation pattern of the output beam from the horn antenna. 68
4.8 Schematic diagram of the 0.843 – 1.100 THz source from VDi. 69
4.9 Output power as a function of frequency of the 0.843 – 1.100 THz source. 69
4.10 Final stage of the 0.843 – 1.100 THz source 69
4.11 Illustration of the photomixing source from EKSPLA. 70
4.12 Internal scheme of the Sacher laser system. 70
4.13 Full bench of THz generation with a photomixing antenna. 71
4.14 Definition of the direct and crossed polarizations. 72
4.15 Internal scheme of our bolometer. 73
4.16 Full bench of THz generation and homodyne detection with photomixing antennas. . . . 74
4.17 Cryostat mounted in its old configuration with its cradle and the spherical mirrors. 75
4.18 Cryostat configured for transmission measurements with the spherical mirrors. 75
4.19 Illustration of the full bench. 76
4.20 Simulation of the beam waist. 77
4.21 Illustration of the truncation of the beam induced by the base plate and the sample holder. 77
4.22 Measurements of the beam shape in the cryostat. 78
4.23 Beam waist propagation as a function of frequency. 78
4.24 Measured spectrum of the at 220 GHz. 79
4.25 Output power as a function of frequency of our sources. 80
4.26 Illustration of the active area of the samples. 81
4.27 Full description of the bench. 83
4.28 Simplified algorithm of operation of the *Tera-Spectro* and *Tera-Spectro^{mini}* programs. 84
4.29 Some results generated by the *Tera-Spectro^{mini} with $I_d - V_d$ addon!*. 85
4.30 Simplified algorithm of operation of the *Tera-Spectro^{mini} with $I_d - V_d$ addon!*. 86
4.31 220 – 325 GHz transmission calibration $P_c(\nu)$. 87

4.32 Illustration of the pulsed measurement setup. 88
4.33 Example of pulses measured by the oscilloscope. 88

5.1 DC and pulsed I-V measurements of a TLM structure for three different temperatures. . . 95
5.2 DC and pulsed I-V measurements of a HEMT structure for three different temperatures. . 96
5.3 DC and pulsed I-V measurements of a IDF structure for three different temperatures. . . 96
5.4 DC and pulsed I-V measurements of TLM structures for three different lengths. 97
5.5 DC and pulsed I-V measurements of HEMT structures for three different lengths. 98
5.6 DC and pulsed I-V measurements of IDF structures for three different lengths. 99
5.7 IDF global resistance dependence on asymmetry. 99
5.8 New interdigitated fingers pattern proposal. 101
5.9 Pulse width effect on HEMT I-V measurement. 101
5.10 Monte-Carlo simulation of a n^+nn^+ bulk GaN diode I-V. 102
5.11 Current-voltage characteristic and its derivative for a 5 µm long TLM. 103
5.12 Current-voltage characteristic and its derivative for a 5 µm long TLM. 103
5.13 Current-voltage characteristic and its derivative for a 10 µm long TLM. 103
5.14 Current-voltage characteristic and its derivative for a 20 µm long TLM. 104

6.1 Experimental scheme of room temperature photomixing measurement. 106
6.2 Transmission spectrum of a GaN over sapphire sample. 107
6.3 Transmission spectrum of a PTFE sample. 108
6.4 Absorption coefficient of PTFE as found in the literature. 109
6.5 Transmission spectrum of a GaAs sample. 110
6.6 Transmission spectrum of a stack of PE sheets. 110
6.7 Illustration of the smoothing effect. 111
6.8 Definition of the direct and crossed polarizations. 112
6.9 Polarization of the source effect on the transmission coefficient. 112
6.10 Temperature effect on the transmission coefficient. 113
6.11 Sample geometry effect on the transmission coefficient. 114
6.12 Gain calculation for different K values. 115
6.13 Electric field effect on the transmission coefficient. 117
6.14 Electric field effect on the transmission coefficient, different view. 118

A.1 Photography of a Hg-probe. 127
A.2 Typical $C(V)$ measurement with a Hg-probe. 128
A.3 Pattern of a Hall cross used on our samples. 129
A.4 Evolution of the asymmetry function f. 129
A.5 Isolation pattern used to measure R_B. 131
A.6 TLM pattern used to measure R_C and R_S. 131
A.7 Measurement of resistance as a function of L on the TLM structure. 132

B.1 Regulation loop of the power of a laser 134
B.2 Regulation loop of the wavelength of a laser 134

List of Tables

2.1 Physical parameters of wurtzite GaN. 41

3.1 Energy levels occupation in the quantum well for a lattice temperature of 10 K. 54
3.2 Energy levels occupation in the quantum well for a lattice temperature of 300 K. 54
3.3 Dimensions (µm) of interdigitated fingers of the mask of figure 2.25. 55
3.4 Different advantages and drawbacks of some possible substrates for GaN growing. 56
3.5 Dimensions (µm) of interdigitated fingers measured by SEM. 58
3.6 Summary of electrical properties measured at room temperature of the PTC465 sample. . 60

4.1 Summary of bolometer characteristics according to IRLabs data. 72
4.2 RF generator characteristics. 79

Bibliography

[Albrecht 98] J.D. Albrecht, R.P. Wang, P.P. Ruden, M. Farahmand & K.F. Brennan. *Electron transport characteristics of GaN for high temperature device modeling*. Journal Of Applied Physics, vol. 83, no. 9, pages 4777–4781, MAY 1 1998.

[Arabshahi 09] H. Arabshahi & A.A. Mowlavi. *Low-Field Electron Transport Properties in Zincblende and Wurtzite GaN Structures Using an Iteration Model For Solving Boltzmann Equation*. Modern Physics Letters B, vol. 23, no. 10, pages 1359–1366, Apr 20 2009.

[Avrutin 10] Vitaliy Avrutin, Donald J. Silversmith, Yusuke Mori, F. Kawamura, Y. Kitaoka & Hadis Morkoc. *Growth of Bulk GaN and AlN: Progress and Challenges*. Proceedings Of The Ieee, vol. 98, no. 7, pages 1302–1315, Jul 2010.

[Baron 09] N. Baron. *Optimisation de l'épitaxie sous jets moléculaires d'hétérostructures à base de GaN : application aux transistors à haute mobilité d'électrons sur substrat silicium*. PhD thesis, Université de Nice-Sophia Antipolis, Sep 2009.

[Bennett 87] B.R. Bennett & R.A. Soref. *Electrorefraction and electroabsorption in InP, GaAs, GaSb, and InSb*. IEEE Journal of Quantum Electronics, vol. 23, no. 12, pages 2159–2166, DEC 1987.

[Bondar 99] V.N. Bondar, A.T. Dalakyan, L.E. Vorob'ev, D.A. Firsov & V.N. Tulupenko. *Far-IR radiation of hot holes in germanium for mutually perpendicular directions of uniaxial pressure and electric field*. JETP Letters, vol. 70, no. 4, pages 265–269, Aug 25 1999.

[Bougrov 01] V. Bougrov, M.E. Levinshtein, S.L. Rumyantsev & A. Zubrilov. *Properties of Advanced Semiconductor Materials GaN, AlN, InN, BN, SiC, SiGe*. Eds. Levinshtein ME, Rumyantsev SL, Shur MS, John Wiley & Sons, Inc., New York, pages 1–30, 2001.

[Bravina 07] S. L. Bravina, N. V. Morozovsky, A. N. Morozovska, S. Gille, J.-P. Salvestrini & M. D. Fontana. *Investigations of LiNbO3 and LiTaO3 single crystals for pyroelectric applications in the wide temperature range*. Ferroelectrics, vol. 353, pages 636–645, 2007. 8th European Conference on Applications of Polar Dielectrics (ECAPD-8), Metz, FRANCE, SEP 05-08, 2006.

[Brown 95] E.R. Brown, K.A. McIntosh, K.B. Nichols & C.L. Dennis. *Photomixing up to 3.8-THz in low-temperature-grown GaAs*. Applied Physics Letters, vol. 66, no. 3, pages 285–287, JAN 16 1995.

[Brunner 09] Fabian D.J. Brunner, Arno Schneider & Peter Guenter. *A terahertz time-domain spectrometer for simultaneous transmission and reflection measurements at normal incidence*. Optics Express, vol. 17, no. 23, pages 20684–20693, NOV 9 2009.

[Cadoret 99] R. Cadoret. *Growth mechanisms of (00.1)GaN substrates in the hydride vapour-phase method: surface diffusion, spiral growth, H-2 and GaCl3 mechanisms*. Journal of Crystal Growth, vol. 205, no. 1-2, pages 123–135, AUG 1999.

[Cordier 07] Y. Cordier, M. Azize, N. Baron, S. Chenot, O. Tottereau & J. Massies. *AlGaN/GaN HEMTs regrown by MBE on epi-ready semi-insulating GaN-on-sapphire with inhibited interface contamination*. Journal of Crystal Growth, vol. 309, no. 1, pages 1–7, NOV 1 2007.

[Coutaz 08] J.L. Coutaz, R. Boquet, N. Breuil, L. Chusseau, P. Crozat, J. Demaison, L. Duvillaret, G. Gallot, F. Garet, J.F. Lampin, D. Lippens, J. Mangeney, P. Mounaix, G. Mouret & J.F. Roux. Optoélectronique térahertz. Coutaz, J.L., 2008.

[Czarny 07] R. Czarny. *Étude et réalisation d'une source térahertz accordable de grande pureté spectrale*. PhD thesis, Université des Sciences et Technologies de Lille, France, IEMN & Thales R&T, JUN 2007.

[Dabouis 09] V. Dabouis, Y. Chancerelle, D. Crouzier & J.C. Debouzy. *What's new in biomedical applications for Terahertz (THz) technology*. M S-Medecine Sciences, vol. 25, no. 8-9, pages 739–743, AUG-SEP 2009.

[DiDomenico 62] M. DiDomenico, R.H. Pantell, O. Svelto & J.N. Weaver. *Optical frequency mixing in bulk semiconductors*. Applied Physics Letters, vol. 1, no. 4, pages 77–79, 1962.

[Dragoman 04] D. Dragoman & M Dragoman. *Terahertz fields and applications*. Progress in Quantum Electronics, vol. 28, no. 1, pages 1–66, 2004.

[Dyson 59] J. Dyson. *The equiangular spiral antenna*. Antennas and Propagation, IRE Transactions on, vol. 7, no. 2, pages 181 –187, april 1959.

[Ernst 97] A.N. Ernst, M.H. Somerville & J.A. Del Alamo. *Dynamics of the kink effect in InAlAs/InGaAs HEMTs*. Electron Device Letters, IEEE, vol. 18, no. 12, pages 613 –615, dec. 1997.

[Fathallah 10] O. Fathallah, M. Gassoumi, B. Grimbert, C. Gaquiere & H. Maaref. *Parasitic effects and traps in AlGaN/GaN HEMT on sapphire substrate*. European Physical Journal-Applied Physics, vol. 51, no. 1, JUL 2010.

[Ferguson 01] B. Ferguson, S. Mickan, S. Hubbard, D. Pavlidis & D. Abbott. *Investigation of gallium nitride T-ray transmission characteristics*. In Electronics And Structures For MEMS II, volume 4591 of *Proceedings Of The Society Of Photo-Optical Instrumentation Engineers (SPIE)*, pages 210–220, 2001.

[Fixsen 99] D.J. Fixsen, C.L. Bennett & J.C. Mather. *COBE Far Infrared Absolute Spectrophotometer observations of Galactic lines*. Astrophysical Journal, vol. 526, no. 1, Part 1, pages 207–214, NOV 20 1999.

[Frayssinet 00] E. Frayssinet, W. Knap, P. Lorenzini, N. Grandjean, J. Massies, C. Skierbiszewski, T. Suski, I. Grzegory, S. Porowski, G. Simin, X. Hu, M.A. Khan, M.S. Shur, R. Gaska & D. Maude. *High electron mobility in AlGaN/GaN heterostructures grown on bulk GaN substrates*. Applied Physics Letters, vol. 77, no. 16, pages 2551–2553, OCT 16 2000.

[Gaquiere 07] C. Gaquiere, F. Medjdoub, J. F. Carlin, S. Vandenbrouck, E. Delos, E. Feltin, N. Grandjean & E. Kohn. *AlInN/GaN a suitable HEMT device for extremely high*

power high frequency applications. IEEE MTT-S International Microwave Symposium Digest, pages 2136–2139. IEEE MTTS, IEEE, 2007.

[Gaubert 03] C. Gaubert, L. Chusseau & D. Gasquet. *Antennes plaquées fractales millimétriques et sub-millimétriques*. volume 5D12, 2003. 13ème Journées Nationales Microondes, Lille.

[Gavrilenko 91] V.I. Gavrilenko & Z.F. Krasilnik. *Negative mass cyclotron-resonance MASER*. Optical and Quantum Electronics, vol. 23, no. Sp. Iss. SI, pages S323–S339, 1991.

[Gornik 91] E. Gornik & A. A. Andronov. *Far-infrared semiconductor lasers*. Optical and Quantum Electronics, vol. 23, no. 2, page v, January 1991.

[Goto 04] M. Goto, A. Quema, H. Takahashi, S. Ono & N. Sarukura. *Polarization-preserving teflon photonic crystal fiber waveguide for THz radiation*. pages 139–140, 345 E 47TH ST, NEW YORK, NY 10017 USA, 2004. IEEE.

[Greenberg 03] M.C. Greenberg, K.L. Virga & C.L. Hammond. *Performance characteristics of the dual exponentially tapered slot antenna (DETSA) for wireless communications applications*. IEEE Transactions on Vehicular Technology, vol. 52, no. 2, pages 305–312, MAR 2003.

[Gregory 05] I.S. Gregory, W.R. Tribe, C. Baker, B.E. Cole, M.J. Evans, L. Spencer, M. Pepper & M. Missous. *Continuous-wave terahertz system with a 60 dB dynamic range*. Applied Physics Letters, vol. 86, no. 20, MAY 16 2005.

[Grischkowsky 90] D. Grischkowsky, S. Keiding, M. Vanexter & C. Fattinger. *Far-infrared time-domain spectroscopy with terahertz beams of dielectrics and semiconductors*. Journal of The Optical Society of America B-Optical Physics, vol. 7, no. 10, pages 2006–2015, OCT 1990.

[Guillet 10] J.P. Guillet. *Microscopie en champ proche terahertz en régime continu*. PhD thesis, Université Montpellier 2, France, December 2010.

[Hafez 05] W. Hafez, W. Snodgrass & M Feng. *12.5 nm base pseudomorphic heterojunction bipolar transistors achieving f(T)=710 GHz and f(MAX)=340 GHz*. Applied Physics Letters, vol. 87, no. 25, DEC 19 2005.

[Hamaguchi 01] Chihiro Hamaguchi. Basic semiconductor physics. Springer-Verlag, Berlin, 2001. ISBN 3-540-41639-0.

[Hu 09] Weiguo Hu, Bei Ma, Dabing Li, Mitsuhisa Narukawa, Hideto Miyake & Kazumasa Hiramatsu. *Mobility enhancement of 2DEG in MOVPE-grown AlGaN/AlN/GaN HEMT structure using vicinal (0001) sapphire*. Superlattices And Microstructures, vol. 46, no. 6, pages 812–816, DEC 2009.

[Hubers 05] H.W. Hubers, S.G. Pavlov & V.N. Shastin. *Terahertz lasers based on germanium and silicon*. Semiconductor Science and Technology, vol. 20, no. 7, pages S211–S221, JUL 2005.

[Iniguez-de-la Torre 10] A. Iniguez-de-la Torre, J. Mateos & T. Gonzalez. *Terahertz current oscillations assisted by optical phonon emission in GaN n(+)nn(+) diodes: Monte Carlo simulations*. Journal Of Applied Physics, vol. 107, no. 5, MAR 1 2010.

[Ito 05] H. Ito, F. Nakajima, T. Furuta & T Ishibashi. *Continuous THz-wave generation using antenna-integrated uni-travelling-carrier photodiodes*. Semiconductor Science and Technology, vol. 20, no. 7, pages S191–S198, JUL 2005.

[Jin 06] Yun-Sik Jin, Geun-Ju Kim & Seok-Gy Jeon. *Terahertz dielectric properties of polymers*. Journal of the Korean Physical Society, vol. 49, no. 2, pages 513–517, AUG 2006.

[Joblot 05] S. Joblot, F. Semond, Y. Cordier, P. Lorenzini & J. Massies. *High-electron-mobility AlGaN/GaN heterostructures grown on Si(001) by molecular-beam epitaxy*. Applied Physics Letters, vol. 87, no. 13, SEP 26 2005.

[Johansson 92] J.F. Johansson & N.D. Whyborn. *The Diagonal Horn as a Sub-Millimeter Wave Antenna*. IEEE Transactions on Microwave Theory and Techniques, vol. 40, no. 5, pages 795–800, MAY 1992.

[Kemp 03] M.C. Kemp, P.F. Taday, B.E. Cole, J.A. Cluff, A.J. Fitzgerald & W.R. Tribe. *Security applications of terahertz technology*. Terahertz for Military and Security Applications, vol. 5070, no. 1, pages 44–52, 2003.

[Khalid 07] A. Khalid, N. J. Pilgrim, G. A. Dunn, A. C. Holland, C. R. Stanley, I. G. Thayne & D. R. S. Cumming. *A planar Gunn diode operating above 100 GHz*. IEEE Electron Device Letters, vol. 28, no. 10, pages 849–851, OCT 2007.

[Kohler 02] R. Kohler, A. Tredicucci, F. Beltram, HE Beere, EH Linfield, AG Davies, DA Ritchie, RC Iotti & F Rossi. *Terahertz semiconductor-heterostructure laser*. Nature, vol. 417, no. 6885, pages 156–159, MAY 9 2002.

[Kominami 85] M. Kominami, D.M. Pozar & D.H. Schaubert. *Dipole and slot elements and arrays on semi-infinite substrates*. IEEE Transactions on Antennas and Propagation, vol. 33, no. 6, pages 600–607, 1985.

[Krithivasan 06] Ramkumar Krithivasan, Yuan Lu, John D. Cressler, Jae-Sung Rieh, Marwan H. Khater, David Ahlgren & Greg Freeman. *Half-terahertz operation of SiGeHBTs*. IEEE Electron Device Letters, vol. 27, no. 7, pages 567–569, JUL 2006.

[Kromer 58] H. Kromer. *Proposed negative-mass microwave amplifier*. Physical Review, vol. 109, no. 5, page 1856, 1958.

[Kucharski 09] R. Kucharski, M. Rudzinski, M. Zajac, R. Doradzinski, J. Garczynski, L. Sierzputowski, R. Kudrawiec, J. Serafinczuk, W. Strupinski & R. Dwilinski. *Nonpolar GaN substrates grown by ammonothermal method*. Applied Physics Letters, vol. 95, no. 13, SEP 28 2009.

[Kumar 03] V. Kumar, A. Kuliev, R. Schwindt, M. Muir, G. Simin, J. Yang, MA Khan & I. Adesida. *High performance 0.25 mu m gate-length AlGaN/GaN HEMTs on sapphire with power density of over 4.5 W/mm at 20 GHz*. Solid-State Electronics, vol. 47, no. 9, pages 1577–1580, SEP 2003.

[Kuzmik 02] J. Kuzmik. *InAlN/(In)GaN high electron mobility transistors: some aspects of the quantum well heterostructure proposal*. Semiconductor Science And Technology, vol. 17, no. 6, pages 540–544, JUN 2002.

[Lee 08] Mark Lee, Michael C. Wanke, Maytee Lerttamrab, Erik W. Young, Albert D. Grine, John L. Reno, Peter H. Siegel & Robert J. Dengler. *Heterodyne mixing of terahertz quantum cascade lasers using a planar Schottky diode*. IEEE Journal of Selected Topics in Quantum Electronics, vol. 14, no. 2, pages 370–373, MAR-APR 2008.

[Lin 05] C.H. Lin, W.K. Wang, P.C. Lin, C.K. Lin, Y.J. Chang & Y.J. Chan. *Transient pulsed analysis on GaNHEMTs at cryogenic temperatures*. IEEE Electron Device Letters, vol. 26, no. 10, pages 710–712, OCT 2005.

[Liu 02] L. Liu & J.H. Edgar. *Substrates for gallium nitride epitaxy*. Materials Science & Engineering R-Reports, vol. 37, no. 3, pages 61–127, APR 30 2002.

[Lucznik 05] B. Lucznik, B. Pastuszka, I. Grzegory, M. Bockowski, G. Kamler, E. Litwin-Staszewska & S Porowski. *Deposition of thick GaN layers by HVPE on the pressure grown GaN substrates*. Journal of Crystal Growth, vol. 281, no. 1, pages 38–46, JUL 15 2005. International Workshop on Bulk Nitride Semiconductors III, Zakopane, Poland, SEP 04-09, 2004.

[Lundstrom 00] M. Lundstrom. Fundamentals of carrier transport. Press syndicate of the University of Cambridge, 2nd edition, 2000.

[Marinchio 10] H. Marinchio, L. Chusseau, J. Torres, P. Nouvel, L. Varani, G. Sabatini, C. Palermo, P. Shiktorov, E. Starikov & V. Gruzinskis. *Room-temperature terahertz mixer based on the simultaneous electronic and optical excitations of plasma waves in a field effect transistor*. Applied Physics Letters, vol. 96, no. 1, JAN 4 2010.

[Martin 01] S. Martin, B. Nakamura, A. Fung, P. Smith, J. Bruston, A. Maestrini, F. Maiwald, P. Siegel, E. Schlecht & I Mehdi. *Fabrication of 200 to 2700 GHz multiplier devices using GaAs and metal membranes*. In B Sigmon, editeur, 2001 IEEE MTT-S International Microwave Symposium Digest, VOLS 1-3, pages 1641–1644. IEEE; MTTS, IEEE, 2001.

[Maruska 69] H.P. Maruska & J.J. Tietjen. *Preparation and Properties of Vapor-Deposited Single-Crystalline GaN*. Applied Physics Letters, vol. 15, no. 10, pages 327–&, 1969.

[Matsuura 97] S. Matsuura, M. Tani & K. Sakai. *Generation of coherent terahertz radiation by photomixing in dipole photoconductive antennas*. Applied Physics Letters, vol. 70, no. 5, pages 559–561, FEB 3 1997.

[McCarthy 52] K.A. McCarthy, S.S. Ballard & E.C. Doerner. *Thermal Conductivity of Sapphire and Rutile as a Function of Temperature*. Physical Review, vol. 88, no. 1, page 153, 1952.

[Mendis 04] R. Mendis, C. Sydlo, J. Sigmund, M. Feiginov, P. Meissner & H.L. Hartnagel. *Tunable CW-THz system with a log-periodic photoconductive emitter*. Solid-State Electronics, vol. 48, no. 10-11, pages 2041–2045, OCT-NOV 2004. International Semiconductor Device Reseaech Symposium (ISDRS 03), Washington, DC, DEC 10-12, 2003.

[Miles 00] R.E. Miles, P. Harrison & D. Lippens. Terahertz sources and systems, volume 27 of *II*. NATO Science, 22-27 June 2000. Proceedings of the NATO Advanced Research Workshop, Château de Bonas, France.

[Morimoto 73] Y. Morimoto, K. Uchiho & S. Ushio. *Vapor-Phase Epitaxial-Growth of GaN on GaAs, GaP, Si, and Sapphire Substrates from GaBr3 and NH3*. Journal Of The Electrochemical Society, vol. 120, no. 12, pages 1783–1785, 1973.

[Mouret 06] G. Mouret, S. Matton, R. Bocquet, D. Bigourd, F. Hindle, A. Cuisset, J.-F. Lampin & D. Lippens. *Anomalous dispersion measurement in terahertz frequency region by photomixing*. Applied Physics Letters, vol. 88, no. 18, MAY 1 2006.

[Nag 80] B.R. Nag. Electron transport in compound semiconductors / b.r. nag. Springer-Verlag, Berlin ; New York, 1980.

[Natali 09] F. Natali, Y. Cordier, C. Chaix & P. Bouchaib. *Advances in quality and uniformity of (Al,Ga)N/GaN quantum wells grown by molecular beam epitaxy with plasma source*. Journal Of Crystal Growth, vol. 311, no. 7, pages 2029–2032, Mar 15 2009.

[Odnoblyudov 00] M.A. Odnoblyudov, I.N. Yassievich, M.S. Kagan & K.A. Chao. *Mechanism of population inversion in uniaxially strained p-Ge continuous-wave lasers*. Phys. Rev. B, vol. 62, no. 23, pages 15291–15294, Dec 2000.

[Palermo 04] C. Palermo. *Évaluation des effets d'une onde hyperfréquence de forte puissance sur les matériaux à application optroniques : Application au $Hg_{1-x}Cd_xTe$*. PhD thesis, Université Montpellier 2, France, October 2004.

[Parker 01] A.E. Parker & J.G. Rathmell. *Measurement and characterization of HEMT dynamics*. IEEE Transactions On Microwave Theory And Techniques, vol. 49, no. 11, pages 2105–2111, NOV 2001. 12th Asia/Pacific Microwave Conference (APMC), Sydney, Australia, DEC 03-06, 2000.

[Polian 96] A. Polian, M. Grimsditch & I Grzegory. *Elastic constants of gallium nitride*. Journal Of Applied Physics, vol. 79, no. 6, pages 3343–3344, MAR 15 1996.

[Pozhela 92] Y.K. Pozhela, E.V. Starikov & P.N. Shiktorov. *Dynamic NDM at Transit-Time Resonance in n-InP*. Semiconductor Science And Technology, vol. 7, no. 3B, pages B386–B389, Mar 1992. 7TH International Conf On Hot Carriers In Semiconductors (HCIS-7), Nara, Japan, Jul 01-05, 1991.

[Reggiani 85] L. Reggiani, editeur. Hot-electron transport in semiconductors, volume 58 of *Topics in Applied Physics*. Springer-Verlag, 1985.

[Richter 08] H. Richter, A.D. Semenov, S.G. Pavlov, L. Mahler, A. Tredicucci, H.E. Beere, D.A. Ritchie, K.S. Il'in, M. Siegel & H.-W. Huebers. *Terahertz heterodyne receiver with quantum cascade laser and hot electron bolometer mixer in a pulse tube cooler*. Applied Physics Letters, vol. 93, no. 14, OCT 6 2008.

[RIKEN 10] RIKEN. THz database Web: `http://www.riken.jp/THzdatabase/`, Teraphotonics Laboratory, Sendai, 2010.

[Savelli 96] M. Savelli, D. Gasquet & B. Orsal. *Physique des dispositifs électroniques*. Techniques de l'Ingénieur, vol. E1100, pages 1–57, June 1996.

[Scalari 06] G. Scalari, C. Walther, J. Faist, H. Beere & D Ritchie. *Electrically switchable, two-color quantum cascade laser emitting at 1.39 and 2.3 THz*. Applied Physics Letters, vol. 88, no. 14, APR 3 2006.

[Shannon 49] C.E. Shannon. *Communication In The Presence Of Noise*. Proceedings Of The Institute Of Radio Engineers, vol. 37, no. 1, pages 10–21, 1949.

[Shen 09] F. Shen & Y.B. Ying. *Applications of Terahertz Spectroscopy and Imaging Techniques in Food Safety Inspection*. Spectroscopy and Spectral Analysis, vol. 29, no. 6, pages 1445–1449, JUN 2009.

[Shiktorov 07] P. Shiktorov, E. Starikov, V. Gruzinskis, L. Varani, C. Palermo, J.-F. Millithaler & L. Reggiani. *Frequency limits of terahertz radiation generated by optical-phonon transit-time resonance in quantum wells and heterolayers*. Physical Review B, vol. 76, no. 4, Jul 2007.

[Shur 96] M. Shur, B. Gelmont & M.A. Khan. *Electron mobility in two-dimensional electron gas in AlGaN/GaN heterostructures and in bulk GaN*. Journal of Electronic Materials, vol. 25, no. 5, pages 777–785, May 1996. Electronic Materials Conference, Charlottesville, VA, JUN 21-23, 1995.

[Siegel 02] P.H. Siegel. *Terahertz technology*. IEEE Transactions on Microwave Theory and Techniques, vol. 50, no. 3, pages 910–928, mar 2002.

[Siegel 04] P.H. Siegel. *Terahertz technology in biology and medicine*. IEEE Transactions on Microwave Theory and Techniques, vol. 52, no. 10, pages 2438–2447, 2004.

[Starikov 01] E. Starikov, P. Shiktorov, V. Gružinskis, L. Reggiani, L. Varani, J.C. Vaissière & Jian H. Zhao. *Monte Carlo simulation of the generation of terahertz radiation in GaN*. Journal of Applied Physics, vol. 89, no. 2, pages 1161–1171, 2001.

[Starikov 08] E. Starikov, P. Shiktorov, V. Gružinskis, L. Varani, C. Palermo, J-F. Millithaler & L. Reggiani. *Terahertz generation in nitrides due to transit-time resonance assisted by optical phonon emission*. Journal of Physics: Condensed Matter, vol. 20, no. 38, page 384209 (12pp), 2008.

[Suemitsu 98] T. Suemitsu, T. Enoki, N. Sano, M. Tomizawa & Y. Ishii. *An analysis of the kink phenomena in InAlAs/InGaAs HEMT's using two-dimensional device simulation*. IEEE Transactions On Electron Devices, vol. 45, no. 12, pages 2390–2399, DEC 1998.

[Tani 02] M. Tani, M. Herrmann & K. Sakai. *Generation and detection of terahertz pulsed radiation with photoconductive antennas and its application to imaging*. Measurement Science & Technology, vol. 13, no. 11, pages 1739–1745, NOV 2002.

[TeraView 10] TeraView. `http://www.teraview.com/`, Cambridge, UK, 2010.

[Tredicucci 04] A. Tredicucci, R. Kohler, F. Beltram, HE Beere, EH Linfield, AG Davies & DA Ritchie. *Terahertz quantum cascade lasers*. Physica E-Low-Dimensional Systems & Nanostructures, vol. 21, no. 2-4, pages 846–851, MAR 2004. 11th International Conference on Modulated Semiconductor Structures (MSS11), Nara, JAPAN, JUL 14-18, 2003.

[Tydex 10] Tydex. THz optical components: `http://www.tydex.ru/`, 2010.

[van der Paw 58] L.J. van der Paw. *A Method of Measuring Specific Resistivity and Hall Effect of Discs of Arbitrary Shape*. Philips Research Reports, vol. 13, no. 1, pages 1–9, FEB 1958.

[Van Exter 89] M. Van Exter, C. Fattinger & D. Grischkowsky. *Terahertz time-domain spectroscopy of water-vapor*. Optics Letters, vol. 14, no. 20, pages 1128–1130, OCT 15 1989.

[Vorob'ev 01] L. Vorob'ev, S. Danilov, V. Tulupenko & D. Firsov. *Generation of millimeter radiation due to electric-field-induced electron-transit-time resonance in indium phosphide*. JETP Letters, vol. 73, no. 5, pages 219–222, March 2001.

[Wagner-Gentner 06] A. Wagner-Gentner, U.U. Graf, D. Rabanus & K. Jacobs. *Low loss THz window*. Infrared Physics & Technology, vol. 48, no. 3, pages 249–253, AUG 2006.

[Ward 08] John S. Ward, Goutam Chattopadhyay, John Gill, Hamid Javadi, Choonsup Lee, Robert Lin, Alain Maestrinia, Frank Maiwald, Imran Mehdi, Erich Schlecht & Peter Siegel. *Tunable Broadband Frequency-Multiplied Terahertz Sources*. In 33RD International Conference on Infrared, Millimeter and Terahertz Waves, VOLS 1 AND 2, pages 52–54. IEEE, IEEE, 2008.

[Werner 03] D.H. Werner & S. Ganguly. *An overview of fractal antenna engineering research*. IEEE Antennas and Propagation Magazine, vol. 45, no. 1, pages 38–57, FEB 2003.

[Winnewisser 98] C. Winnewisser, F. Lewen & H. Helm. *Transmission characteristics of dichroic filters measured by THz time-domain spectroscopy*. Applied Physics A-Materials Science & Processing, vol. 66, no. 6, pages 593–598, JUN 1998.

[Yamane 97] H. Yamane, M. Shimada, S.J. Clarke & F.J. DiSalvo. *Preparation of GaN single crystals using a Na flux*. Chemistry of Materials, vol. 9, no. 2, pages 413–&, FEB 1997.

[Ziegler 93] J.G. Ziegler & N.B. Nichols. *Optimum Settings for Automatic Controllers*. Journal of Dynamic Systems Measurement and Control-Transactions of the ASME, vol. 115, no. 2B, pages 220–222, JUN 1993.

Publications of the author

Articles in international journals

[J1] E. Starikov, P. Shiktorov, V. Gruzhinskis, L. Varani, C. Palermo, G. Sabatini, H. Marinchio, **T. Laurent**, and L. Reggiani. Anomalous behavior of electronic noise related to the onset of current instabilities in n+nn+ diodes. *Journal of Statistical Mechanics : Theory and Experiment*, 2009(01):P01035, 2009.

[J2] **T. Laurent**, P. Nouvel, J. Torres, L. Chusseau, C. Palermo, L. Varani, Y. Cordier, J-P. Faurie, B. Beaumont, E. Starikov, P. Shiktorov, and V. Gruzhinskis. Preliminary results of bench implementation for the study of terahertz amplification in gallium nitride quantum wells. *Journal of Physics : Conference Series*, 193:012094 (4pp), 2009.

[J3] R. Sharma, **T. Laurent**, J. Torres, P. Nouvel, S. Blin, C. Palermo, L. Varani, Y. Cordier, M. Chmielowska, S. Chenot, J-P. Faurie, B. Beaumont, P. Shiktorov, E. Starikov, and V. Gruzhinskis. THz gain measurement of GaN quantum wells at low temperatures. *Applied Physics Letters*, TO BE SUBMITTED, 2010.

[J4] **T. Laurent**, R. Sharma, J. Torres, P. Nouvel, S. Blin, C. Palermo, L. Varani, Y. Cordier, M. Chmielowska, S. Chenot, J-P. Faurie, B. Beaumont, P. Shiktorov, E. Starikov, and V. Gruzhinskis. Voltage controlled terahertz transmission enhancement through GaN quantum wells. *Applied Physics Letters*, TO BE SUBMITTED, 2010.

[J5] **T. Laurent**, R. Sharma, J. Torres, P. Nouvel, S. Blin, C. Palermo, L. Varani, Y. Cordier, M. Chmielowska, J-P. Faurie, and B. Beaumont. Pulsed Current-Voltage Characteristics of AlGaN/GaN HEMTs from room to low temperature. Solid State Electronics, SUBMITTED, 2010.

[J6] P. Ziadé, H. Marinchio, **T. Laurent**, G. Sabatini, Z. Kallassy, C. Palermo, and L. Varani. Hydrodynamic study of terahertz three-dimensional plasma resonances in InGaAs diodes. *Semiconductor Science and Technology*, 25(7):075012, 2010.

Articles in international conferences

[IC1] L. Chusseau, L. Varani, J. Torres, C. Palermo, P. Nouvel, A. Penarier, H. Marinchio, G. Sabatini, **T. Laurent**, P. Shiktorov, E. Starikov, and V. Gruzhinskis. THz detection and generation by semiconductor heterostructures using transport properties in InGaAs HEMT and GaN 2D electron gas. pages 155–156, Venezia, Italy, nov 2008. *HETECH*.

[IC2] H. Marinchio, G. Sabatini, **T. Laurent**, J. Pousset, C. Palermo, J. Torres, L. Varani, L. Chusseau, Y. Roelens, and S. Bollaert. Experimental and theoretical investigation of optically excited THz plasma waves in submicron InGaAs HEMTs. *EOS Annual Meeting*, sep 2008.

[IC3] H. Marinchio, G. Sabatini, J. Torres, **T. Laurent**, J. Pousset, C. Palermo, L. Varani, L. Chusseau, P. Shiktorov, E. Starikov, and V. Gruzhinskis. Analytical and numerical modelling of optical excitation of THz plasma modes in nanoHEMTs. pages 157–158, Venezia, Italy, nov 2008. *HETECH*.

[IC4] G. Sabatini, H. Marinchio, J. Pousset, **T. Laurent**, C. Palermo, L. Varani, J.-F. Millithaler, L. Reggiani, T. Rodilla, T. González, S. Perez, and J. Mateos. Study of electronic transport in high mobility materials : application to InGaAs and InAs. pages 61–62, Venezia, Italy, nov 2008. *HETECH*.

[IC5] **T. Laurent**, G. Sabatini, P. Nouvel, J. Torres, C. Palermo, L. Chusseau, L. Varani, Y. Cordier, E. Starikov, P. Shiktorov, and V. Gruzhinskis. Terahertz generation in GaN quantum wells by amplification of transverse electromagnetic waves. pages 85–86, Venezia, Italy, nov 2008. *HETECH*.

[IC6] J-P. Guillet, L. Chusseau, R. Adam, **T. Laurent**, T. Grosjean, A. Penarier, and D. Charraut. Terahertz near-field imaging using a Y splitter and Sommerfeld wire waves on bare metal rods. Roma, Italy, sep 2010. *35th International Conference on Infrared, Millimeter and THz Waves (IRMMW-THz 2010)*.

[IC7] H. Marinchio, C. Palermo, G. Sabatini, P. Ziadé, P. Shiktorov, E. Starikov, V. Gruzhinskis, **T. Laurent**, P. Nouvel, J. Torres, A. Penarier, S. Blin, L. Chusseau, and L. Varani. Hydrodynamic simulation of heterodyne terahertz detection in a field effect transistor. Roma, Italy, sep 2010. *35th International Conference on Infrared, Millimeter and THz Waves (IRMMW-THz 2010)*.

[IC8] H. Marinchio, C. Palermo, G. Sabatini, P. Ziadé, **T. Laurent**, P. Shiktorov, E. Starikov, V. Gruzhinskis, P. Nouvel, J. Torres, A. Penarier, S. Blin, L. Chusseau, and L. Varani. Hydrodynamic study of electronic, optical and thermal excitation of plasma waves in HEMTs. Roma, Italy, sep 2010. *35th International Conference on Infrared, Millimeter and THz Waves (IRMMW-THz 2010)*.

[IC9] P. Nouvel, J. Torres, H. Marinchio, **T. Laurent**, S. Blin, L. Chusseau, C. Palermo, L. Varani, P. Shiktorov, E. Starikov, V. Gruzhinskis, F. Teppe, and D. Coquillat. Measurements of THz emission from nanometric-size transistors. Roma, Italy, sep 2010. *35th International Conference on Infrared, Millimeter and THz Waves (IRMMW-THz 2010)*.

[IC10] **T. Laurent**, S. Ginestar, S. Blin, L. Chusseau, J. Torres, P. Nouvel, C. Palermo, and L. Varani. Frequency Stabilization of Photo-Mixing Generated Signal Using a Single Michelson Interferometer. Roma, Italy, sep 2010. *35th International Conference on Infrared, Millimeter and THz Waves (IRMMW-THz 2010)*.

[IC11] **T. Laurent**, R. Sharma, P. Nouvel, S. Blin, L. Chusseau, C. Palermo, L. Varani, Y. Cordier, M. Chmielowska, J-P. Faurie, and B. Beaumont. Enhanced Terahertz Transmission in AlGaN/GaN two-dimensional electron gas. Marriott Tampa Waterside Hotel and Marina in Tampa, Florida, U.S.A., sep 2010. *International Workshop on Nitride semiconductors*.

[IC12] **T. Laurent**, R. Sharma, J. Torres, P. Nouvel, S. Blin, L. Chusseau, C. Palermo, L. Varani, Y. Cordier, M. Chmielowska, J-P. Faurie, and B. Beaumont. Invited presentation - Experimental investigation of THz Transmission in GaN two-dimensional electron gas. Vilnius, Lithuania, aug 2010. *14th International Symposium on Ultrafast Phenomena in Semiconductors (UFPS)*.

[IC13] **T. Laurent**, R. Sharma, J. Torres, P. Nouvel, S. Blin, L. Chusseau, C. Palermo, L. Varani, Y. Cordier, M. Chmielowska, J-P. Faurie, B. Beaumont, E. Starikov, P. Shiktorov, and V. Gruzhinskis. Enhanced Terahertz Transmission of GaN Quantum Wells. Roma, Italy, sep 2010. *35th International Conference on Infrared, Millimeter and THz Waves (IRMMW-THz 2010)*.

[IC14] **T. Laurent**, R. Sharma, J. Torres, P. Nouvel, S. Blin, C. Palermo, L. Varani, Y. Cordier, M. Chmielowska, J-P. Faurie, and B. Beaumont. Measurement of pulsed current-voltage characteristics of AlGaN/GaN HEMTs from room temperature to 15 K. Vilnius, Lithuania, aug 2010. *14th International Symposium on Ultrafast Phenomena in Semiconductors (UFPS)*.

[IC15] P. Ziadé, C. Palermo, L. Varani, Z. Kallassy, H. Marinchio, **T. Laurent**, G. Sabatini, and P. Nouvel. Terahertz Three-Dimensional Plasma Resonances in InGaAs Diodes : An Hydrodynamic Study. Paris - La Défense, France, sep 2010. *40th European Microwave Conference (EuMIC 2010)*.

Seminars

[S1] **T. Laurent**. GaN quantum wells for terahertz amplification. Cork, Ireland, apr 2010. *Visit in Tyndall National Institute*.

Articles in national conferences

[NC1] A. Penarier, P. Nouvel, J.-P. Guillet, **T. Laurent**, J. Torres, R. Adam, S. Jarrix, and L. Chusseau. Probe design for electromagnetic near field THz mappings. Valence, France, sep 2007. *19ème Conf. Optique Hertzienne et Diélectriques*.

[NC2] **T. Laurent**, H. Marinchio, G. Sabatini, J. Torres, L. Chusseau, C. Palermo, and L. Varani. Utilisation des phonons optiques pour la génération d'ondes terahertz dans le GaN (Use of optical phonons in GaN for terahertz waves generation). Bordeaux, France, may 2008. *JNRDM*.

[NC3] **T. Laurent** and L. Varani. Exploitation des phonons optiques polaires dans le GaN en vue de la réalisation d'une source terahertz (Use of polar optical phonons in GaN for the design of a terahertz source). Montpellier, France, jun 2008. *DOCTISS*.

[NC4] **T. Laurent**, L. Chusseau, J. Torres, P. Nouvel, C. Palermo, and L. Varani. Spectroscopie continue d'éléments optiques pour une expérience cryogénique terahertz (Continuous-wave spectroscopy of optical components for a terahertz cryogenic experiment). Lille, France, jun 2009. *THz days*.

[NC5] **T. Laurent**, R. Sharma, S. Blin, and J. Torres. Réalisation d'un banc de spectroscopie terahertz à basses températures (Low-temperatures terahertz spectroscopic set-up realization). Montpellier, France, jun 2010. *JNRDM*.

Étude théorique et expérimentale d'un nouveau MASER terahertz à l'état solide en GaN

L'objet de cette thèse vise à montrer expérimentalement l'amplification dans le domaine terahertz d'échantillons à base de puits quantiques en nitrure de gallium (GaN), maintenus à basses températures (< 100 K), grâce au mécanisme physique de "résonance du temps de transit des phonons optiques". Pour ce faire, un banc expérimental permettant de mesurer le spectre en transmission des échantillons dans différentes gammes de fréquences (0.220–0.325, 0.843–1.100 et 0.75–1.9 THz suivant la source utilisée), et sous différentes conditions (température, orientation, champ électrique appliqué) a été développé. Un deuxième banc, servant à mesurer les caractéristiques courant-tension en régime continu ou pulsé a également été réalisé en vue de l'étude électrique des composants à basses températures. Les résultats montrent l'existence d'un effet conséquent sur le spectre de transmission au fur et à mesure que le champ électrique appliqué augmente.

Les expériences restantes devraient démontrer la viabilité d'une structure MASER constituée des échantillons étudiés dans cette thèse, placés dans une cavité résonante.

Mots clef : terahertz, amplification, GaN, OPTTR, expérimental, puits-quantique.

Theoretical and experimental investigation of a new GaN based solid state terahertz MASER

The objective of this thesis is to experimentally demonstrate the amplification in the terahertz frequency domain by quantum wells of gallium nitride (GaN), maintained at low temperatures (< 100 K), thanks to the so called "optical phonon transit time resonance" mechanism. To achieve that goal, an experimental setup have been developed to measure the transmission spectra of the samples under study in different frequency bands (0.220–0.325, 0.843–1.100 et 0.75–1.9 THz depending on the source), and under different experimental conditions (temperature, orientation, applied electric field). Besides this first setup, another bench have been developed to measure the DC and pulsed current-voltage characteristics at low temperatures. The results show a significant enhancement on the transmission spectra as the applied electric field is increased.

The remaining experiments should demonstrate the feasibility of a MASER structure made of the samples studied in this thesis, surrounded by a resonant cavity.

Keywords: terahertz, amplification, GaN, OPTTR, experimental investigation, quantum-well.

Discipline : électronique, nanotechnologies, composants et systèmes.

Institut d'Électronique du Sud, place Eugène Bataillon – CC 084
34095 MONTPELLIER Cedex 5